# Charged interfaces and their applications in energy sustainability

by

**Sreedath Panat**

Dual Degree: B.Tech in Mechanical Engineering and
M.Tech in Intelligent Manufacturing
Indian Institute of Technology Madras (2017)

Submitted to the Department of Mechanical Engineering
in Partial Fulfillment of the Requirements for the Degree of

**DOCTOR OF PHILOSOPHY**

at the

**MASSACHUSETTS INSTITUTE OF TECHNOLOGY**

February 2023



Signature of Author: ……
Department of Mechanical Engineering
November 21, 2022

Certified by: ……
Kripa K. Varanasi
Professor of Mechanical Engineering
Thesis Supervisor

Accepted by: ……
Nicolas G. Hadjiconstantinou
Professor of Mechanical Engineering
Graduate officer

THIS PAGE INTENTIONALLY LEFT BLANK

# Charged interfaces and their applications in energy sustainability

by

Sreedath Panat

Submitted to the Department of Mechanical Engineering
on November 21, 2022, in Partial Fulfillment of the
Requirements for the Degree of

Doctor of Philosophy in Mechanical Engineering

## Abstract

Energy sustainability is one of the most important challenges of the present time. In this thesis we investigate some critical sustainability challenges and develop advanced mitigation approaches for various energy systems. In photovoltaic systems, dust accumulation on solar panels is a global challenge that affects the operational efficiency. Current water-based methods impose a huge water footprint and cost to solar energy. In crude oil extraction, there is significant waste byproduct formed in the form of water-in-oil nanoscale emulsion due to the mixing of underground water and crude oil. To separate water and oil phases toxic chemical demulsifiers are added which along with effluents from the refineries reach waterbodies, harming the local ecosystem. In post-combustion $CO_2$ capture systems, the absorption of $CO_2$ from flue gas into a sorbent liquid is capital expensive. The need for large surface area of interaction necessitates the installation of prohibitively expensive absorption towers and the usage of environmentally unfriendly chemicals such as amines. In this thesis, we investigate advanced methods by leveraging interfacial charge to make these renewable and non-renewable energy systems more sustainable and efficient. First, we demonstrate a novel approach based on active electrostatic charge induction for charging and electrostatically repelling dust from solar panels. We show that more than 99% of the lost power output can be recovered by our approach without consuming a single drop of water. Second, we develop a non-Laplacian space charge emitter electrocoalescer setup that allows us to apply nearly 8 times stronger electric field compared to traditional electrocoalescers across water-in-oil emulsion to polarize and coalesce the droplets. Thus, we demonstrate that we can successfully phase separate water-in-oil nanoscale emulsions at timescales relevant for crude oil processing systems, while completely eliminating the use of toxic demulsifiers. Finally, we introduce mist-scale droplets for significantly enhancing the interfacial area of interaction between flue gas and the sorbent liquid. We introduce electrostatic space charge injection approach to charge and collect the $CO_2$-absorbed mist droplets at nearly 100% efficiency. Overall, our approach leads to more than 95% $CO_2$ absorption at 2.6-fold reduction in carbon capture capital cost.

Thesis Supervisor: Kripa K. Varanasi
Title: Professor, Department of Mechanical Engineering

THIS PAGE INTENTIONALLY LEFT BLANK

# Acknowledgements

First and foremost, I am deeply grateful to my advisor Prof. Kripa Varanasi for providing the kind of guidance and mentorship he did over the course of the five years of my PhD. Kripa has significantly influenced my way of thinking and the style of research. His acumen for identifying most pressing challenges, conducting most relevant scientific investigations, and effectively communicating the research have to the greatest extend shaped the work I present in this thesis. Our numerous meetings to discuss various ideas have been some of the most valuable times I spent at MIT. Beyond science, I have also learned tremendously from Kripa from his style of leadership that allows for great amount of freedom that fosters endless creativity in the lab culture. Finally, his passion for entrepreneurship has been truly inspiring for me. It has significantly changed my worldview and has influenced my decisions for future. Thank you, Kripa, for making my PhD experience such a wonderful journey.

I also thank Prof. Alan Grodzinsky and Prof. Paulo Lozano for serving on my doctoral committee, and for their valuable insights and feedback.

My grad school experience could not have been as much fun and fulfilling without the super-kind and smart peer group I had the fortune of working with at Varanasi research group. I am incredibly privileged to have some of the best minds in the world as my lifelong friends. I would like to thank Vishnu Jayaprakash with whom I collaborated on several projects, pitch competitions, quals prep and many more, who has always been available for numerous brainstorming. I would also like to thank Maxime Costalonga for truly valuable discussion during our time in the lab. Simon Rufer and Fabian Dickhardt have been instrumental in shaping parts of this thesis. Thank you so much for the awesome collaboration and friendship! Finally, I would like to thank all of the former and current lab members of Varanasi group- Somu, David, Victor, Jack, Caroline, Sami, Baptiste, Alvaro, Sam, Tal, Bert, Divya, Karim, Maher, Leonid, Valentina, Henri, Alex, Sean, Mike, and all other lab mates I had the fortune to spend time with.

On a personal note, I would like to thank my parents, Lalitha and Padmanabhan, and my brother Sreerag, for their unconditional love and support throughout my life. I owe them everything. All of my life decisions are motivated by their implicit and forever support. I specially

want to thank my parents for instilling a culture of hard work with great emphasis on education in our family since my and my brother's young age. My journey would not have happened without that.

I also thank all my friends with whom I have spent so much time. My time in Boston would not have been as much fun without you all- Arun, Raj, Rajat, Roshin, Shourav, Sooraj, Manish, Robin, Aravind, Srishti, Vyshnavi, Krishna, Aroon, Joshua, Sharan and many more.

Finally, I am incredibly thankful to my partner Aiswarya for her tremendous support and for always being there for me, even while being full globe apart. Thank you, Ammu, for being the best partner I could ask for! You are one of the strongest persons I have ever seen and my never-ending source of joy, courage, and motivation!

THIS PAGE INTENTIONALLY LEFT BLANK

# Contents

# List of Figures

# List of Tables

# 1. Introduction

Energy production is one of the sectors whose operation affects every other industry and human beings all around the world. Efficient production of energy is the single biggest factor that determines the quality of life of people. On average, as we live during the time of greatest technological development, the per-capita energy requirement has gone up to levels an order of magnitude bigger than that in the past century[1].

Despite the progress we have made, humanity is on route to an extreme climate crisis, thanks to the unsustainable practices in the energy industry that keeps the modern civilization alive. While coal, oil, and gas still account for more than 60% of electricity generation[2,3], the global push for clean energy has resulted in rapid growth of renewable energy systems. But even with the increase in global renewable energy capacity, the transition to 100% sustainability is a long road and will happen only eventually. Meanwhile it is crucial to ensure efficient and sustainable operation of the existing renewable and non-renewable energy systems.

Interfacial interactions are ubiquitous in all kinds of systems, including energy systems. Since interfaces act as boundaries that define the conditions for transfer of matter, momentum, heat, or charge, controlled interfacial interactions have widespread applications[4]. The genesis of this thesis is from the broader idea that leveraging interfacial charge interactions at micro and nanoscale have novel and highly practical applications in large-scale systems in the energy industry. Specifically, this thesis explores how to make the operation of photovoltaics, oil and gas, and carbon capture systems more efficient and sustainable by introducing interfacial charge and by leveraging the interactions between charged interfaces in these systems. The scientific exploration and technological development attributed to this thesis are largely based on the fundamentals of interfacial science and electrostatics.

## 1.1. Motivation

Photovoltaics is one of the most promising renewable energy systems that is projected to account for ~10% of global electricity generation by 2030[5]. In 2021 solar was the fastest growing source of electricity in the United States. Solar is largely considered as a truly sustainable energy

source. However, there is a big operational challenge that threatens the sustainable nature of solar power. Most of the big solar power plants in the world are located in dry dust-laden desert regions due to the abundance of land area and sunlight[6–11]. However, the wind-borne and airborne dust particles in these regions settle on top of solar panels as shown in Figure 1-1 and reduce the efficiency of photovoltaic systems by up to 30% in one month, if not cleaned regularly[12–14]. In terms of economics, a mere 1% drop in efficiency leads to ~$800,000 loss in annual revenue for a 600 MW power plant. Therefore, solar panels are cleaned often. The most common cleaning technique is by using water. Current water-based solar panel cleaning methods impose a giant water footprint to the photovoltaic systems. Water being a scarce commodity in these arid regions, the water-based cleaning of solar panels is very expensive, costing nearly 10% of annual operation and maintenance cost[6,15]. It is estimated that more than 30 billion gallons of fresh water is being consumed annually, globally for solar panel cleaning purposes[15–17]. This much amount of water can otherwise satisfy the annual water needs of up to 2 million people in developing and underdeveloped regions. Thus, even though we perceive photovoltaics as a renewable energy source, they have huge water footprints associated with them, which is only expected to exponentially grow as the installed solar based grows. The first objective of this thesis is to develop waterless solar panel cleaning approach that makes photovoltaic systems much more efficient and truly sustainable.

Figure 1-1. **Dust accumulation on solar panels.** Blocking of sunlight and the resultant loss of power output due to dust accumulation on solar panels is by far the biggest operational challenge

faced by the modern photovoltaic industry. Image source: Adobe Stock Images licensed asset (#331024517).

Apart from ensuring the sustainability of photovoltaics and other renewable energy systems, it is also crucial to ensure sustainable operation of non-renewable systems to the fullest extent possible. The usage of fossil fuels including crude oil is expected to continue for several decades before fully transitioning to renewable energy sources. One of the biggest areas of unsustainability in crude oil industry apart from carbon emission is in the oil refinement process, especially oil-water separation[18–22]. Crude oil extracted from the underground contains a significant amount of naturally occurring water that is being pumped out along with oil[23,24]. It is estimated that for every barrel of crude oil, nearly three barrels of water is being produced, which is the single largest waste stream generated in the oil and gas industry[25]. Water needs to be removed from the crude oil, where ready to ship crude oil should contain no more than 0.2% water[26]. Up to 20% of water initially present in the oil can be present in emulsified form[27] as shown in Figure 1-2. The emulsified water droplets must be removed before sending the oil for further downstream processing. Often, the emulsified droplets of water present in the oil are sub-micron in size, known as nano-scale emulsion[20]. The small size of the droplets prevent them from settling down, and the droplets are further stabilized due to naturally occurring emulsifying agents in the crude oil such as asphaltenes that act as surfactant, preventing droplet coalescence[28,29]. To promote coalescence, electrocoalescers are used where electrodes are immersed into the emulsion to induce droplet coalescence using applied electric field. Even though electrocoalescers can remove up to 70% of the water droplets that are tens to hundreds of microns in size[30], they are quite ineffective for phase separation of nanoscale droplets. The unseparated oil-water mixture is often collected and diluted with more water to be dumped into the environment. In the US alone, it is estimated that nearly 15 billion barrels of micro-nano droplet contaminated wastewater is generated annually[22].

Demulsifiers are mixed with the water separation process to chemically aid it and increase the electrostatic oil-water separation efficiency.[31,32]. Demulsifiers are chemical compounds that disrupt the surfactant layer surrounding droplets to destabilize the water-oil interface. For many freshwater and marine creatures, however, many of the standard demulsifiers are exceedingly poisonous compounds[33,34]. This is crucial for offshore refineries because the majority of their effluents end up in the ocean. The ineffectiveness of the oil-water separation process also

highlights the necessity of a strong upstream water-washing step to reduce the salinity of any droplets that might entrain with the oil and travel to oil processing units downstream. According to our estimates, the water-washing portion of the crude oil desalting process uses up to 150 billion gallons of fresh water yearly, water that would otherwise be used to meet the needs of almost 30 million people in developing and underdeveloped areas. Desalting crude oil is a costly process. The desalting market is currently valued at $2.6 billion, of which the demulsifier market, which largely serves the crude oil industry, is a $ 2 billion market. The second objective of this thesis is to develop an efficient mechanism for phase separation of water-in-oil nanoscale emulsion that completely eliminates the usage of toxic chemical demulsifiers.

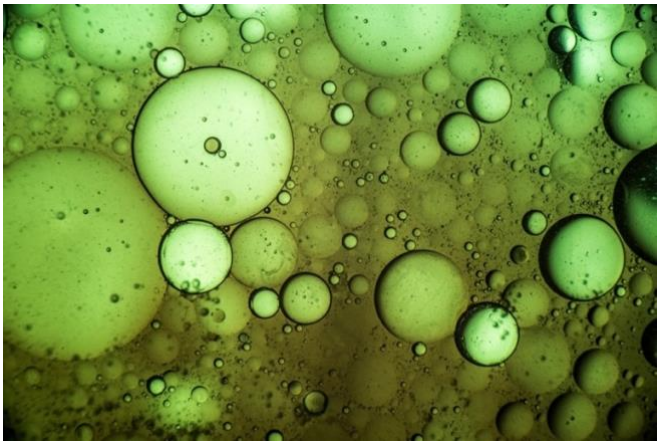

Figure 1-2. **Water in oil emulsion.** Formation of stable emulsion between water and oil is found across various industries. Separating the dispersed phase from the continuous phase especially when the dispersed phases is on the order of nanoscale, is a century old challenge. Image source: Adobe Stock Images licensed asset (#74557123).

In addition to crude oil processing, one of the biggest challenges associated with oil and gas industry is the $CO_2$ emission during the burning of fossil fuels. Global $CO_2$ emissions have reached about 41 Gt in 2021[35] placing an enormous strain on the Earth's climate stability [36,37]. One of the most efficient ways to reduce anthropomorphic emissions is through post-combustion carbon capture in power plants (Figure 1-3), as capturing the CO2 produced by a single 500 MW natural gas power plant over the course of a year is equivalent to removing emissions from 200,000 cars over the same time period. [38,39]. Chemical absorption into a liquid absorbent is generally regarded as the most promising technique among many methods for capturing CO2 due to the higher efficiencies, cheaper prices, and techno-economic maturity that it offers.[40–44]. The majority of

practical chemical absorption facilities use packed bed reactors. These reactors are tall towers filled with a number of packing units. At the top of the tower, sorbent solution is supplied, and it drips down over the surface of the packing units, forming liquid films that react with the rising flue gas stream. The packing units are made to increase the contact time and the interfacial area between the liquid absorbent and the flue gas[45]. Packed bed reactors must be big enough to allow for enough space and time for absorption to occur in order to capture >90% of the CO2 emitted from a power plant (where flue gas flow rates can range between 100 and 800 kg/s) [46–48]. As a result, packed bed towers frequently exceed 40 meters in height and 10 meters in diameter, accounting for around 30% of the total capital needed for such carbon capture systems [49,50]. Only 28 large-scale carbon capture plants are now operational worldwide due to unreasonably high prices[51]; therefore, shrinking the size of these absorption towers would make post-combustion carbon capture systems more viable[52]. The final aim of this thesis is to develop an efficient $CO_2$ capture method that reduces the size and capital expense of $CO_2$ absorption towers.

Figure 1-3. **$CO_2$ exhaust from power plants via flue gas.** Power plants are one of the biggest contributors of anthropogenic greenhouse effect amounting to the largest volume of per capita (per-unit) $CO_2$ emission compared to any other concentrated source. Image source: Adobe Stock Images licensed asset (#297555832).

In all three challenges described above, interfacial interaction is one of common themes that we can observe. In photovoltaic soiling, adhesion interaction occurs at the interface between dust particles and solar panel surfaces. In the case of nano-scale emulsions, emulsion stability is governed primarily by the stability of oil-water interface. Finally, in the $CO_2$ absorption systems,

the rate of $CO_2$ capture is governed by the rate of mass transfer at the sorbent liquid-flue gas interface. The scientific exploration of this thesis is at the nexus of electrostatics and interfacial science, where we introduce charge at the interfaces described in the above systems. In photovoltaic systems we explore the potential of introducing a charged solid-solid interface, i.e., introduction of surface charge on solar panels and dust particles as shown in Figure 1-4A. We aim to study the physics of particle charging and adhesion and devise a solution based on physical understanding from our scientific study. In nanoscale emulsions, we introduce strong charge polarization at the liquid-liquid interface, i.e., the interface between water droplets and oil medium as shown in Figure 1-4B. We aim to study the stability of nano-scale emulsions in presence of strong surface charge polarization and devise a solution to the nanoscale emulsion phase separation challenge based on our findings. Finally, in $CO_2$ capture systems, we introduce charge at the liquid-gas interface, i.e., between the flue gas and the sorbent liquid as shown in Figure 1-4C. We aim to study how the sorbent liquid can be much more effectively utilized by introducing them as small droplets of high surface area and leverage the interfacial charge to collect the charged droplets at high efficiency.

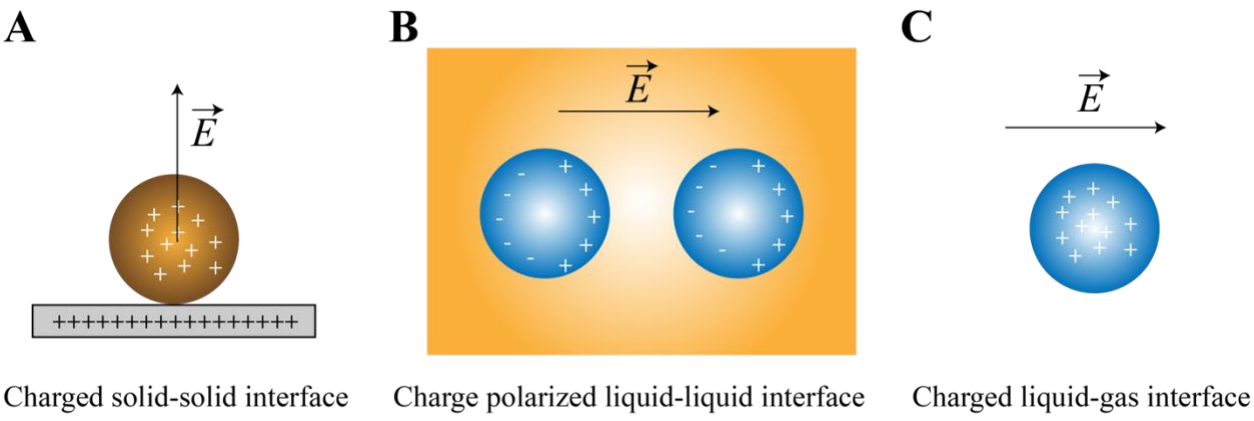


Figure 1-4. **Leveraging charged interfaces for attaining sustainability in various energy industries**. This thesis explores three types of charged interfaces for tackling challenges in three different domains in the energy industry. (**A**) We use interfacial charge exchange between solids for charging and repelling dust from solar panels, making photovoltaics more efficient. (**B**) We enable the application of strong electric field via non-Laplacian electrostatic space charge emitter to polarize and coalesce nanoscale droplets to phase separate water-in-oil emulsions in oil and gas industry. Here the liquid-liquid interface between water and oil is charged due to polarization. (**C**) We introduce sorbent liquid in the form of mist droplets to maximize the flue-gas interaction and

charge the droplets to electrostatically collect them with high efficiency. Here the liquid-gas interface between droplets and flue gas is a charged interface.

## 1.2. Thesis Structure

The content of this thesis is organized into 4 chapters: from chapter 2 to chapter 5. The first part of this thesis focuses on methods of removing dust from solar panels for improving their operational efficiency. Since most of the big solar power plants are located in dust-laden desert-like regions, dust accumulation is one of the single biggest operational challenges faced by the photovoltaic industry. Conventional cleaning method using water is expensive, and results in a 30-billion-gallon annual water footprint on photovoltaics, threatening the sustainability of photovoltaics. Chapter 2 and Chapter 3, which form the first part of this thesis, focus on studying the nature of adhesion of dust particles on surfaces and developing a waterless solar panel cleaning technology that works based on electrostatic charge induction for making photovoltaics truly sustainable.

In Chapter 2 we investigate the charge transfer via induction between a conductive surface and dust particles as a function of applied voltage. We find that despite primarily consisting of electrically insulating silica material, dust particles behave like conductive material due to adsorption of moisture from the ambient. We identify the critical humidity to make charge induction possible on dust particles. We performed systematic studies inspired from Stokes' experiments to measure the interfacial charge exchange and charge accumulation on dust particles. Thus, we identify the electric field needed to be applied to achieve sufficient charging for complete particle repulsion. Based on our findings, we define a non-dimensional critical voltage criterion for electrostatic dust removal. We designed and fabricated an autonomous electrostatic dust removal system as shown in Figure 1-5 and demonstrate that more than 95% of the lost power output can be recovered electrostatically, without consuming a single drop of water.

Improving the performance of electrostatic dust removal systems is the focus of Chapter 3. In Chapter 2, we find that even though electrostatic charge induction is very effective for removing most of the dust particles, small dust particles, especially less than 30 microns in size are very challenging to remove. This is because the Van der Waals force, a universal force of attraction that exists between all kinds of materials, prevents the electrostatic dust repulsion of small dust

particles. Van der Waals force of adhesion scales as proportional to the particle size, whereas the electrostatic force of repulsion scales with the surface area of particles since charge carriers rearrange themselves on the particle-air interface. As particle size reduces, the surface area reduces even more that the reduction in particle size. At a critical particle size, Van der Waals force dominates electrostatic force of repulsion. The focus of Chapter 3 is to systematically study the adhesion of dust particles on surfaces of different scales of morphology and identify the best suited surface morphology that reduces adhesion and enables effective electrostatic dust removal in the small particle regime. We find that nanoscale texture reduces the adhesion of dust microparticles by two orders of magnitude and therefore enables significantly better electrostatic dust removal.

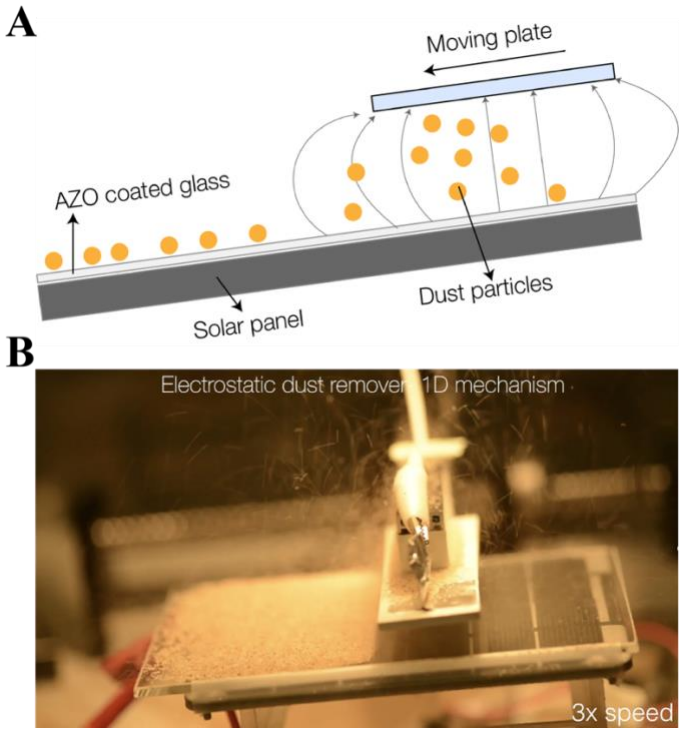


Figure 1-5. **Electrostatic dust removal from solar panels via charge induction.** (**A**) and (**B**) Dust particles acquire charge from the charged transparent solar panel surface via electrostatic induction and repel off from the solar panel. This concept is leveraged to design an autonomous electrostatic solar panel dust removal mechanism that recovers more than 95% of the lost power output without consuming a single drop of water.

Chapter 4 forms the second part of the thesis. In this chapter, the focus is on electrostatic phase separation of water-in-oil emulsion. Oil-water mixing is a problem that occurs in various

industries such as food industry and oil-and-gas. Separating the dispersed water phase from the continuous oil phase (or vice-versa), especially when the dispersion forms nano-scale emulsion is a century old challenge. Gravity-based separation is impractical due to small emulsion droplet sizes. Conventional electrocoalescers use immersed electrodes. However, the limited electric field strength applied in traditional electrocoalescing makes them ineffective for nanoscale emulsions. In this chapter, we present a non-Laplacian space charge injection based electrocoalescence that drastically enhances the rate of demulsification of nanoscale emulsions and eliminates the use of toxic chemical demulsifiers as shown in Figure 1-6A. We demonstrate that by introducing space charge emitter electrodes with an air gap between the electrodes and the emulsion we can avoid the droplet-mediated electrical shorting and apply an electric field 8 times stronger. The application of strong electric field causes strong interfacial charge polarization, resulting in strong droplet-droplet dipole attraction due to the interfacial charge as shown in Figure 1-6B. We show that this charge separation and resulting droplet-droplet attraction results in much faster phase separation of water-in-oil nanoscale emulsions (Figure 1-6C and Figure 1-6D) at different water fractions ranging from 2%-20%. We visualize the droplet chaining and coalescence events and demonstrate that the rate of oil-water separation scales with the square of applied voltage, showing that the enhanced electric field quadratically enhances the rate of electro-coalescence. Finally, we design a flow-through space-charge emitter electrocoalescer that enables rapid, continuous demulsification.

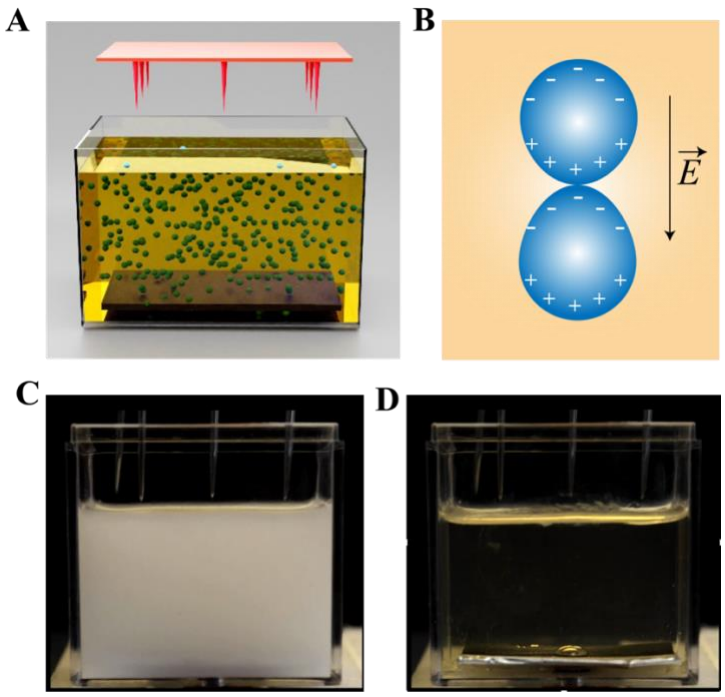


Figure 1-6. **Non-Laplacian electrostatic space charge injection mechanism for efficient phase separation of water-in-oil nanoscale emulsion.** (**A**) Sharp emitter electrode array for introducing non-Laplacian electrostatic space charge injection. This enables application of stronger electric field across the emulsion. (**B**) Application of strong electric field enables stronger polarization and coalescence of nanoscale droplets. (**C**) Water-in-oil nanoscale emulsion is extremely stable against gravity settling. Traditional electro coalescence technique fails to phase separate nanoscale emulsions. (**D**) By application of strong electric field, the water and oil phases separate rapidly, resulting in a clear solution.

Chapter 5 forms the third and final part of this thesis. Carbon dioxide capture from exhaust stack for coal and natural gas power plants is one of the most scalable ways of curbing anthropogenic $CO_2$ emission. However, this is very expensive to accomplish in practice due to the prohibitively expensive capital and operational expense associated with absorption towers. In this chapter, we propose and alternative approach to capturing $CO_2$ into the sorbent liquid by potentially eliminating the absorption tower altogether or significantly reducing its size. $CO_2$ absorption is a phenomenon where the available surface area of interaction is one of the biggest bottlenecks. We propose that the interfacial area of interaction between sorbent liquid and the flue gas can be tremendously increased by introducing the sorbent liquid as tiny mist droplets instead of as a flowing film. However, since the stokes number of tiny mist droplets are much smaller than

large 100-micron droplets, they are easily entrained with the flow and will escape along with the flue gas despite absorbing $CO_2$. Passive demisters that capture liquid from gas stream are incredibly inefficient or they introduce significant backpressure. To systematically study and characterize our proposed approach, we designed a bench-scale $CO_2$ capture device, where we use KOH solution as the $CO_2$ capture solvent. We introduce KOH mist droplets into a mixture of air and $CO_2$ and show that we can capture >95% $CO_2$ from the air stream. To prevent the entrainment and loss of mist droplets, we introduce an electrostatic mist capture unit. The droplets are charged by electrostatic space charge injection and are captured at >99% efficiency (shown in Figure 1-7) due to high Deutsch-Anderson factor. Finally, we perform a detailed techno-economic analysis and show that our mist-based method can reduce the size of $CO_2$ capture systems by up to 5x, reduce the capital expenditure by ~60% and also open the door to a whole new set of environmentally benign catalysts for $CO_2$ capture.

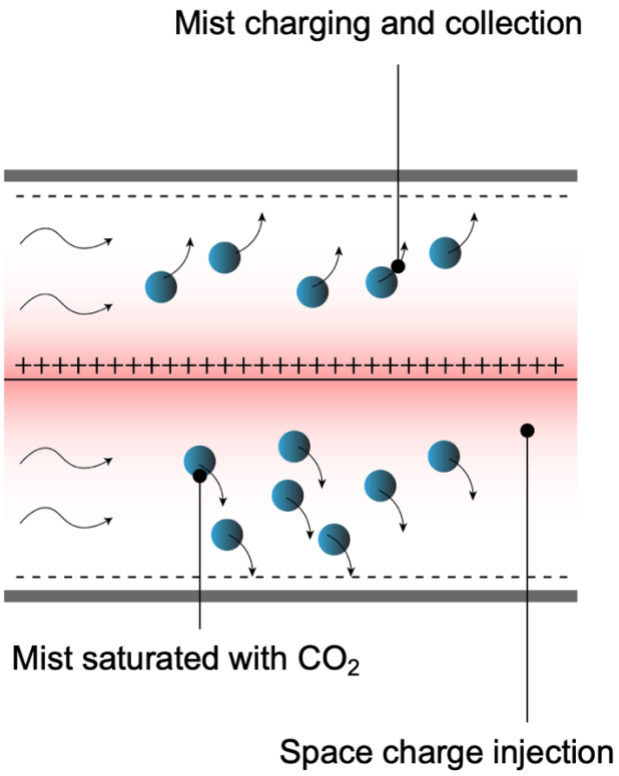


Figure 1-7. **Mist-scale droplets enhance the $CO_2$ absorption rate from flue gas.** Flue gas-sorbent interaction can be maximized by maximizing the surface area to volume ratio of the sorbent liquid using mist. Since mist droplets easily entrain with the gas flow, capturing them efficiently

is impossible with passive demisters. We design an in-line electrostatic demister that injects space charge to charge and electrostatically collect the mist droplets.

THIS PAGE INTENTIONALLY LEFT BLANK

## 2. Electrostatic dust removal using adsorbed-moisture-assisted charge induction for sustainable operation of solar panels

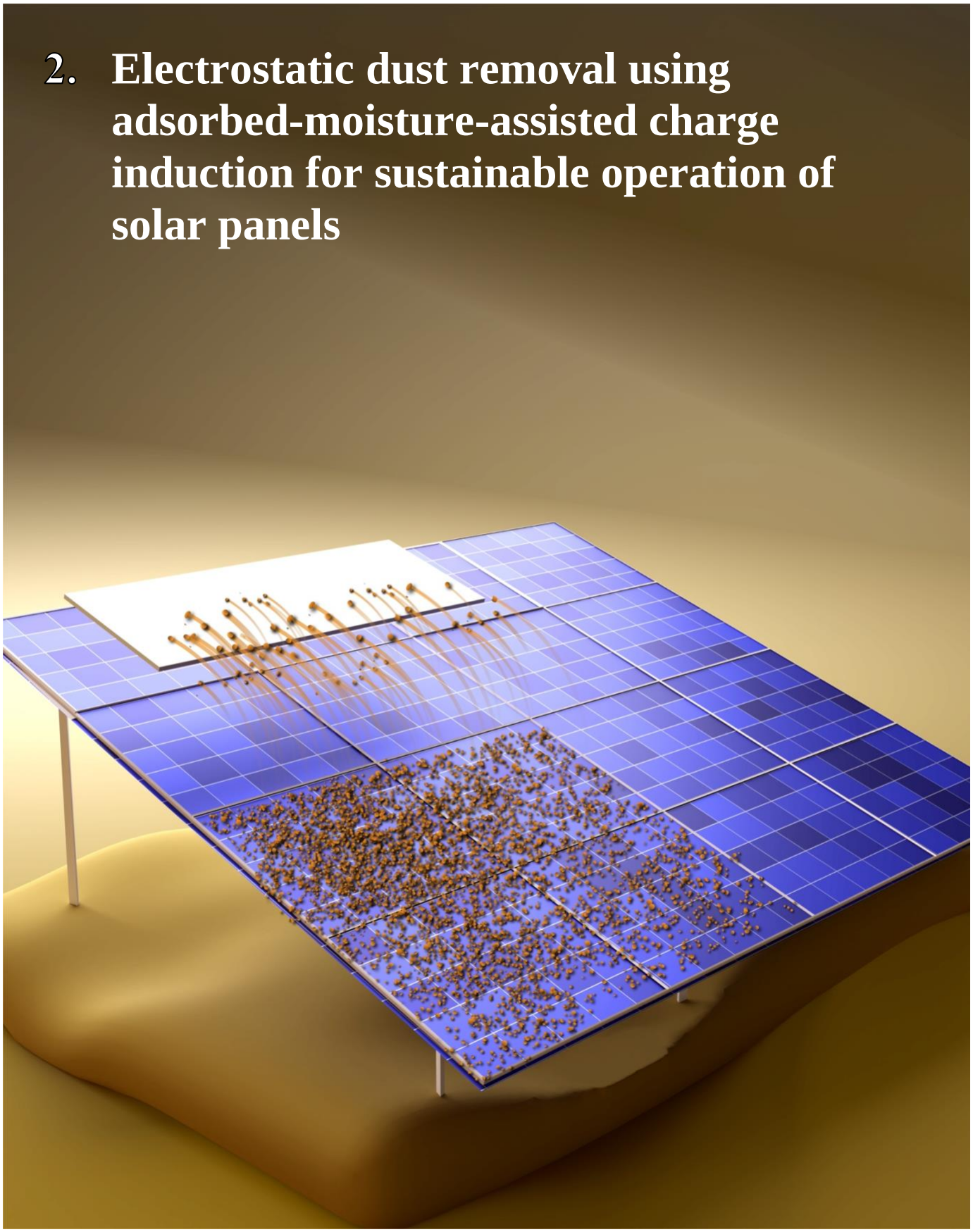

## 2.1. Abstract

Dust accumulation on solar panels is a major challenge as it blocks a large portion of sunlight. Solar panels are therefore cleaned regularly using large quantities of pure water. Consumption of water for cleaning, especially in deserts, poses a significant sustainability challenge. In this chapter, we present a waterless approach for dust removal from solar panels using electrostatic induction. We find that dust particles, despite primarily consisting of insulating silica, can be electrostatically repelled from electrodes due to charge induction assisted by adsorbed moisture. We experimentally determine dust particle charge by conducting Stokes experiments under an electrostatic field. By considering electrostatic, Van der Waals, and gravitational forces, we define the threshold electric potential for particle removal. We also demonstrate dust removal over a broad range of relative humidity, making our approach widely applicable. Finally, we develop a lab-scale prototype and demonstrate up to 95% recovery of lost power output using our approach.

## 2.2. Introduction

### 2.2.1. Photovoltaics growth

As a result of collective efforts to move towards clean energy, renewable energy systems have shown tremendous growth (Figure 2-1) [53], reaching a capacity of 25% of global power output in 2018 [5]. Photovoltaic (PV) systems have played a key role in this growth by increasing their global power production capacity from 9 GW in 2007 to 509 GW by the end of 2018 [54]. It is projected that solar power will amount to 10% of global electricity generation by 2030 [55] in comparison to 2.2% in 2018 [56]. Along with the increase in number of PV installations there is also great focus on making cheaper and more efficient solar panel systems [57] including efforts for improving the power conversion efficiency of PV cells [58], use of antireflective coatings for minimizing reflective loss [59], keeping solar panels cool by active and passive methods [60], actively changing the angular positioning to track sun [61], nanotexturing the silicon for maximizing absorbance [62,63] etc.

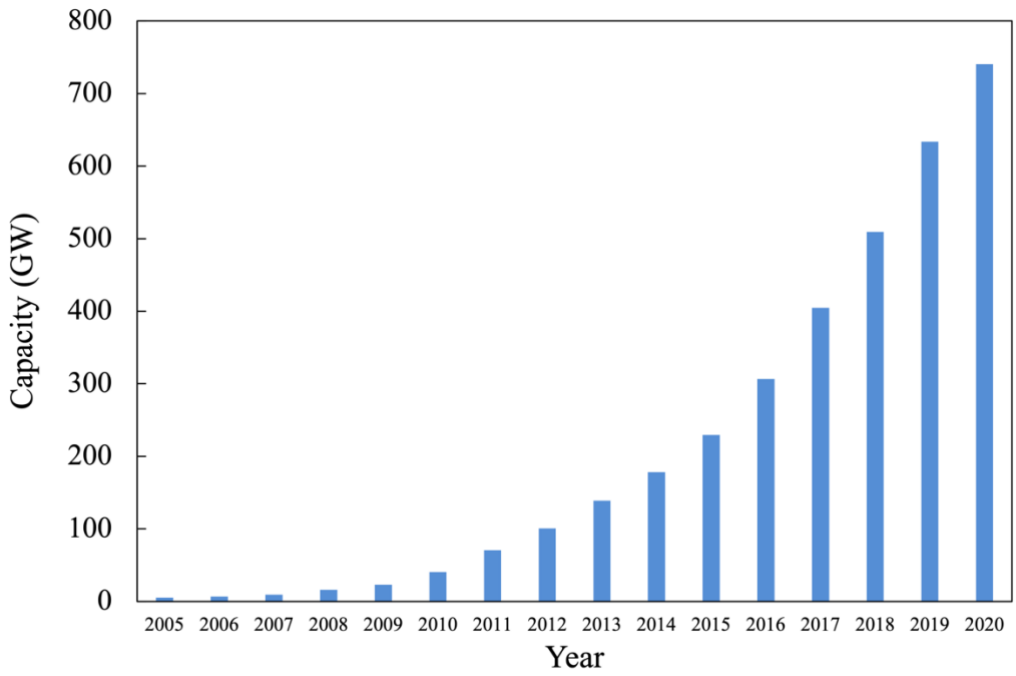


Figure 2-1. **Photovoltaic global capacity growth from 2005-2020** (IEA report) [53]

### 2.2.2. Dust accumulation: a global challenge

Despite all of the recent improvements in PV technology, dust accumulation on solar panel surfaces blocks a significant portion of incident sunlight and remains a major operational challenge for the industry [6–9] (Figure 2-2). Many large-scale solar farms are located in geographical regions that have an abundance of land and sunlight, such as deserts. The list includes some of the biggest solar power projects in the world such as in Tengger Desert Solar Park (China), Bhadla Solar Park (India), Dubai Solar Park, Desert Sunlight Solar Farm (US); which are all located in deserts. Even though the abundance of sunlight in these locations is favorable for solar power production, these regions also tend to have significant air-borne mineral dust [12] that gradually accumulates on solar panel surfaces, reducing their efficiency. We performed an accelerated in-lab study that simulated harsh soiling conditions on a lab-scale solar panel and found that the power output decreases exponentially with dust coverage as shown in Figure 2-3A and Figure 2-3B. In harsh environments

with dust accumulation rates close to 1 g/m$^2$/day[17], it takes only about a month for dust accumulation of 3 mg/cm$^2$ to occur [13,14]. For example, as shown in Figure 2-3B, dust accumulation of 5 mg/cm$^2$ corresponds to almost 50% loss in power output. There can also be rapid loss of efficiency in regions where dust-storms are frequent [64]. It has been shown that an average power loss of 3%-4% on a global scale amounts to an economic loss of 3.3-5.5 billion USD [6]. Thus, solar panels are usually cleaned regularly (up to several times a month) depending on the severity of soiling conditions [6].

Figure 2-2. **Dust accumulation on solar panels at Atacama solar park, Chile**

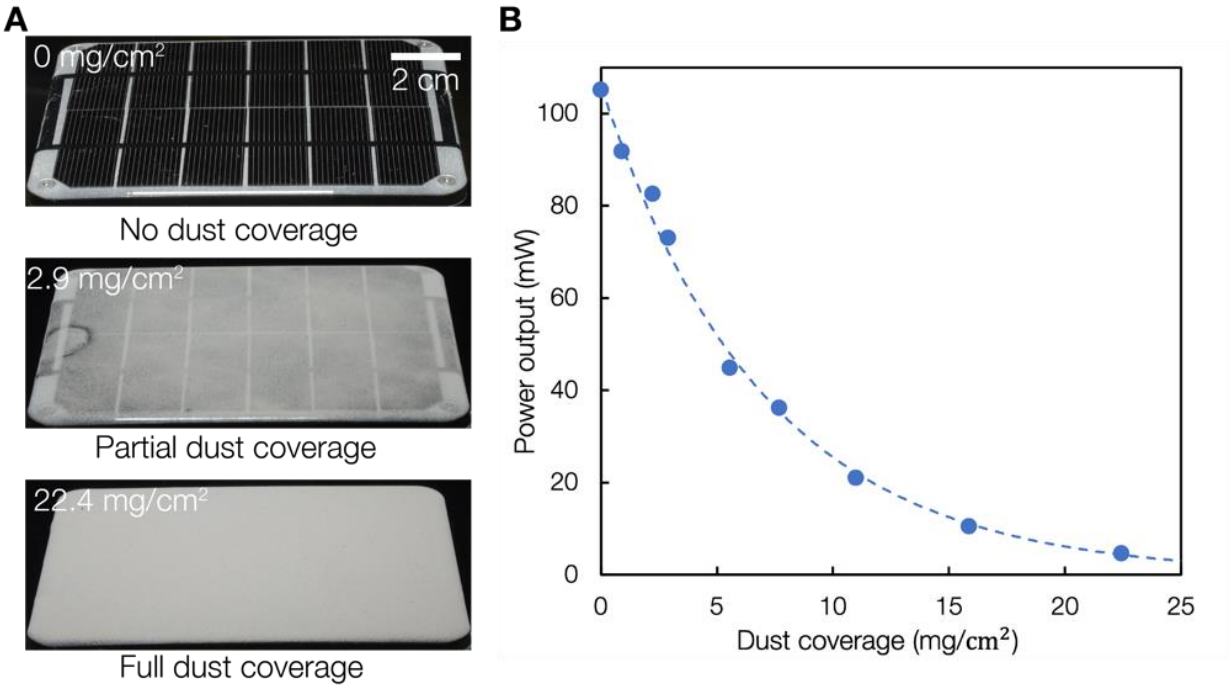


Figure 2-3. **Effect of dust accumulation on solar panel power output.** (**A** and **B**) Spreading dust particles (~15 um size) uniformly on the surface of a lab-scale solar panel reduces power output exponentially with increasing dust coverage due to increased blocking of incident light. Here we used a fluorescent lamp as the light source.

### 2.2.3. Solar panel cleaning methods

The most common method of cleaning is using pressurized water jets and sprays [13]. Since water is scarce in desert regions it has to be transported from elsewhere before being sprayed onto solar panels. Water-based cleaning contributes up to 10% of the operation and maintenance cost of solar farms based on cleaning frequency [6,15]. Studies report that both PV and concentrated solar power plants consume about 1-5 million gallons of water per 100 MW per year for cleaning [15,16]. At a global PV capacity above 500 GW [54], we estimate based on reports [15,16] that up to 10 billion gallons of water are being consumed every year world-wide for solar panel cleaning purposes, which can otherwise satisfy the annual water needs of up-to 2 million people in developing and under-developed countries. As the solar install base grows, water consumption by solar farms is only expected to rapidly increase. In order to eliminate water consumption some small scale farms have implemented manual or robotic dry scrubbing [6,65]. However, dry scrubbing is less effective at removing dust and introduces irreversible surface scratching [66] that reduces the light

transmittance over time. Currently, the lack of efficient approaches for maintaining dust-free solar panels remains a major challenge in the global effort to drive down the cost of solar energy [6]. Therefore, there is a pressing need for alternate cleaning approaches that can eliminate the giant water footprint of the solar industry not only to reduce the operational costs, but also to be truly sustainable.

### 2.2.4. Electrostatic solar panel cleaning: state of the art and challenges

Electrostatic solar panel cleaning has been proposed as an exciting alternative that can potentially eliminate the consumption of water as well as contact scrubbing damage due to the absence of mechanical components that rub against the panel. Electrodynamic screens (EDS) are the most popular electrostatic dust removal systems (shown in Figure 2-4). Some approaches for implementing EDS involve fabricating arrays of interdigitated transparent Indium Tin Oxide (ITO) micro-electrodes that are embedded in a dielectric film or installing insulated copper mesh electrodes on top of solar panel surfaces [67–70]. Upon activating the electrodes, the electric field propels the dust particles via weak, short range dielectrophoresis and/or weak, passive triboelectric charging. While the EDS systems are promising and have been successfully implemented in extremely dry environments such as solar panels on Mars rovers [71,72], there are several challenges for implementation in solar panels on Earth. A key challenge is moisture intrusion over time into the dielectric film that insulates the electrodes due to its finite porosity. Moisture accumulation could eventually lead to electrical shorting of the electrodes and failure of the system [73,74]. Furthermore, embedded interdigitated micro-electrode arrays in EDS are expensive for commercial implementation due to the costs associated with microfabrication [6]. In the case of interdigitated copper electrodes there are also limitations arising from significant shadowing of the surface.

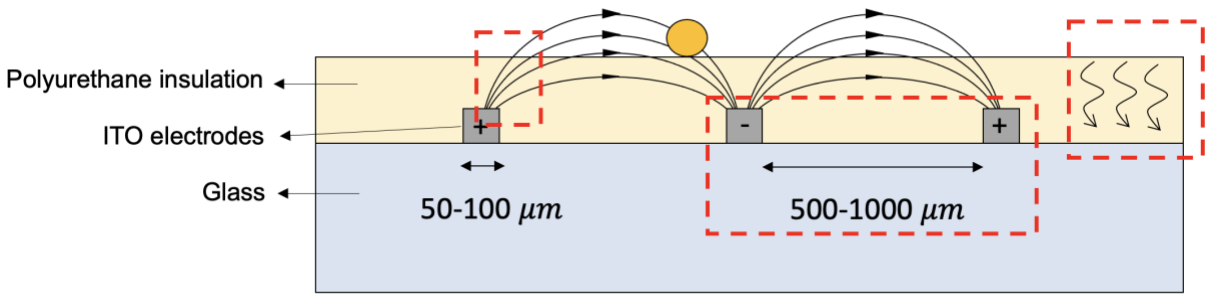


Figure 2-4. **Electrodynamic Screen (EDS) installed on top of the solar panel surface**. The mechanism of dust removal is primarily via dielectrophoresis. Transparent microelectrodes are embedded in a thin transparent polyurethane film. The polyurethane film has finite permeability to moisture.

### 2.2.5. Our approach: electrostatic dust removal using active charging

In this chapter, we propose a novel electrostatic approach to "actively charge" dust particles and impart strong Coulombic force for dust repulsion. Our approach overcomes the prior limitations that occur due to reliance on relatively weak, short range dielectrophoretic/triboelectric force and eliminates the issue of electrical shorting. Our work was motivated by the experiment shown in Figure 2-5A where we observed that dust particles resting on the bottom electrode in a parallel-plate setup are repelled from the surface on application of sufficient voltage (Movie 2-1). This occurs due to induction that causes charge accumulation on the dust, as shown in the schematic of Figure 2-5B. When we performed similar experiments by replacing dust particles with conductive iron or insulating Teflon particles, we observed that dust particles qualitatively behaved like iron rather than Teflon. Both dust and iron particles lift off (Figure 2-6) and are removed from the electrode surface when the applied voltage exceeds certain threshold value as shown in Figure 2-5C.

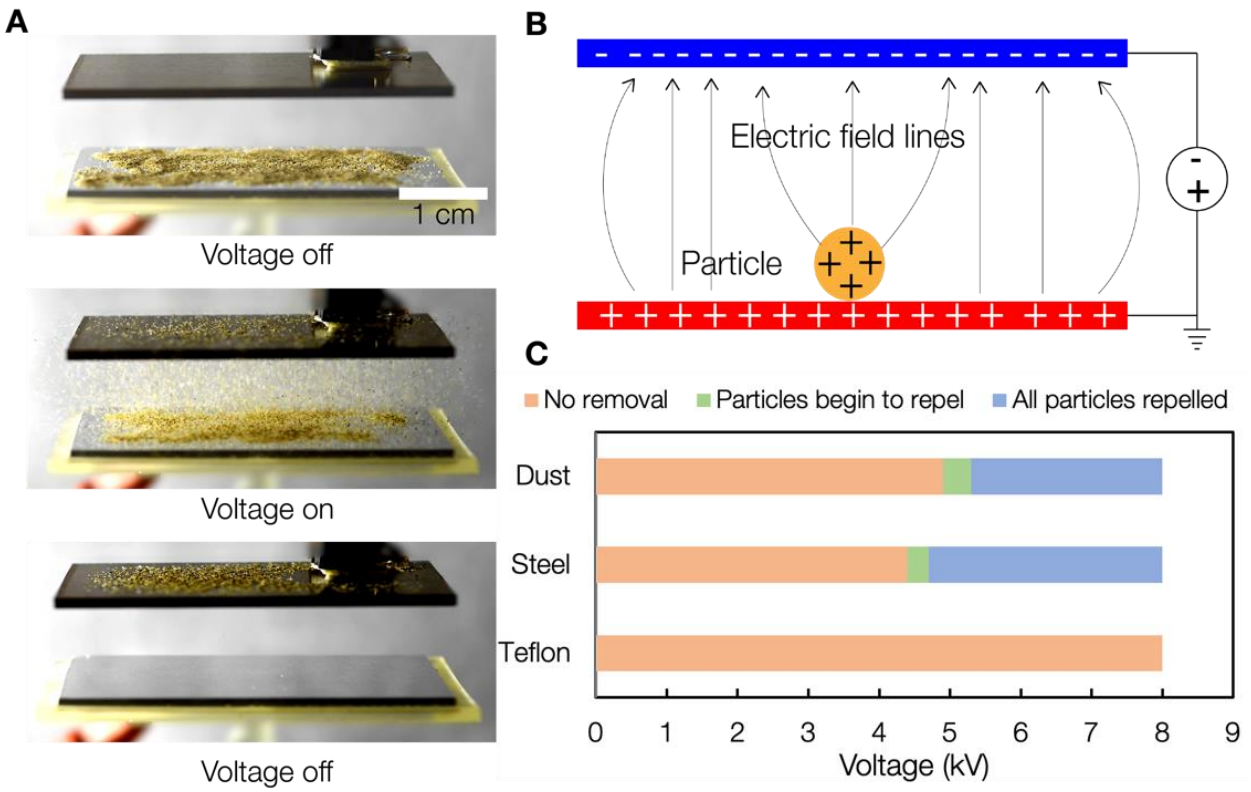


Figure 2-5**. Repulsion of dust by electrostatic charge induction.** (**A**) Dust particles spread on the bottom metallic electrode are observed to repel on application of voltage (~12 kV) between the plates. (**B**) The electrostatic repulsion results from charging by induction, where charge of same polarity as that of the contacting electrode accumulates on the dust particle. (**C**) The behavior of dust particles is similar to that of conductive iron particles where particle lift-off happens when the applied voltage reaches a threshold value that enables particles to overcome the force that adhere them on to the surface.

Even though "dust" is a term that encompasses a wide variety of particulate matter, typical desert dust particles that foul solar panels are mineral particulate matter [7,12,64,75]. There can be variation in mineral/chemical composition of the particles depending on the geographical location [12]. However, mineral dust particles commonly consist of a significant fraction (~30%-75%) of silica [76,77], which is known to adsorb moisture [78] (Figure 2-7).

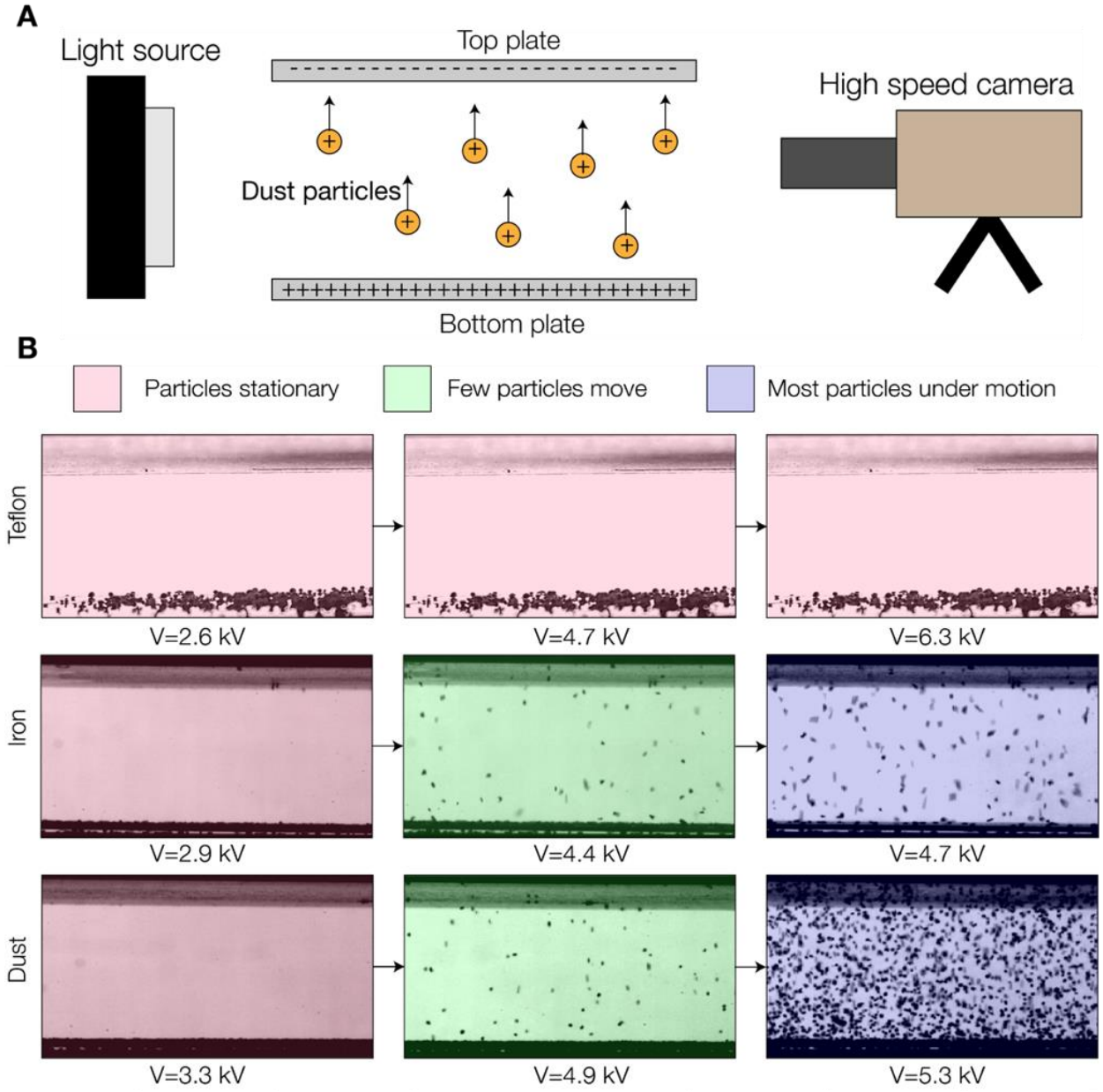


Figure 2-6. **Behavior of Teflon, steel, and dust particles on contact with a metallic electrode. (A)** Experimental setup for imaging the particle motion as particles oscillate between the plates. **(B)** High speed images of Teflon ( >50 μm), steel/iron (~253 μm) and dust particles (~253 μm). Teflon particles are stationary for the entire range of applied voltage- indicating negligible charging by induction as we expect for an insulating material. Steel particles take off from the surface at certain threshold voltage indicative of conductive behavior where electrostatic force overcomes the Van der Waals adhesive force. Dust particles also behave similar to conductive iron particles.

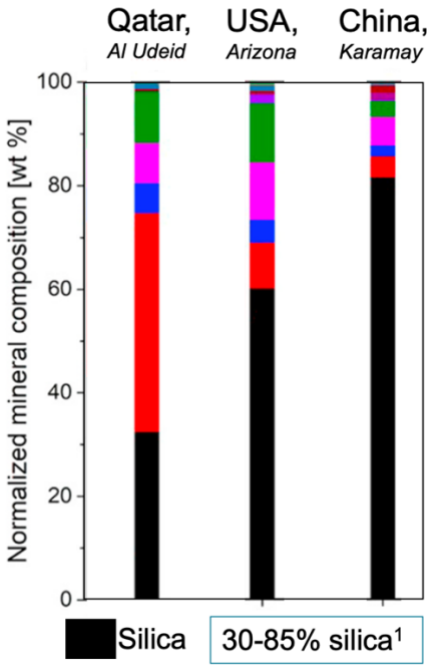


Figure 2-7. **Typical mineral dust composition from various deserts**. It can be seen that a significant portion of the chemical composition of dust particles are made of silica. [12]

Even though pure silica is a good insulting material, adsorbed moisture reduces its electrical resistivity [79] and it becomes charged upon contact with an electrode [80]. We use Arizona test dust (Intermediate and miscellaneous test dust fractions from Powder Technology Inc.) also known as crystalline silica dust whose chemical composition emulates that of typical desert mineral dust particles in our experiments.

We make use of the conductor-like behavior of dust particles to repel them from solar panel surfaces. First, we estimated the charge on dust particles and then defined the condition for particle removal in terms of applied voltage. We then varied the relative humidity to study the effect of variation in moisture adsorption on electrostatic dust removal. Finally, we designed an electrostatic dust removal system for a lab-scale solar panel by transforming the top surface of the panel into a transparent electrode[17].

## 2.3. Results and Discussion

### 2.3.1. Estimation of charge on dust particles

In order to design an electrostatic cleaning system where voltage is the primary control parameter, we systematically study the electrostatic dust removal process. As shown in the free body diagram of a dust particle (Figure 2-8A) the electrostatic force ($F_E$) acting to remove the particle from the surface is opposed by the forces of adhesion ($F_A$) and gravity ($F_G$) that tend to keep the particle on the surface. As shown in Figure 2-5C, the presence of a critical threshold voltage shows that the particle lifts off from the surface when charge induction results in a strong enough electrostatic repulsive force to overcome adhesion and gravity.

The gravitational force can be determined by knowing the density (assuming silica) and approximate size of the dust particle ($\rho \sim 2650 \frac{kg}{m^3}$ , $F_g = \rho \frac{4}{3} \pi R^3 g$). Similarly, at the moderate relative humidity range where we performed our experiments (45%-55%, unless specified), the force of adhesion of micro-particles with surface roughness is primarily governed by Van der Waals force [81–83]. Van der Waals force for microparticles is very well characterized and can be estimated by using Hamaker's [84] model, after incorporating a correction factor for surface roughness as proposed by Rabinovic et al [85]. Finally, electrostatic force is given by the product of particle charge and applied electric field ($F_E = QE$). In our parallel-plate electrode configuration, the electric field strength is easily determined. However, since the electrical conductivity of dust particles is not well characterized, the particle charge ($Q$) remains unknown. Thus, in order to be able to predict the electrostatic force and thereby the dust-removal voltage, particle charge needs to be estimated.

To estimate the charge $Q$ for dust particles, we performed particle-repulsion experiments by immersing the electrodes in a silicone oil bath [80] (see Experimental Methods) as shown in Figure 2-8B. As potential difference was applied between the plates, particles acquired charge and bounced back and forth between the plates. Figure 2-8C shows the snapshot of high-speed images taken from one of these experiments.

Viscosity of the oil (500 cSt) was chosen to be high enough to minimize the effect of inertia and thus particles attained terminal velocity of motion between the plates quickly compared to the

total travel time of particles between the plates (see Movies 2-3 and 2-4). To avoid particle acceleration, the motion of particles in the oil bath should be dominated by viscosity and hence the oil bath viscosity needs to be in general high. The criterion for selecting the viscosity is derived as follows.

Considering electrostatic, gravitational, viscous, buoyant, and inertial forces, we can write the equation of motion of a particle moving up in the oil bath as Equation 2.1.

$$qE - mg - 6\pi\mu RU + \frac{4}{3}\rho_o \pi R^3 g = ma \tag{2.1}$$

We write the acceleration in terms of the terminal velocity ($U$) and the time scale over which acceleration happens ($\tau$) as shown below (Equation 2.2).

$$a \sim \frac{U}{\tau} \tag{2.2}$$

Before particle reaches a steady velocity, inertial term is comparable with electrostatic force (Equation 2.3).

$$qE \sim ma \sim m\frac{U}{\tau} \tag{2.3}$$

Thus, the time scale for acceleration is given as shown in Equation 2.4.

$$\tau \sim \frac{mU}{qE} \tag{2.4}$$

If $S$ is the gap between top and bottom electrodes, the total time ($t$) taken by particle to move the full distance is given by Equation 2.5.

$$t \sim \frac{S}{U} \tag{2.5}$$

For particle motion to be predominantly viscous dominated, we want $\frac{\tau}{t} \ll 1$, thus we get the condition shown in Equation 2.6.

$$\frac{mU^2}{qES} \ll 1 \tag{2.6}$$

But we also know that if the particle motion is viscous dominated, then scaling of electrostatic force and viscous drag will be the same. Hence $qE \sim 6\pi\mu RU$ and thus $U \sim \frac{qE}{6\pi\mu R}$. Using this in Equation 2.6 we get Equation 2.7.

$$\frac{m}{qES}\left(\frac{qE}{6\pi\mu R}\right)^2 = \frac{qEm}{(6\pi\mu R)^2 S} \ll 1 \tag{2.7}$$

On rearranging, we have the condition for viscosity as Equation 2.8.

$$\mu \gg \frac{1}{6\pi R}\sqrt{\frac{qEm}{S}} \tag{2.8}$$

Here if we assume that dust particles are perfectly conducting, $qE \sim 4\pi R^2 \epsilon_0 \epsilon_r E^2$. Mass of the particle can be written in terms of the particle size and density. Thus, equation 2.8 can be simplified into Equation 2.9.

$$\mu \gg \frac{1}{6\pi R}\sqrt{\frac{16\pi^2 \epsilon_0 \epsilon_r E^2 \rho R^5}{3\,S}} = \frac{2}{3}E\sqrt{\frac{\epsilon_0 \epsilon_r \rho R^3}{3S}} \tag{2.9}$$

By plugging in the following values for the variables in Equation 2.9, we get a numerical condition for the dynamic viscosity of the silicone oil that needs to be chosen (Equation 2.10).

$$E \sim 10^6 \frac{V}{m}, \rho \sim 2600 \frac{kg}{m^3}, \epsilon_0 \epsilon_r = \epsilon_{oil} \sim 2.6 \times 10^{-11} \frac{F}{m}, R \sim 200\ \mu m, S \sim 1.5\ cm$$

$$\mu \gg 2.31 \times 10^{-3} Pa.s \tag{2.10}$$

Consider silicone oil of density $970 \frac{kg}{m^3}$, $\nu \gg 2.38 \times 10^{-6} \frac{m^2}{s}$ $or$ $\nu \gg 2.38\ cSt$. Thus, we choose silicone oil of viscosity 500 cSt (>>$2.38\ cSt$) for our experiments. As explained in Experimental Methods section, we empirically identify that too high viscosity (~1000 cSt), makes it harder for the particles to displace the thin oil film between particle and the electrode.

Thus, to measure the charge on particle moving in high viscosity silicon oil we start with force balance. We balance the electrostatic force with Stokes drag force, gravitational force, and buoyancy force as $Q\bar{E} + m\bar{g} + 6\pi\mu R\bar{U} + \bar{F}_B = 0$. We measure the terminal velocity of particles

from high-speed images and estimate the charge on particles that lift off from the surface as shown in Equation 2.11.

$$Q = \frac{6\pi\mu RU + (\rho - \rho_{oil})\frac{4}{3}\pi R^3 g}{E} \qquad 2.11$$

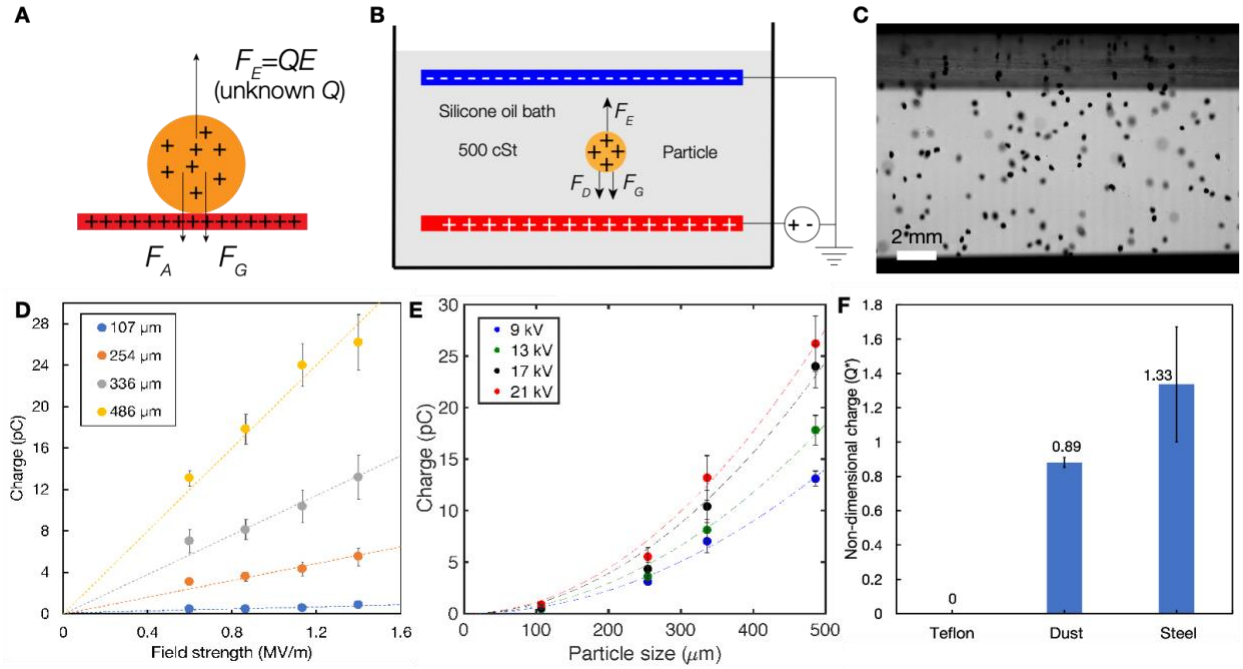


Figure 2-8. **Charge estimation experiments.** (**A**) Schematic of the forces acting on a dust particle with forces of adhesion ($F_A$) and gravitation ($F_G$) acting against the electrostatic force ($F_E$). Here, in-order to determine $F_E$, charge $Q$ needs to be estimated. (**B**) Schematic of the experimental setup with parallel plates immersed in silicone oil bath for estimating particle charge. (**C**) Snapshot from high-speed imaging of dust particles (~327 um) bouncing between electrodes spaced at 1.5 cm. (**D**) Estimated charge ($Q$) for different sized dust particles plotted against applied electric field strength $E$. $Q$ scales linearly with $E$ for dust particles similar to what we expect for conducting particles. (**E**) $Q$ scales proportional to the square of particle size (~$R^2$) indicating the conductor-like behavior. (**F**) Based on $Q_{th} \sim 4\pi R^2 \epsilon_0 \epsilon_r E$ we define a non-dimensional charge $Q^* = Q/Q_{th}$ which scales as $Q^* \sim 1$ (here $\epsilon_r \sim 3$ for oil). We see that while teflon shows no sign of charging ($Q^* \sim 0$), $Q^* \sim 1$ for both dust and metallic particles shows that dust particles are exhibiting conductor-like behavior. Error bar corresponds to standard deviation over 3 experiments and 5 different particles per experiment.

Figure 2-8D plots the charge against the applied electric field strength for dust particles of different sizes. The charge is found to be linearly proportional to the applied electric field strength,

as in conducting materials. Similarly, Figure 2-8E plots the estimated charge against the particle radius. The accumulated charge is quadratically proportional to the radius ($Q \sim R^2$). This confirms that charge accumulation occurs on the particle surface rather than in the bulk volume of the particle, similar to conducting materials [86].

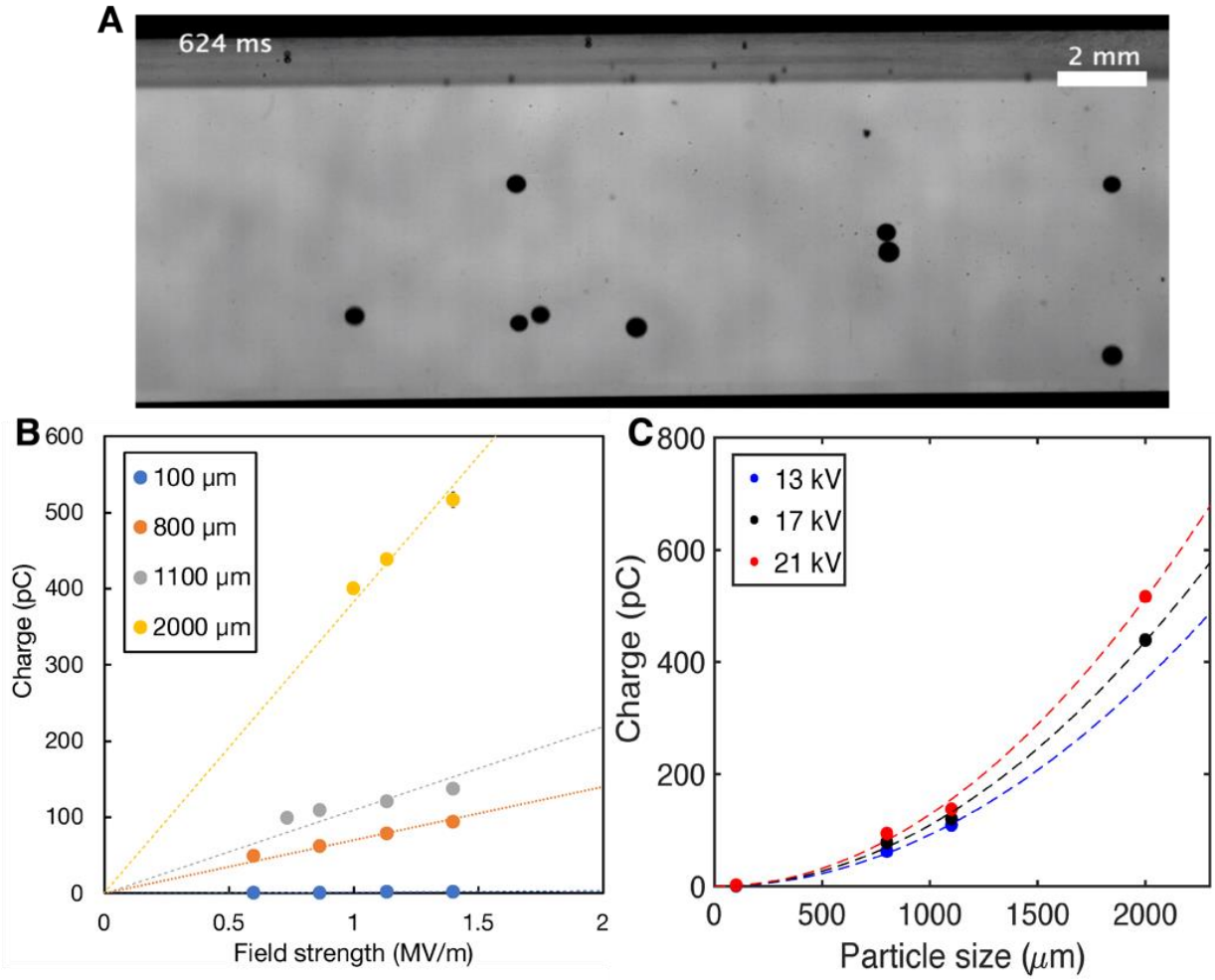


Figure 2-9. **Charge estimation experiments for steel particles.** (**A**) Steel beads of average size 550 microns oscillating between parallel plate electrodes separated by 1.5 cm gap immersed in silicone oil of viscosity 500 cSt. (**B**) Charge ($Q$) is estimated from force balance. $Q$ scales linearly with electric field strength ($E$). (**C**) Charge scales with surface area of particle ($\sim R^2$) since charge carriers rearrange themselves on the surface to eliminate the tangential component of electric field at the surface.

Finally, to compare the magnitude of charge on dust particles with that of particles of known electrical conductivity $\sigma$, we performed silicone oil bath experiments using teflon ($\sigma \sim 10^{-24}\,\frac{S}{m}$, good insulator) and steel ($\sigma \sim 10^{6}\,\frac{S}{m}$, good conductor) spheres (Figure 2-9). While

Teflon particles remained stationary at the bottom electrode indicating negligible charge induction, steel particles bounced between the electrodes similar to dust particles. We estimate the charge $Q$ using force balance. We define a non-dimensional charge ($Q^*$) based on the experimentally estimated charge and the theoretical approximation for charge on a perfect conductor ($Q_{th} \sim 4\pi R^2 \epsilon_0 \epsilon_r E$) [86,87] as $Q^* = \frac{Q}{Q_{th}}$. In Figure 2-8F we plot $Q^*$ for Teflon, dust, and steel particles. While charge on Teflon is ~0, charge on both steel and dust particles scales as ~1. Even though the exact numerical value of the non-dimensional charge is higher for steel particles, the scaling of charge indicates that dust particles act very much like a conductor and that the actual charge is well approximated by the expression for $Q_{th}$.

The similarity in charging behavior between dust and steel particles is also explained by charge relaxation time ($\tau = \frac{\epsilon}{\sigma}$). Charge relaxation time is the characteristic timescale for a particle to reach the saturation charge $Q_{th}$ [86]. For many metals, charge relaxation time ranges from $10^{-15}$ s to $10^{-19}$ s ($\tau \ll 1\ s$), and hence the particle charging is instantaneous. For dust particles, exact quantification of $\tau$ is challenging. However, we arrive at a lower estimate for electrical conductivity and thus an upper estimate for charge relaxation time of dust particles by measuring the resistance of dust compressed between two metallic plates at moderate relative humidity (~45%-50%). The dust particles are constrained within a 3D printed ring of thickness ($t$) 1 mm and diameter ($D$) 10 cm. The resistance ($R$) is measured using a multimeter. Since $R = \frac{\rho t}{A} = \frac{t}{(\sigma A)} = \frac{4t}{\sigma \pi D^2}$, conductivity ($\sigma$) is calculated as $\sigma = \frac{4t}{(R\pi D^2)}$ and is plotted in Figure 2-10A. Here, since the area is assumed as the apparent contact area which is an upper estimate compared to the real contact area where dust particles are only making partial contact with each other depending on the packing, we underestimate the conductivity. Charge relaxation time is $\tau = \frac{\epsilon}{\sigma}$. Here, the permittivity of the medium is approximated to be that corresponding to water since we see from our humidity-controlled experiments that adsorbed moisture is the cause of conductivity. We plot the charge relaxation time $\tau$ for various particle sizes in Figure 2-10B. It can be seen that $\tau$ is <<1 s. This implies that even though dust particles are not as conductive as metallic particles in terms of conductivity, they reach the saturation charge nearly instantaneously and thus the charge on dust particles scale similar to that of metallic particles as shown in Figure 2-8F.

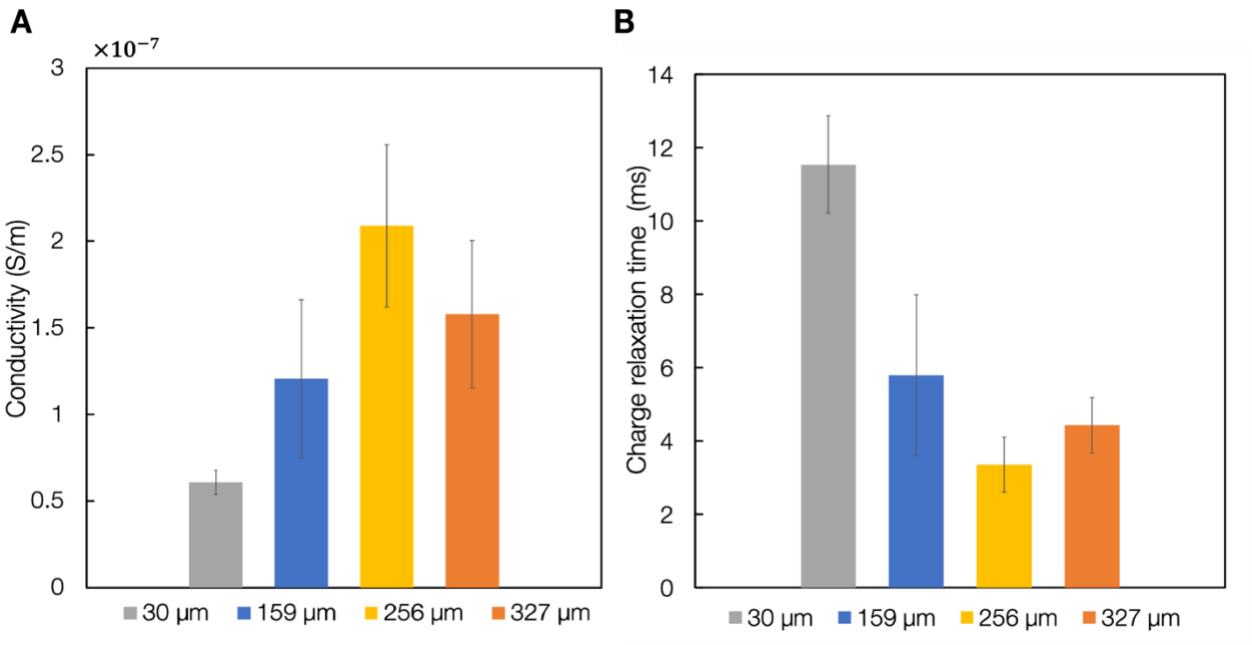


Figure 2-10. **Lower estimate for conductivity and upper estimate for charge relaxation time constant of dust particles. (A)** Lower limit for conductivity (σ) is estimated by using the nominal cross-sectional area (A) and thickness (t) of dust film as σ=t/(A*R) **(B)** An upper limit for charge relaxation time constant (τ) is estimated from the permittivity of adsorbed water (ε) and estimated conductivity values (σ). τ=ε/σ<< 1 s for all cases.

### 2.3.2. Defining the dust removal voltage

From the estimated charge and resulting expression for charge as a function of voltage, we write the full expression for force balance for a perfectly spherical particle considering electrostatic, gravitational and Van der Waals forces of adhesion. Here, for a given particle size, electrostatic force is limited by the maximum electric field strength that can be sustained in air (3 MV/m) without causing dielectric breakdown [86]. We assume this upper limit for $E$ and material properties of silica where Hamaker constant $A \sim 6.3 \times 10^{-20}\ J$ (in air), density $\rho \sim 2650\ \frac{kg}{m^3}$, and particle-surface atomic separation of $d_0 \sim 0.4\ nm$ [88,89]. We write an expression for the sum of the forces (Equation 2.12) and plot it as a function of particle size to obtain the bell-like curve as shown in Figure 2-11A. Because Van der Waals force scales with particle size, electrostatic force scales with surface area, and gravitational force scales with particle volume, the resulting balance shows that as particle size becomes larger, $F_{net}<0$ due to dominance of gravity. Similarly, as

particle size becomes small (expanded inset of Figure 2-11A) $F_{net}$ again becomes <0 due to the dominance of adhesion. However, at intermediate particle sizes, this analysis confirms that electrostatic force is indeed sufficient for the experimentally observed removal of particles from charged surfaces.

$$F_{net} = F_E - F_A - F_G = (4\pi\epsilon_0\epsilon_r E^2)R^2 - \left(\frac{A}{6d_0^2}\right)R - \left(\rho\frac{4}{3}\pi g\right)R^3 \qquad 2.12$$

To experimentally determine the particle removal condition, we designed the setup shown in Figure 2-11B where dust particles rest on the bottom plate (made of silicon wafer) of the parallel plate setup placed on a weighing scale having 1 mg precision. The top plate is independently held in position such that its weight is not transmitted through the scale (see Experimental Methods). We applied voltage between the plates and measured the reading on the scale as a function of voltage. We define the fraction of dust removed ($M^* = \frac{M - M_{\min}}{M_{\max} - M_{\min}}$) by non-dimensionalizing the scale reading ($M$) using initial ($M_{\max}$) and final readings ($M_{\min}$). By plotting $M^*$ against the applied voltage, we obtain the curve shown in Figure 2-11C. It can be seen that for different particle sizes, there exists a unique threshold voltage at which most of the particles are removed. We define this threshold voltage as the dust-removal voltage.

Using the expression for force balance, we derive an expression for dust removal voltage as shown in Equation 2.13, where $gcos(\theta)$ is the normal component of gravity due to the tilt ($\theta \sim 20^0$) of the plate we introduced, and $s$ is the separation/gap between the plates (~1.2 cm) (see Experimental Methods).

$$F_E = F_A + F_G$$

$$(4\pi\epsilon_0\epsilon_r E_{th}^2)R^2 = C_r\left(\frac{A}{6d_0^2}\right)R + \left(\rho\frac{4}{3}\pi g cos(\theta)\right)R^3$$

$$E_{th} = \frac{V_{th}}{s}$$

$$V_{th} = \sqrt{\left(\frac{C_r A s^2}{24\pi\epsilon_0\epsilon_r d_0^2}\right)\frac{1}{R} + \left(\frac{\rho g cos(\theta) s^2}{3\epsilon_0\epsilon_r}\right)R} \qquad 2.13$$

Notice that we also introduce a roughness correction factor $C_r$ in front of the Van der Waals force term as proposed by Rabinovich et al.[85], which is also known as the modified Rumpf model. The theoretical model for force of adhesion proposed by Hamaker [84] is a simplified one and does not consider surface irregularities. Even for smooth-looking glass micro-spheres, it has been shown that the scale of RMS surface roughness could be of the order of few nano-meters [90]. Hamaker's equation for Van der Waals force was modified by Rumpf [91] by assuming hemispherical asperities on the surface, which was later modified by Rabinovic et al. [85] by considering RMS surface roughness on the substrate. This modification introduces the pre-factor to the Hamaker's equation as shown below (Equation 2.14).

$$F_{adh} = \left[\frac{1}{\left(1+\frac{R}{1.48r_{RMS}}\right)} + \frac{1}{\left(1+\frac{1.48r_{RMS}}{d_0}\right)^2}\right]\frac{AR}{6d_0^2} = C_r\frac{AR}{6d_0^2} \qquad 2.14$$

Here $r_{RMS}$ is the RMS surface roughness. We call the pre-factor as $C_r$ or the roughness correction factor. It should be noted that even for large particles of size hundreds of microns, the RMS surface roughness will be nanometric. Thus, $C_r$ becomes small (<1); meaning that Van der Waals force of adhesion reduces for microparticles with nano-scale roughness compared to a perfectly smooth microparticle. As can be seen in Figure 2-12A, even though the average particle size is about 75 microns, the minimum feature (sharp points) size on the surface is much smaller in size. We measure the average surface roughness of these dust particles using AFM and find that the RMS roughness is nanometric (~25 $\pm$ 5 nm) as shown in Figure 2-12B.

This factor accounts for the rough surface topology of the dust particles, which is shown in the AFM image of Figure 2-11D and has a measured RMS roughness of ~25 nm. Nano-scale roughness reduces the force of adhesion significantly [92], and must therefore be considered in this force balance. We estimate $C_r$ by measuring the value of surface roughness using AFM ($r_{RMS}$~25 $nm$) and plugging in the value for particle radius $R$ and parameter $d_0$ in Equation 2.14. The observed value of surface roughness and the estimated values of $C_r$ we use in our force balance model are in alignment with those estimated by the modified Rumpf model. The exact value of $C_r$ is dependent on the size of particle ($R$) as described in Equation 2.14. Since our particle sizes vary by a factor a ~40 (from ~7.5 $\mu m$ to ~327 $\mu m$), the estimated $C_r$ values also vary significantly (by

a factor of ~30) from largest particle size to the smallest. The effect of adhesion force is predominant in small particles and large particles are mostly influenced by only gravitational force. Therefore, $C_r$ is more relevant for smaller particles (<30 $\mu m$). For particle size on the order of 10 microns, the estimated value of $C_r$ is $\sim 10^{-2}$, meaning the force of adhesion compared to that of a smooth surface could be reduced by up to two orders of magnitude, as suggested by models and experiments in literature[91,93,94]. We non-dimensionalize the horizontal axis of Figure 2-11C by normalizing the measured voltage with $V_{th}$ and plot it in Figure 2-11E ($V^*=V/V_{th}$). We see that all curves collapse onto a single non-dimensional curve suggesting that our simple model captures the essential physics of the induction-based dust removal process. Thus, $V^*>1$ defines the non-dimensional criterion for dust removal.

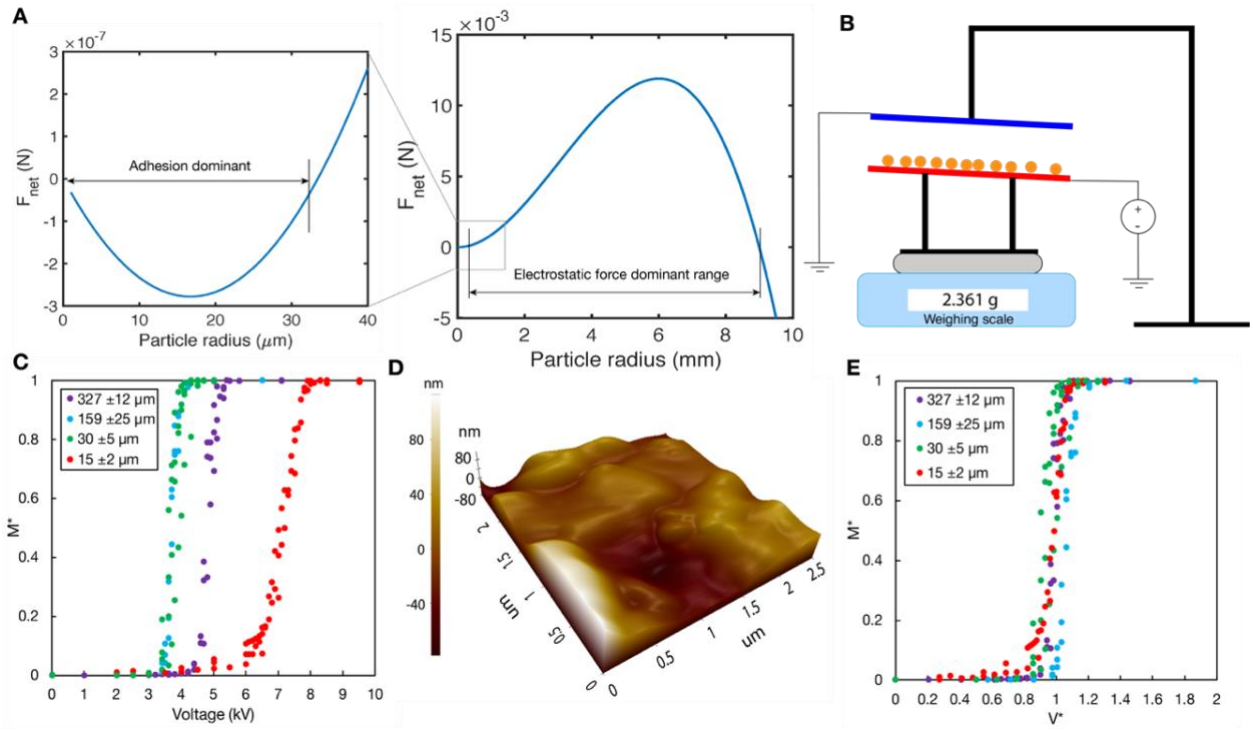


Figure 2-11. **Forces acting on dust particles and the dust removal voltage.** (**A**) The net vertical force acting on a dust particle in contact with an electrode as a function of particle size. We assume material properties of silica. $F_{net} > 0$ when electrostatic force dominates adhesion and gravity. In the expanded portion for small particle sizes, it can be seen that $F_{net} < 0$ due to domination of adhesion. (**B**) Schematic of the experimental setup to determine the threshold voltage for dust removal. Dust removal is quantified by measuring the reduction of mass in the digital weighing scale reading. (**C**) Threshold voltage for removing dust particles is plotted for different particle sizes. The sudden jump in the fraction of dust removed ($M^*$) denotes the dust removal voltage. (**D**)

AFM surface roughness of a typical dust microparticle. RMS roughness was found to be nanometric (~25 nm). (**E**) Dust removal voltage curves for different particle sizes collapsing onto a single non-dimensional curve with threshold voltage for dust removal at $V^*$~1.

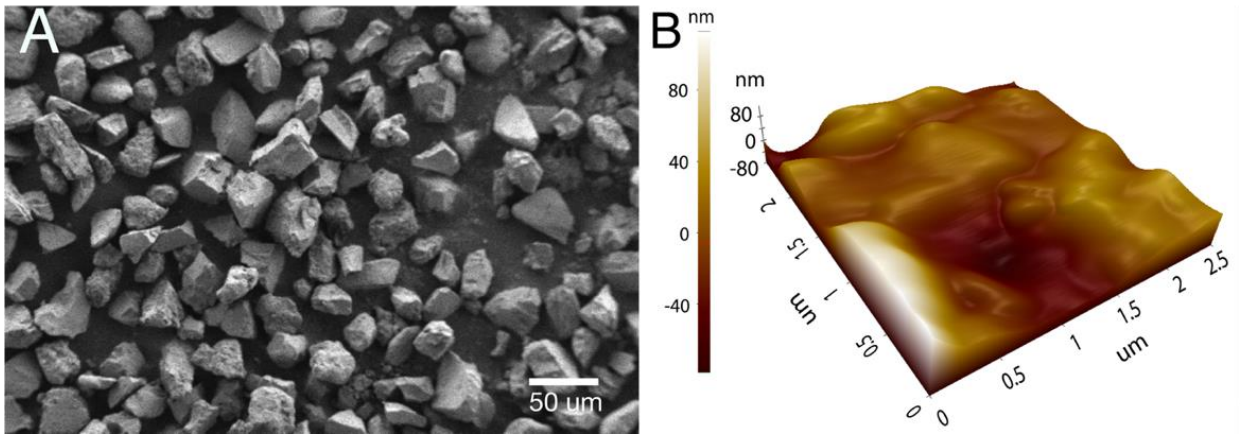


Figure 2-12. **Roughness:** (**A**) SEM image of 75 μm dust particles. (**B**) AFM surface topology.

## 2.3.3. Effect of humidity

Moisture adsorption on dust particles changes with the relative humidity of the ambient environment, which fluctuates in outdoor conditions depending on the time of the day and the season. Because charging depends on moisture adsorption [80], we expect that dust removal will also depend on humidity. To study the effect of changing humidity we devised an experimental setup (Figure 2-13A) where electrodes were placed inside a sealed acrylic chamber with two inlets- one for nitrogen purging to decrease the humidity and another for flow of humid air to increase the humidity. A wireless humidity sensor placed inside the chamber measured the real-time humidity.

The bottom electrode was made of smooth rectangular silicon cut from silicon wafer to minimize the effect of surface irregularities on adhesion. On application of voltage (10 kV), dust particles were removed, which was quantified using optical microscope imaging of the remaining dust on silicon wafer (Figure 2-13B). Figure 2-13C shows a microscope image from one of the experiments with remaining dust particles (~30 um) appearing as white dots on the silicon wafer, which appears black. We use the percentage area of the wafer covered by particles as a measure of dust removal.

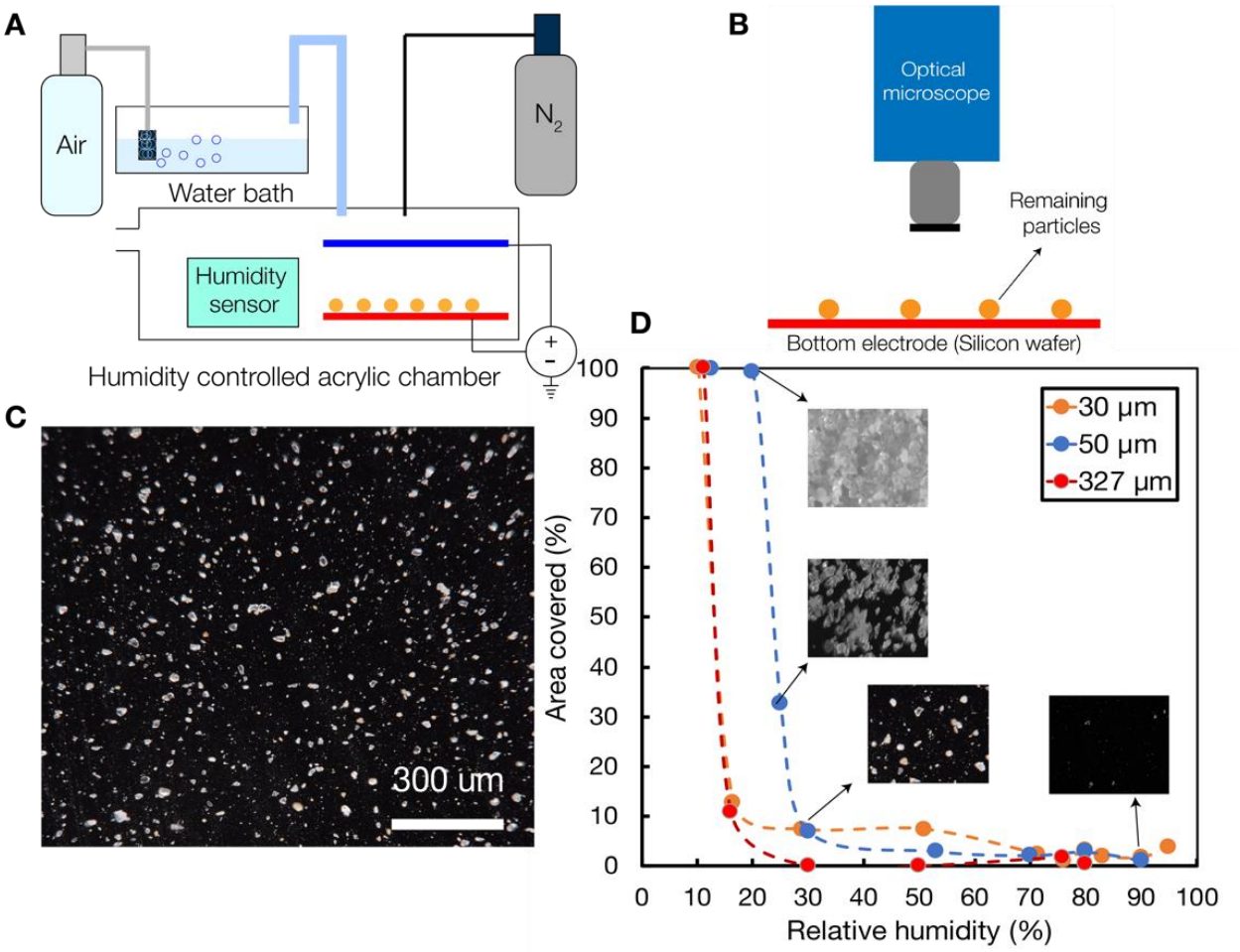


Figure 2-13. **Dust removal with varying humidity.** (**A**) Schematic of the humidity chamber experimental setup with nitrogen purge for reducing humidity and compressed air bubbler for increasing humidity. There were two ports for connecting the electrical leads and one port for gas exit. (**B**) Schematic of optical microscope imaging of dust particles that remained on the bottom electrode after applying voltage. (**C**) Microscope picture of remaining particles (size ~30 um) after applying 10 kV across the parallel plates spaced by 1.5 cm. (**D**) Percentage area of the surface covered by particles for different particle sizes across varying humidity. Even though dust particles do not get removed at low humidity, electrostatic repulsion works for a wide range of relative humidity values.

Relative humidity was varied between ~10% and ~95% (see Experimental Methods) for dust particles of different sizes, as shown in Figure 2-13D. At low relative humidity values (<~30%), dust particles remained stuck to the silicon surface due to a lack of moisture-assisted charging. However, for relative humidity values above 30% and even as high as 95% dust removal was

highly effective. Desert regions typically experience daily fluctuation in humidity where during the daytime relative humidity tends to be low (below 30%) and during night the humidity rises followed by the cooling of atmosphere and sometimes even results in humidity saturation as shown in Figure 2-14 [12,95]. Therefore, our electrostatic dust removal technique can be deployed and used as part of a daily cleaning when the humidity rises. For other geographic regions where there is moderate (~50%) or high (>75%) relative humidity, our approach works well to remove most of the dust particles as we demonstrate in Figure 2-13D. This makes our induction-based approach robust and widely applicable for various geographical locations.

We further confirm the humidity-based charge induction by performing experiments using silica beads. We find that pristine silica beads get charged and completely repelled off from electrodes on application of voltage (Figure 2-15B, Movie 2-6). The hydrophilic nature of silica makes it possible for the particles to absorb sufficient moisture to experience sufficient charging. However, silica particles coated with OTS (Trichloro(octadecyl)silane), a molecule with hydrophobic end group, are made hydrophobic and cannot absorb sufficient moisture even at 55% relative humidity. Therefore, OTS coated silica beads are not completely repelled off from the electrodes (Figure 2-15A, Movie 2-7). These observations indicate that charging is governed by the hydrophilic nature of particles that result in sufficient moisture absorption, which results in charge induction.

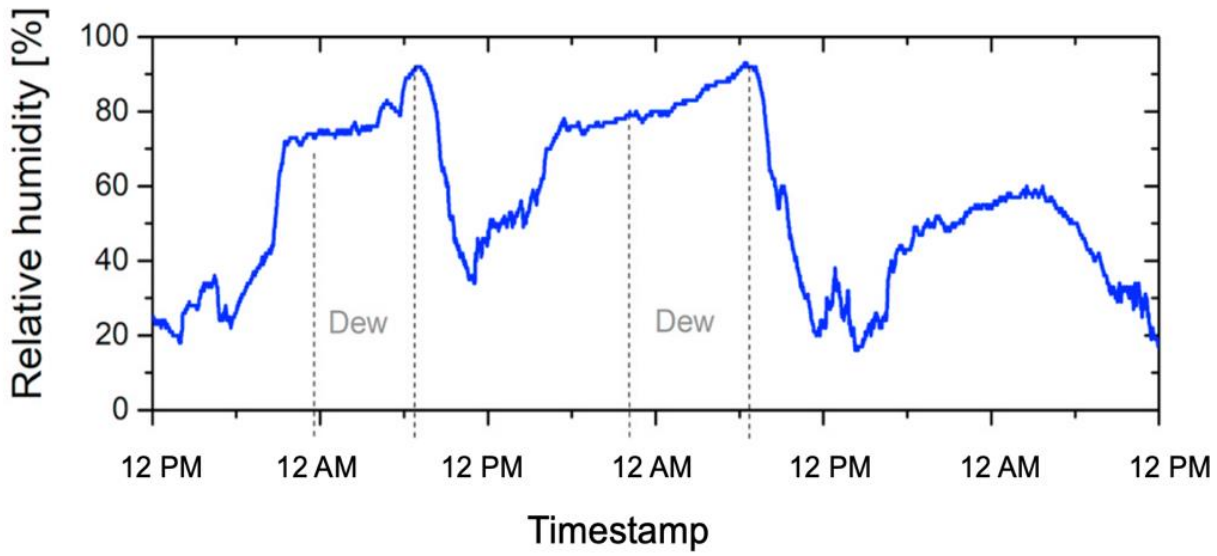


Figure 2-14. **Typical humidity fluctuation at solar test facility Doha** [12]

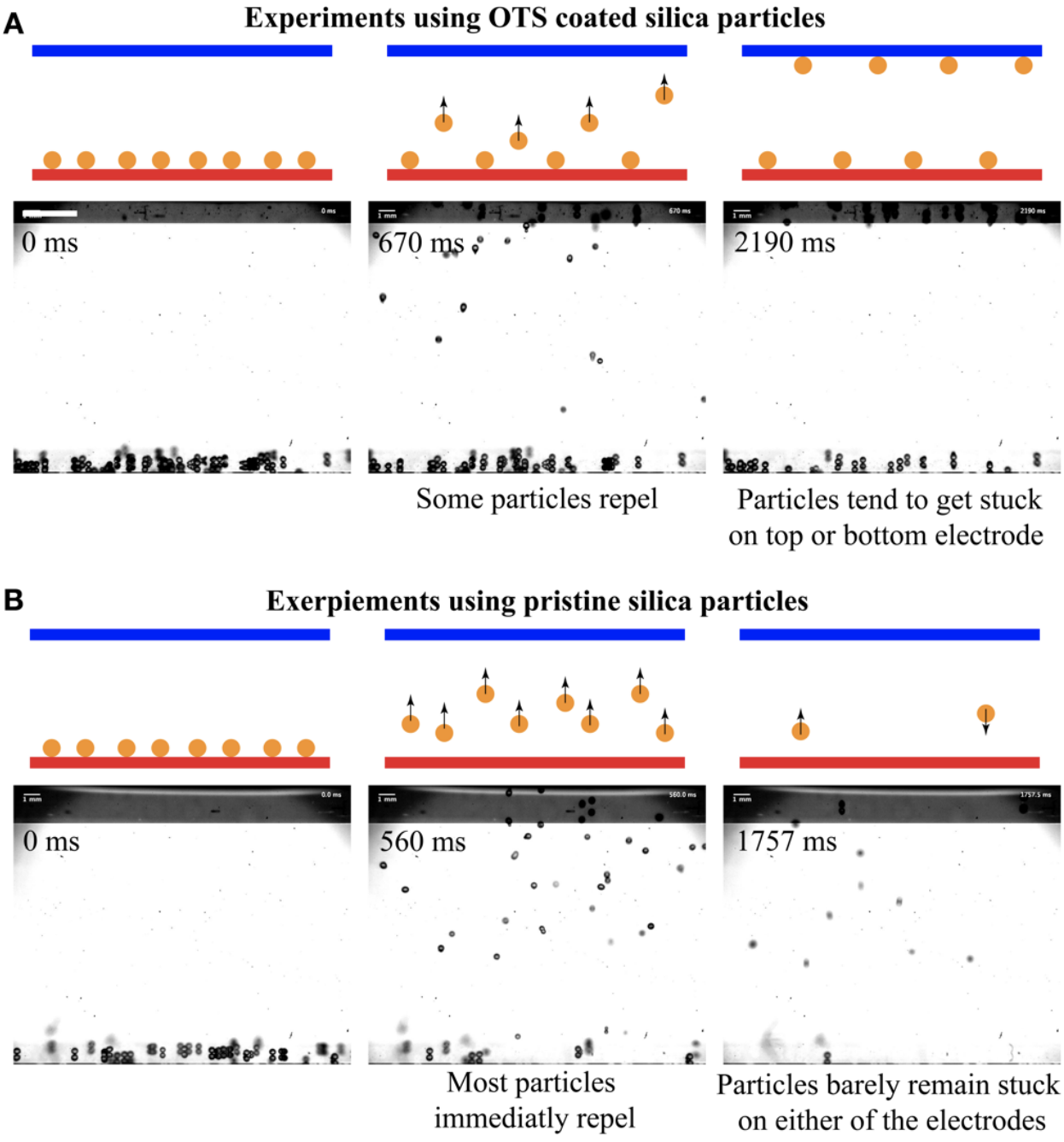


Figure 2-15. **Particle repulsion experiments using OTS coated silica particles and pristine silica particles:** (A) Experiments using OTS coated silica particles. Schematic depicts the experimental observation. Silica particles coated with Trichloro(octadecyl)silane (OTS) finds it difficult to acquire charge due to decreased extent of moisture absorption caused by hydrophobic chemistry. On application of voltage some particles acquire weak charge and get repelled, but they get stuck at the top electrode. Ultimately, particles are not fully removed from the plates. (B) Experiments using pristine, uncoated silica beads. The surface of the particles has hydrophilic chemistry, which helps moisture absorption. As soon as the voltage is turned on almost all particles

are repelled off from the bottom plate. The particles colliding with the top plate do not get stuck there, Eventually, almost all particles are removed from the space between the electrodes. Mean diameter of particles are ~327 μm Applied voltage is 13 kV. Scalebar is 1.5 mm.

### 2.3.4. Lab-scale prototype

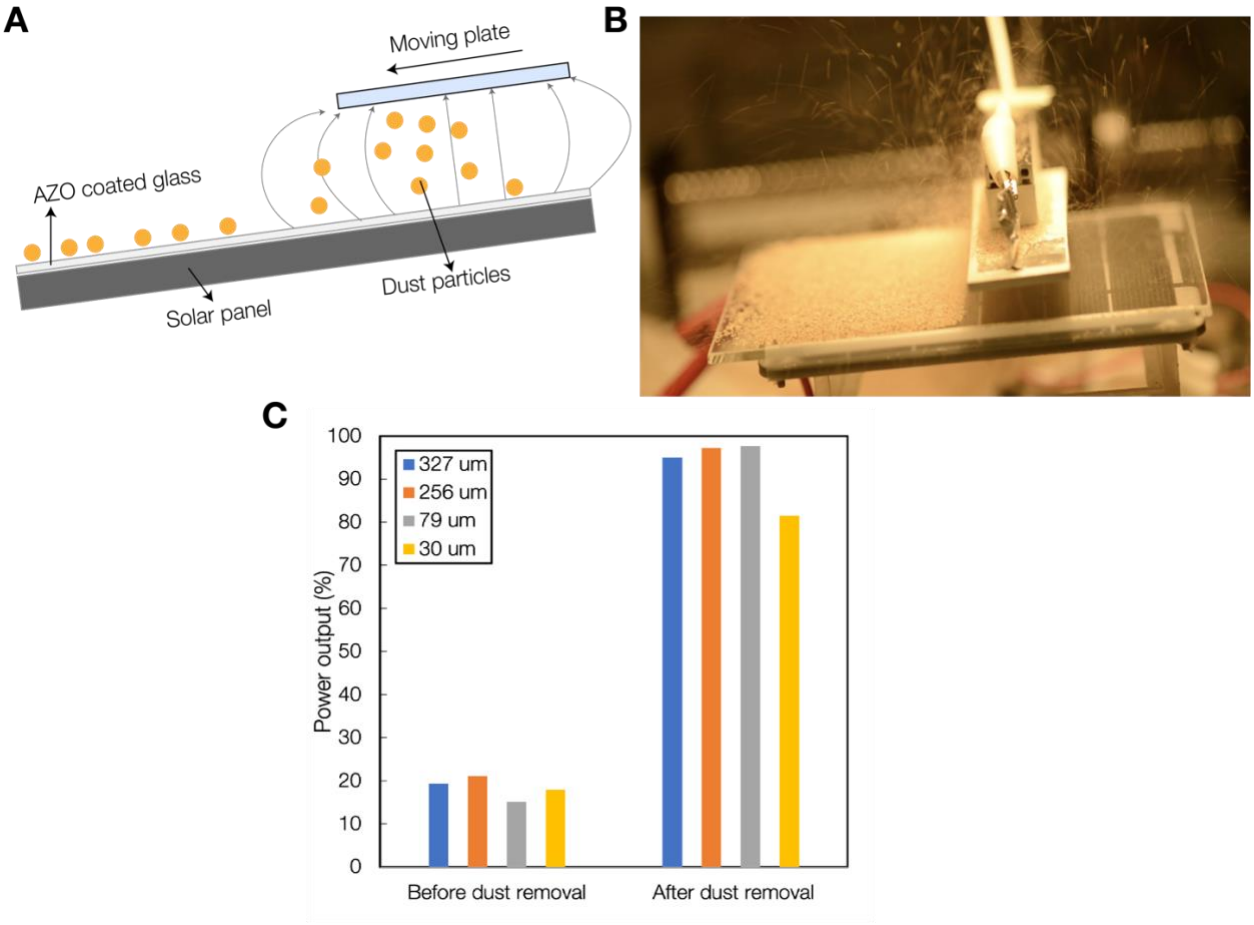


Figure 2-16. **Electrostatic cleaning system installed on a lab-scale solar panel.** (**A**) Schematic of the dust removal mechanism with AZO coated glass installed on top a 10 cmx15 cm solar panel. Electric field is set up between moving top plate and the bottom transparent electrode. (**B**) Lab-scale electrostatic solar panel cleaner with moving plate controlled by stepper motor-linear guide mechanism under operation. (**C**) Power recovery from solar panel after dust removal for different dust particle sizes.

Finally, we designed and fabricated an electrostatic dust removal system for a lab scale solar panel. The glass plate on top of the solar panel was coated with a 5 nm thick transparent and conductive layer of Aluminum doped Zinc Oxide (AZO) using Atomic Layer Deposition (ALD)

(see Experimental Methods) and forms the bottom electrode (Figure 2-16A). The top electrode (made of aluminum) is mobile to avoid shading the solar panel and is translated along the panel during cleaning using a linear guide-stepper motor mechanism (Figure 2-16B) When a voltage ~12 kV is applied across the electrodes (calculated from our model to satisfy V*>1), dust particles are removed from the solar panel surface as the top electrode passes by the surface (Movie 2-5). The output power was measured before and after cleaning for different dust particle sizes (Figure 2-16C), and we measure a 95% recovery in the lost power after cleaning for particle sizes greater than ~30 microns.

For real solar farms, dust particle size distribution is dependent on the geographic location. It has been shown that the size distribution varies from 0.8-1000 microns and for many locations, the mean dust particle size is above ~30 microns, making our approach highly practical [96]. There are also several locations where the mean particle size falls below ~30 microns. However, it must be noted that the total optical loss by soiling is due to a combination of absorption, reflection and scattering of light by dust particles. Unless the particle size is on the order of wavelength of light (sub-micron), absorption and reflection (shadowing) losses are predominant, which increases proportional to the surface area of the particle [97]. Our approach can effectively remove the larger particles (>30 microns) in a particle size distribution with mean size <30 microns that can potentially contribute to more severe soiling loss and provide significant improvement to the efficiency and reduction in the water usage.

For manufacturing transparent conductive surfaces, ALD technique is an already established industrial standard in photovoltaics for smaller substrates. Also, there is quite a lot of interest to use transparent conductive oxides such as ITO for developing thin film solar cells [98]. Since we provide a uniform coating, there are no complex microfabrication steps involved (unlike embedded microelectrodes in prior works), which eliminates significant portion of the cost making our embodiment much practical to scale up. All we need to provide is a simple retrofit of a thin transparent film with an appropriate conductive coating on top of the solar panel. For high throughput, techniques such as roll-to-roll deposition can be used [99]. Since we are not limited by the resistance of the thin film due to zero current flow between the electrodes, we can make the coating as thin as possible. The thickness of our current coating is ~5 nm. However, it could be as

small as 1 nm or even sub-nanometric, which will significantly reduce the cost and minimize any potential optical losses.

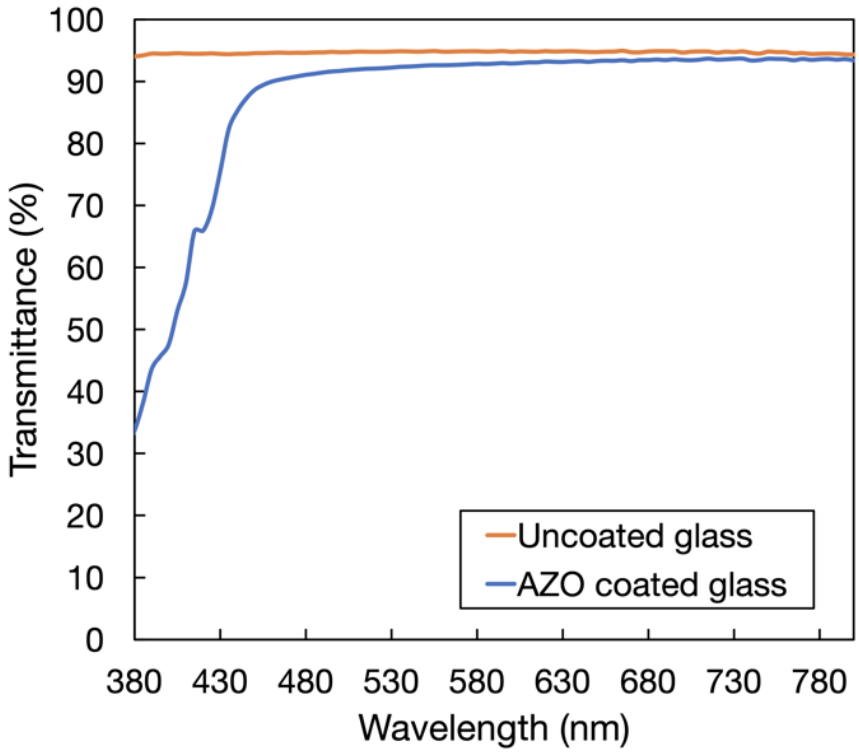


Figure 2-17. **Light transmittance of pristine uncoated glass and AZO coated glass in the visible spectrum:** Light transmittance of AZO coated glass and uncoated glass of same thickness (~2.5 mm) in the visible spectrum measured using UV-vis spectrometer. For most of the wavelength in visible spectrum from ~450-750 nm, both uncoated and AZO coated glasses have high transmittance of ~90%. Due to UV absorption, AZO coated glass displays lower transmittance at smaller wavelengths.

For our dust removal technology, the power consumption associated with electrostatic dust repulsion is virtually negligible. This is because, even though the applied voltage is on the order of kilovolts, there is no current flow between the top and bottom electrodes and therefore no electrical power consumption. The only mode of power consumption is that associated with the translation of the moving electrode. For powering the translation, a separate dedicated solar panel and battery unit can be used such that our retrofit dust removal mechanism withdraws no power from the solar panel array. We can utilize a single moving electrode for an array of solar panels consisting of about 20 solar panels by making it translate in both directions along the plane of the

solar panel array using retrofit railings or other mechanical components as shown in Figure 2-18. Finally, we also developed a framework for fully autonomous solar panel cleaning system that incorporates machine learning techniques for detection and classification of dust particle distribution on a solar panel for providing feedback to the robotic dust removal mechanism (see Appendix).

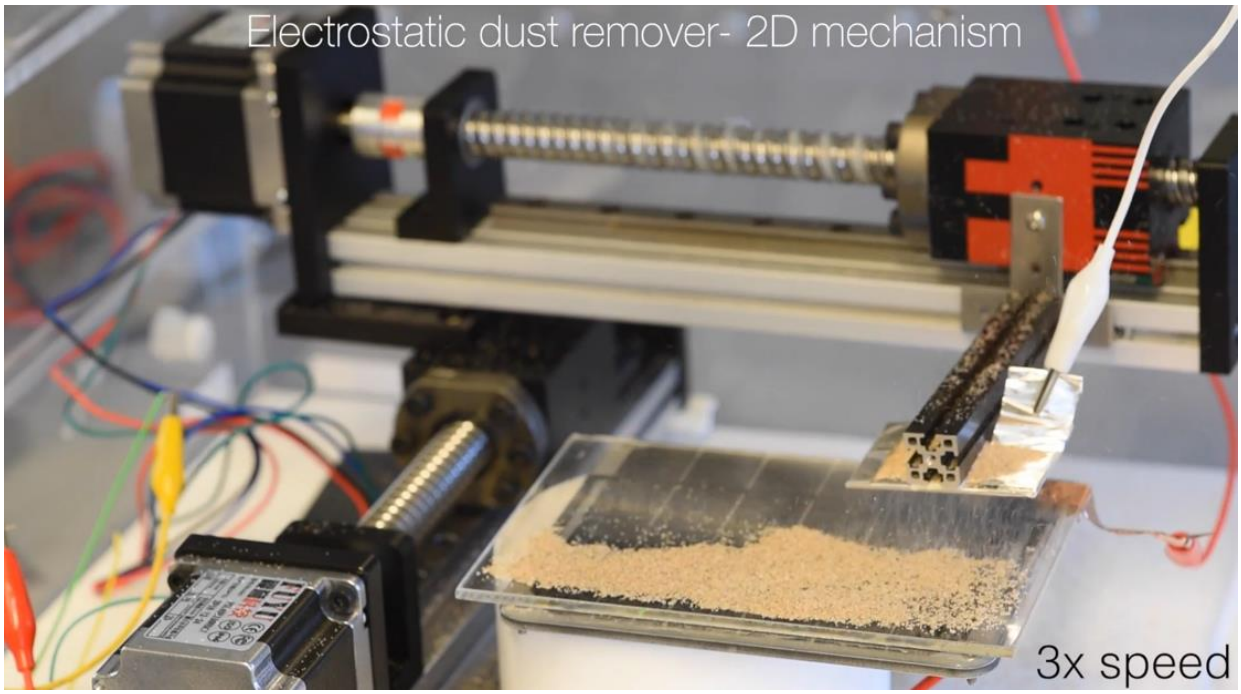


Figure 2-18. **2D solar panel cleaning mechanism**. The moving electrode can be made to translate along and across solar panels.

## 2.4. Experimental Methods

### 2.4.1. Equipment and materials

- DC High voltage power source: Spellman; model no.- SL30P600.
- Mini solar panel: Adafruit; model- Medium 6V 2W.
- Stepper motor with linear guide: FUYU FSL40 Linear Guide Slide Stage Actuator Motorized by Nema 23 Stepper Motor.
- Stepper motor control: Adafruit Metro M0 express with DRV8833 driver.
- Optical microscope: Zeiss; model- Axio zoom.

- Multimeter: EXTECH; model- EX540.
- Dust and iron particles: Arizona Test Dust particles and iron particles of various mean sizes were obtained from Powder Technology Incorporated (PTI). Dust particles have average density of 2.6 g/cc and consist of up to 77% silica [100]. Particle diameters (mean±std) of different size distributions we use are: 15±2 µm, 30±5 µm, 50±5 µm, 79±20 µm, 159±25 µm, 256±20 µm, 327±12 µm.
- Stainless steel microspheres 7.8g/cc density of various sizes were purchased from Cospheric LLC.
- Silicone oil (500cSt) purchased from Sigma Aldrich.
- Weighing scale for dust removal voltage measurement experiments: Hogentogler & Co. Inc.
- Wireless humidity sensor: Sensorpush.

### 2.4.2. Charge estimation experiments using silicone oil bath

The bouncing of dust particles between parallel plates occurs at uniform velocity when the electrodes are immersed in high viscosity silicone oil (500cSt). Too low of a viscosity of the medium (air or low viscosity silicone oil) does not allow the particles to reach terminal velocity within the time duration it takes for dust particles to travel from one plate to another. Theoretically, it should still be possible to estimate the charge on particles by balancing electrostatic, gravitational, inertial, and viscous forces. Inertial forces could be estimated by experimentally determining the acceleration using high-speed imaging. However, since dust particles are not perfectly spherical, particles rebound between the plates at random velocity depending on the orientation of impact (Movie 2-2). This makes it difficult to extract useful information from the high-speed images of dust particle oscillation in low viscosity medium. Too high viscosity (>1000 cSt) is also not favorable because the thin oil film between particle and the electrode surface takes long time to get displaced for dust to physically contact the electrode for getting charged. Thus, appropriate viscosity of silicone oil was selected such that inertia is negligible but displacing the oil film does not take long time.

### 2.4.3. Experiments for determining dust removal voltage

The dust removal voltage was estimated by measuring the reading of the weighing scale against the applied voltage. Dust particles took off from the bottom plate placed on a 3d-printed fixture on the weighing scale as applied voltage was increased. At a certain threshold voltage most of the dust particles were removed. This shows up as a sudden jump in the $M^*$ vs $V$ curve as shown in Figure 2-11C. Since a fraction of electric field lines starting from the bottom plate end up on the top portion of the top plate, few particles land on top of the top plate after taking off from the bottom plate (Movie 2-1). Therefore, to avoid measuring the weight of these particles, the top plate was held separately in place without letting its weight fall on the weighing scale. Also, the parallel plates were tilted a bit to preferentially let most of the dust particles to fall onto one side assisted by gravity. We use the tilt angle ($\theta$ ~20 degrees) to get effective normal component of gravity ($gcos(\theta)$) in equation 4. The scale readings were taken only after switching off the high voltage, otherwise the electric field from the top plate pulls the bottom plate up, reducing the scale reading. Since this experiment is really weight sensitive because the total weight of dust being removed from the plate is only ~1 g, the electrical wire that connects to the bottom plate was taped firm in its position to make it not move and perturb the measurement.

### 2.4.4. Experiments with varying humidity

Humidity was controlled in a sealed acrylic chamber by controlling the flow of nitrogen or compressed humid air. Nitrogen purging was very effective for achieving relative humidity as low as 10%. For increasing the humidity, a typical humidifier that creates mist was initially tried and was found to be not effective. This is because the droplets from the mist get deposited on the dust particles and thus particles remain stuck on the silicon surface along with the water drops even after applying voltage, owing to the hydrophilic nature of the surface. Hence, we bubbled compressed air through a porous stone (aeration stone) into a water bath that resulted in humid air without entraining any water drops. This air was passed into the acrylic chamber to increase the humidity. Increasing the flow rate of air through the bubbling stone, in general, increases the relative humidity. However, there is a threshold flow rate (estimated by trial and error) of compressed air beyond which increasing the flow rate decreases the relative humidity owing to a smaller fraction of water vapor compared to air. By this method, we were able to push the humidity

of the chamber up to ~80%. The flow rates of nitrogen or compressed humid air were controlled manually to attain different humidity values ranging from 10% to 80%. To achieve higher humidity values (from 80%-95%), we used a wet sponge that was placed inside the fully sealed acrylic chamber and waited for evaporation to take place. It took up to 14 hours for the chamber to become 95% humid.

### 2.4.5. Atomic Layer Deposition (ALD) for fabricating transparent electrode

ALD deposition of Aluminum doped Zinc Oxide on glass substrate was performed by coating ZnO and Aluminum layer by layer at Center for Nanoscale Systems (CNS), Harvard University. The layer thickness of ZnO and Al is in the ratio of 40:1 such that the composite AZO coating has 2.5% doping of Al in ZnO. We measure the transmittance of AZO coated glass using UV-vis spectrometer. The transmittance (~90%) is very close to that of a pristine uncoated glass (~92%) surface for most of the wavelengths of the visible spectrum (Figure 2-17).

### 2.4.6. Translation mechanism for moving top electrode

The top electrode is made of rectangular Aluminum and is electrically grounded. The electrode is fixed on the moving stage of a linear guide actuator that makes the plate translate along the top surface of the solar panel. Lead screw rotation is controlled by a NEMA 23 stepper motor. To control the stepper motor, we make use of an “Adafruit Metro M0 Express” microcontroller coupled with a DRV8833 stepper motor driver. The microcontroller and driver need not be powered separately, as the power for the driver is taken from the micro-controller. In order to have precise input voltage and current control, we can power the microcontroller using a DC voltage source. Alternately, the microcontroller can be simply powered using a 9 V battery. Depending on the counter torque that is acting on the stepper motor we will need to increase the input voltage as we find from operating the dust removal mechanism. In such cases, we make use of DC power supply at a fixed current but variable voltage setting.

## 2.5. Conclusion

In summary, we demonstrate a simple electrostatic induction-based approach for mitigating the dust-accumulation problem on solar panels to recover the lost power output. We find that dust particles, even though predominantly consisting of insulating silica material, can be made to repel from surfaces using moisture-assisted charge induction. We experimentally estimate this charge

and show that the dust particles are electrically conducting. We characterize the dust removal process for different particle sizes and derive an expression for the voltage required for particle removal. Furthermore, we show that our approach can recover 95% of the lost power and is effective whenever the relative humidity of the ambient environment is greater than ~30%. We discuss how we can leverage ambient humidity fluctuation to make our approach widely applicable to solar installations around the world. Given the significant efficiency losses posed by dust fouling and the associated water footprint for cleaning the panels, we expect that our waterless electrostatic cleaning can provide an efficient and cost-effective approach for maintaining dust-free solar panels, contributing to sustainable operation of solar farms.

THIS PAGE INTENTIONALLY LEFT BLANK

# 3. Enhanced electrostatic dust removal from solar panels using transparent, electrically conductive, nanotextured surface

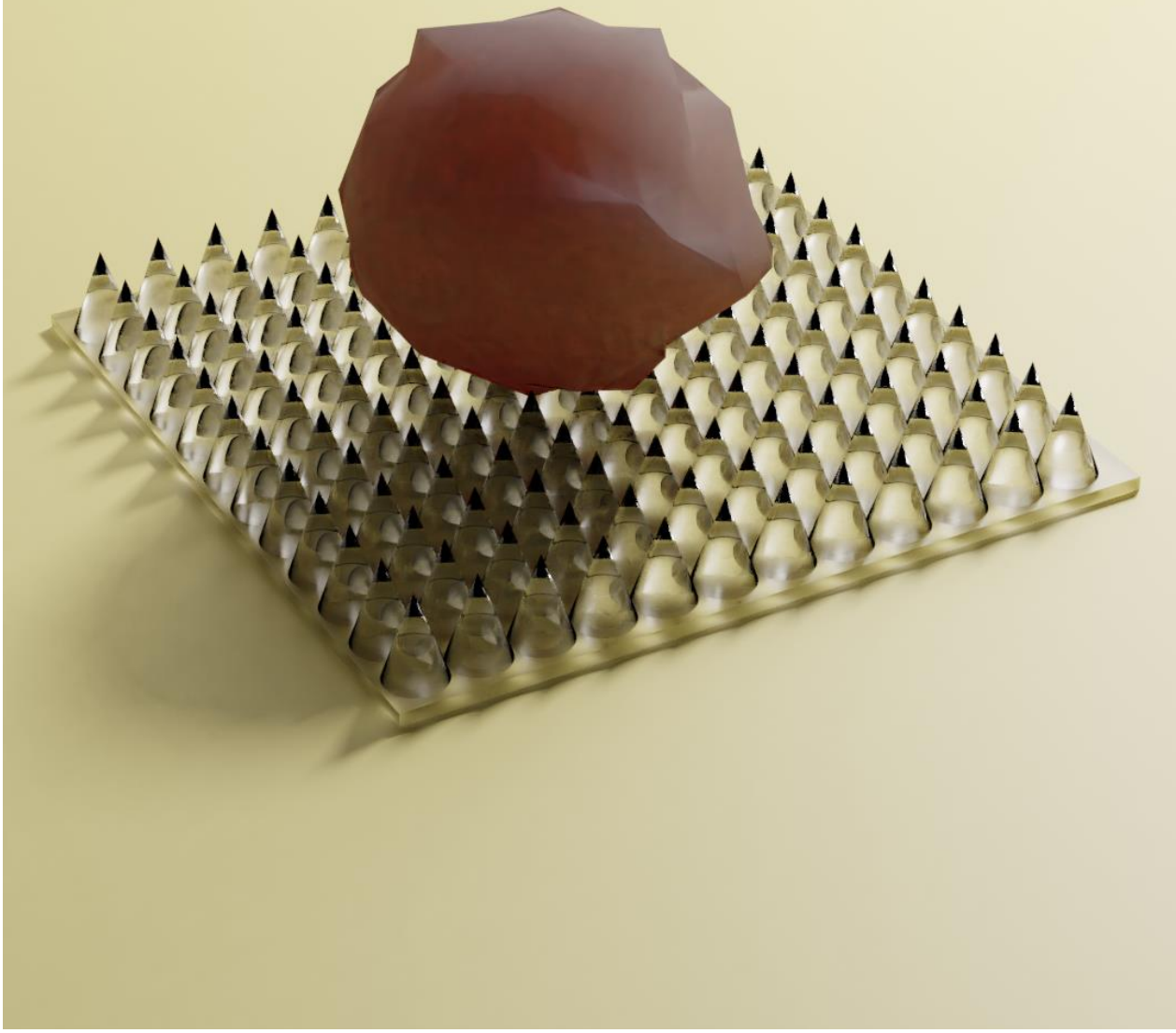

## 3.1. Abstract

As we discuss in Chapter 2 of this thesis, dust accumulation on solar panels is one of the biggest operational challenges faced by the photovoltaic industry. Removing dust using water-based cleaning is expensive and unsustainable. Dust repulsion via charge induction is one of the most promising ways to clean solar panels and recover power output without consuming a single drop of water. However, it is still challenging to remove small particles (<30 $\mu m$) because Van der Waals force of adhesion overcomes electrostatic force of repulsion. In this chapter, we propose nanotextured glass surfaces for significantly enhancing electrostatic dust removal in the small particle size regime. We performed AFM pull-off force experiments and demonstrate that nano-textured surfaces reduce the force of adhesion by up to 2 orders of magnitude. We show that the reduced adhesion results in significantly better (~3.5-fold) small particle electrostatic dust removal compared to plain or micro-textured surfaces. We fabricate transparent, electrically conductive, nanotextured glass that can be retrofit on solar panel surfaces and show that we can recover more than 90% of lost power output in the small particle regime.

## 3.2. Introduction

Most of the big solar power plants (>500 MW) in the world are located in dry geographic regions such as deserts due to availability of sunlight and land area. However, there is significant wind and airborne dust in these regions that accumulates on top of the panels over time, blocking the incident sunlight [8–10,64,101,102]. Solar panels are therefore cleaned regularly to maintain the power output [12,13,101,103]. Water based cleaning, which is the most widely used cleaning method is quite expensive, contributing up to 10% of annual operation and maintenance cost [15,101]. It is also unsustainable in the long run due to the huge freshwater footprint (>10 billion gallons per year) [17]. Waterless brush scrubbing based cleaning introduces irreversible scratching damage that affects the long-term operation of solar panels [66]. Alternate effective cleaning methods can therefore significantly transform the photovoltaic solar power industry.

Electrostatic dust removal has the potential to eliminate the water footprint and contact scrubbing damage associated with solar panel cleaning. There are mainly two types of techniques or embodiments for electrostatic dust removal systems. In the first type, Electrodynamic Screens (EDS) [67,68,72,104] or thin copper meshes [69,70] are used where a gradient of electric field is applied to

cause dielectrophoretic motion of dust particles. The dust particles are not charged but are merely carried along the direction of electric field gradient due to charge polarization [73,87]. Since dielectrophoretic force is a weak, short-range force, it is challenging to remove dust particles smaller than 100 $\mu m$. Therefore, a second type of technique- active coulombic charge induction based dust removal system, has been proposed for significantly more effective electrostatic dust removal [17] compared to Electrodynamic Screens.

In the active dust removal system, the glass surface of the solar panel is converted into a transparent, electrically conductive material. This enables the application of a potential difference between the glass electrode and another top moving electrode causing charge induction and repulsion of dust particles [17]. Coulombic force scales with the square of particle size ($\sim R^2$) since the charge carriers rearrange themselves on the surface of the dust particles rather than inside their bulk volume [86] (see Equation 3.1). This makes coulombic force much stronger compared to dielectrophoretic force for small particles that scales with the particle volume ($\sim R^3$) [105] (see Equation 3.2). However, even in active charging system, as the particle size approaches about ~30 microns, it is challenging to remove them electrostatically [17].

$$F_c = 4\pi R^2 \epsilon_0 \epsilon_r E^2 \sim R^2 \tag{3.1}$$

$$F_{DEP} = 2\pi R^3 \epsilon_L Re\left(\frac{\epsilon_p{}^* - \epsilon_L{}^*}{\epsilon_p{}^* + 2\epsilon_L{}^*}\right)\nabla E^2 \sim R^3 \tag{3.2}$$

For small particles, since gravitational force is negligible, electrostatic force of repulsion is counteracted by force of adhesion. The primary mechanisms for particle adhesion to a solid surface are Van der Waals attraction, capillary condensation of water vapor at the particle/surface interface, and electrostatic forces due to charged particles and surfaces due to tribo-charging [106]. In studies without either capillary condensation or significant tribo-charging, the only mechanism for particle adhesion is Van der Waals attraction force which scales with the particle size ($F_{vdw} \sim \frac{AR}{6d_0^2} \sim R$) [82,84,107]. Thus, for small particles Van der Waals force dominates electrostatic force of repulsion and makes it challenging to remove them from the electrode surface. Electrostatic force for a certain particle size also has an upper limit due to the breakdown field strength of air ($E_{max} \sim 3\ MV/m$) [86]. Therefore, there is a critical particle size below which electrostatic dust removal is challenging. Figure 3-1A shows the removal of large particles

(~327 $\mu m$) almost completely from the surface of a silicon wafer electrode after applying voltage. Here the applied voltage is ~15 kV between the parallel-plate electrodes spaced apart by ~3 cm. In the microscope image in Figure 3-1A(3) it can be seen that most of the large dust particles are removed after application of voltage resulting in negligible particle residue. However, Figure 3-1B shows the dust particles that remain after application of voltage in the small particle size regime (~15 $\mu m$). As shown in the microscope image in the expanded inset, a significant portion of the surface is covered by particles even after the voltage application. This is because for small particles force of adhesion dominates electrostatic force of repulsion as shown in the schematic of Figure 3-1C.

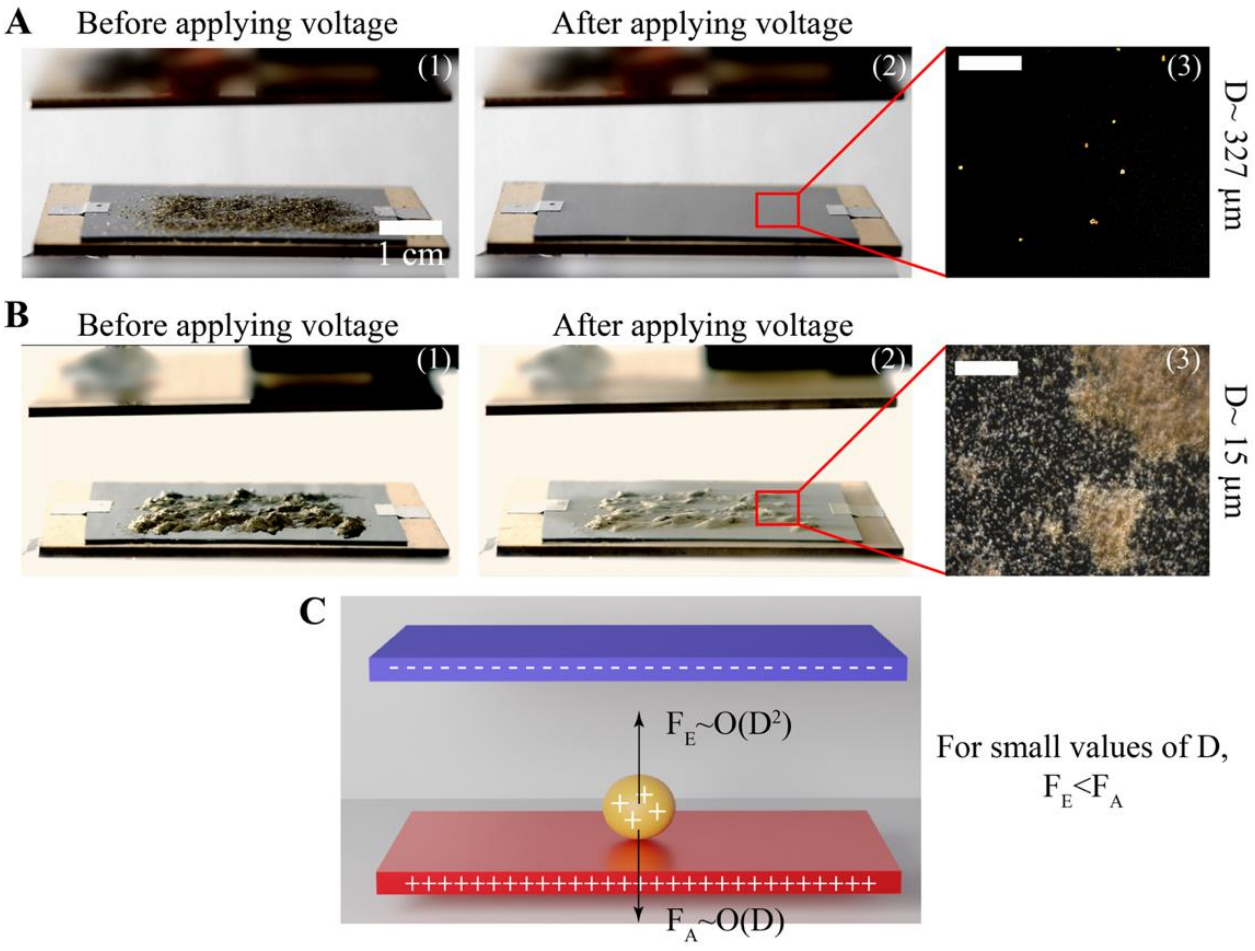


Figure 3-1. **Smaller dust particles are challenging to be electrostatically repelled from a conductive surface compared larger particles. (A)** (1) Dust particles of average size ~327 $\mu m$ resting on smooth silicon wafer before application of voltage. (2) On application of high voltage (~ 15 kV) between the electrode gap (~3 cm) the dust particles are repelled off from the surface of

the electrode. (3) Microscope image of dust particles remaining after application of voltage. It can be seen that most particles are removed. Scalebar in the expanded inset is 5 $mm$. **(B)** (1) Dust particles of average size ~15 $\mu m$ resting on smooth silicon wafer before application of voltage. (2) A significant portion of the particles remain on the surface even after application of high voltage. (3) Microscope image of remaining dust particles. Major fraction of the surface remains covered. Scalebar in the expanded inset is 500 $\mu m$. **(C)** Particles are charged via induction where charge of same polarity as that of the contacting electrode is induced on the dust particles. Electrostatic force of repulsion scales proportional to the square of particle size $F_E \sim O(D^2)$. For small particles, Van der Waals force acts to retain particles on the surfaces. Even though the absolute value of Van der Waals force of adhesion reduces with particles size $F_A \sim O(D)$, $F_A$ dominates $F_E$ as particle size $(D)$ reduces below a critical value.

Removing particles below 30 microns is crucial in solar panel application since the dust particle size distribution often shows (in about 60% of the cases) a mean value below 30 $\mu m$ as characterized in data collected from several solar farms around the world [96]. Thus, for efficient operation of solar power farms, small particles have to be removed to completely eliminate the usage of water. Since electrostatic force cannot be increased beyond a critical point of 3 MV/m, the only practical way to remove smaller particles is by reducing the Van der Waals force of adhesion.

Van der Waals force is universal in nature and acts between all kinds of materials within a short-range of less than ~1 nm [108–110]. There are mainly two ways of reducing Van der Waals force; by changing the surface chemistry to reduce the Hamaker constant or by changing the surface morphology to reduce the degree of contact between particle and substrate [111,112]. Since electrostatic dust removal applications require transparent conductive surfaces, the material choices for varying Hamaker constant are very limited. Moreover, the order of magnitude of Hamaker constant that affects the Van der Waals force of adhesion does not have significant variability across conductive materials ($\sim 10^{-20}\ J$) [108]. Therefore, reducing the degree of contact between particle and substrate is one of the most effective ways to reduce Van der Waals force of adhesion [83].

There are several surface morphology modifications for reducing the particle-surface degree of contact. Different types of texture patterns on various scales can be fabricated on the surface. Since solar panel application is mostly confined in the microparticle regime, the effect of texture is apparent only when the size of the texture is comparable (micron scale texture) or smaller than

that of the particle size (nano-scale texture). There are various microscale features that can be introduced on surfaces such as micropillars, cones, pyramids etc. [113]. There are also a variety of nanoscale textured surfaces that offer more dense, smaller scale features that could have significant impact on the force of adhesion [114]. Finally, there are hierarchical structures with hydrophobic chemistry (lotus leaf like) such as micro-nano hierarchical structures along with hydrophobic coatings that have been attempted for introducing self-cleaning effect on solar panels [115]. However, self-cleaning effect works only when there is rain or water-based washing [116]. Moreover, the hydrophobic modifier renders the surface of the panel electrically insulating and therefore cannot be used in electrostatic dust removal applications.

In this chapter we investigate the effect of surface texture on the efficacy of electrostatic dust removal in the microparticle regime relevant for photovoltaic application. We demonstrate that nanoscale textured surfaces significantly reduce the force of adhesion of dust/micro particles compared to micro-scale textures. We performed electrostatic dust removal experiments and show that the reduced adhesion manifests as a significant reduction (up to ~3.5-fold) in dust residue after the application of voltage. We quantify the reduction in adhesion force due to texture by performing AFM pull off experiments and show that nanoscale texture reduces the force of adhesion by up to 2 orders of magnitude compared to plain untextured surface, thus presenting a compelling case for having nano-textured surfaces for enhancing small particle dust removal. Last, we fabricate transparent, electrically conductive, nanotextured surfaces for solar panel application and demonstrate that up to 90% of the lost power output can be recovered for small microparticle fouling (<30 $\mu m$), thus making electrostatic dust removal technology significantly more effective in the small-particle regime.

## 3.3. Results and Discussion

### 3.3.1. Nanotextured surface is significantly more effective for electrostatic dust removal

The adhesion of a micrometric dust particle onto a surface is a sub-micron phenomenon. At a single particle level, the region of contact between particle and substrate is much smaller than the particle size itself for all kinds of substrates [82,109]. For surface cleaning application, prior to investigating a single particle-surface interaction, we experimentally study the removal of dust

particles as a collection from textured and non-textured surfaces. This is crucial since the loss of power output in solar panels due to dust accumulation is a function of total dust coverage.

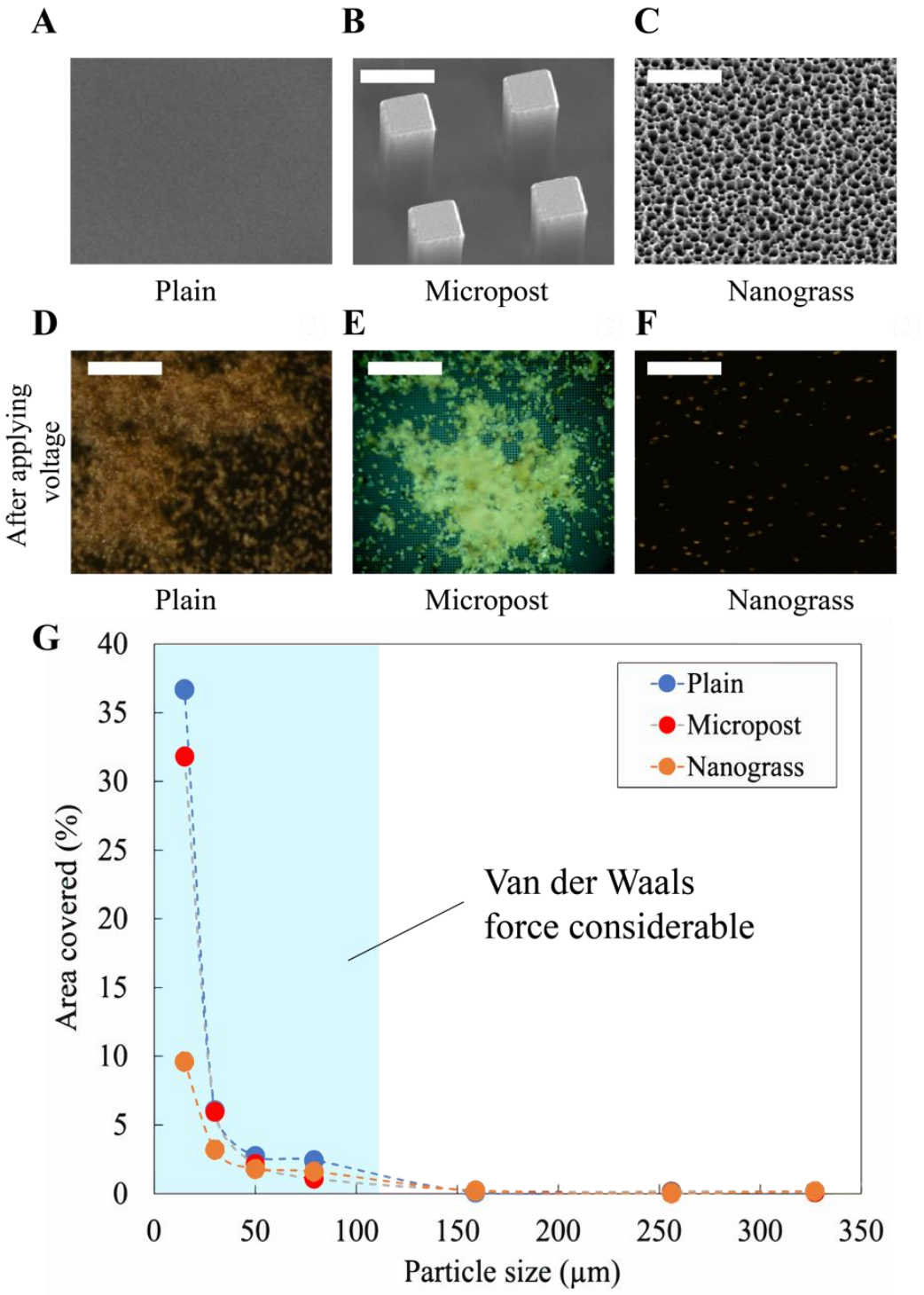


Figure 3-2. **Effect of surface texture on electrostatic dust removal. (A), (B), (C)** SEM images of pristine silicon, micro-post textured silicon (5 $\mu m$ posts, scalebar is 7 $\mu m$) and nanograss

(scalebar is 2 $\mu m$) textured silicon before deposition of dust particles. **(D)** Dust residue remaining after application of voltage on a plain surface. It can be seen that for small particle sizes there is significant surface coverage even after the application of voltage. The representative image is for dust particles of average size 15 $\mu m$ **(E)** Performance of micron-scale texture for electrostatic dust removal. It can be seen that even after application of voltage there is a significant fraction of the surface covered by dust particles. **(F)** Electrostatic dust removal from nano-grass surface. Since nanoscale surface significantly reduces the degree of contact between particle and substrate it can be seen that most of the dust particles are removed after application of voltage. **(G)** Dust removal as a percentage of surface area coverage after electrostatic dust removal for different particle sizes. For large particles >100 $\mu m$ surface texture has no effect since force of adhesion is negligible. But for particles <100 $\mu m$ in size, it can be seen that the effect of texture starts to play a role. For the smallest particle size ~15 $\mu m$ it can be seen that nano-textured surface performs significantly better compared to micro-post surfaces. It can also be seen that the performance of micron-scale texture is only nominally better that the plane surface. Scalebar in images (**D)**, (**E)**, (**F**) are all 200 $\mu m$. The applied voltage in all experiments was 15 kV and the electrode spacing was 3 cm.

Even though there are various kinds of surface textures that can be fabricated, including groves, cones, posts etc., [117,118] we are primarily interested in the effect of the scale of texture because the force of adhesion, is at the first order, dependent the RMS surface roughness [85,119]. We therefore fabricated micro-post array surfaces and nanoscale textured "nanograss" surfaces that are "gold standard" surfaces for micro and nano scale textured surfaces respectively on pristine silicon wafers. Micro-posts were fabricated using standard photolithography [120] and nanograss was fabricated using reactive ion etching (RIE) [121]. This also enables us to perform highly repeatable experiments. Figure 3-2(A, B, C) shows SEM images of pristine silicon, micro-post textured silicon and nanograss respectively before covering the surface with dust.

We performed systematic electrostatic dust removal experiments where the silicon wafer was connected as the bottom electrode between two parallel plate electrodes (spacing ~3cm) similar to the experiments in figure 1 and the applied voltage was 15 kV. We limited the applied voltage to prevent electrical arcing between the sharp edges of the electrodes. At the start of a set of experiments, the substrate was fully covered with dust particles before applying voltage. Followed by application of voltage, we imaged the residual dust particles using microscope as shown in sample experimental images Figure 3-2 (D, E, F). It can be seen that while plain and micro-textured

surfaces retain a significant portion of small dust particles, nanotextured surface almost completely repels off the dust particles with negligible residue left.

We quantify the dust removal for dust particles of different average sizes as shown in Figure 3-2G. For large particles >100 $\mu m$ there is negligible effect of surface texture because Van der Waals force of adhesion is much smaller than electrostatic force of repulsion. However, as particles size becomes smaller (<100 $\mu m$) it can be seen that dust particle removal becomes harder due to domination of adhesion as also evident by the increase in percentage area covered. As particle size become smaller than ~30 $\mu m$, a significant portion (>30%) of the surface area is covered by dust particles for both plain and micro textured surfaces. Micro textured surface, however, is nominally better, due to slightly reduced degree of contact between dust particles and the surface. However, since the size of textures are on the same order as that of dust microparticles, most of the dust particles distributed atop microposts "experience" an essentially flat surface. As a result, on average, the total dust coverage when we use microtextured surface is comparable to that of plain surface. However, when the surface is nano-textured, there is significant improvement in dust removal as shown in Figure 3-2F. Nanotexture introduces voids at the nanometric region of contact between particles and substrate, resulting in much lower adhesion and significantly better electrostatic dust removal [85,92,114].

### 3.3.2. Quantifying the force of adhesion using AFM pull-off experiments

Macroscale dust retention on the substrate after application of voltage is affected by the adhesion force of particle-substrate interactions. To probe this further, we study a single particle system where the adhesion of a single microparticle on plain, microtextured and nanotextured surfaces are investigated. For this, we use Atomic Force Microscope to quantify the parameter called "pull-off" force which is the critical force required to remove a particle from the substrate [89,114].

The pull-off force measurements were performed using a multi-mode atomic force microscope (AFM) operated on a Nanoscope 5 controller (Bruker). Colloidal probes were used in the force spectroscopy measurements [122]. Dust particles were modeled by attaching spherical silica ($SiO_2$) bead of radius $25 \pm 0.5\ \mu m$, as shown in Figure 3-3A. Cantilevers with spring constants

ranging from 0.1 nN/nm to 100 nN/nm were used for pull-off force measurements. The spring constant was chosen specifically for each experiment to maximize force sensitivity, while constraining the cantilever deflection within the linear range (see Experimental Methods). Prior to the experiments, the spring constants of the cantilevers were determined based on the ambient thermal fluctuations. We also eliminated static charge effect by electrically grounding the substrate and the experimental setup.

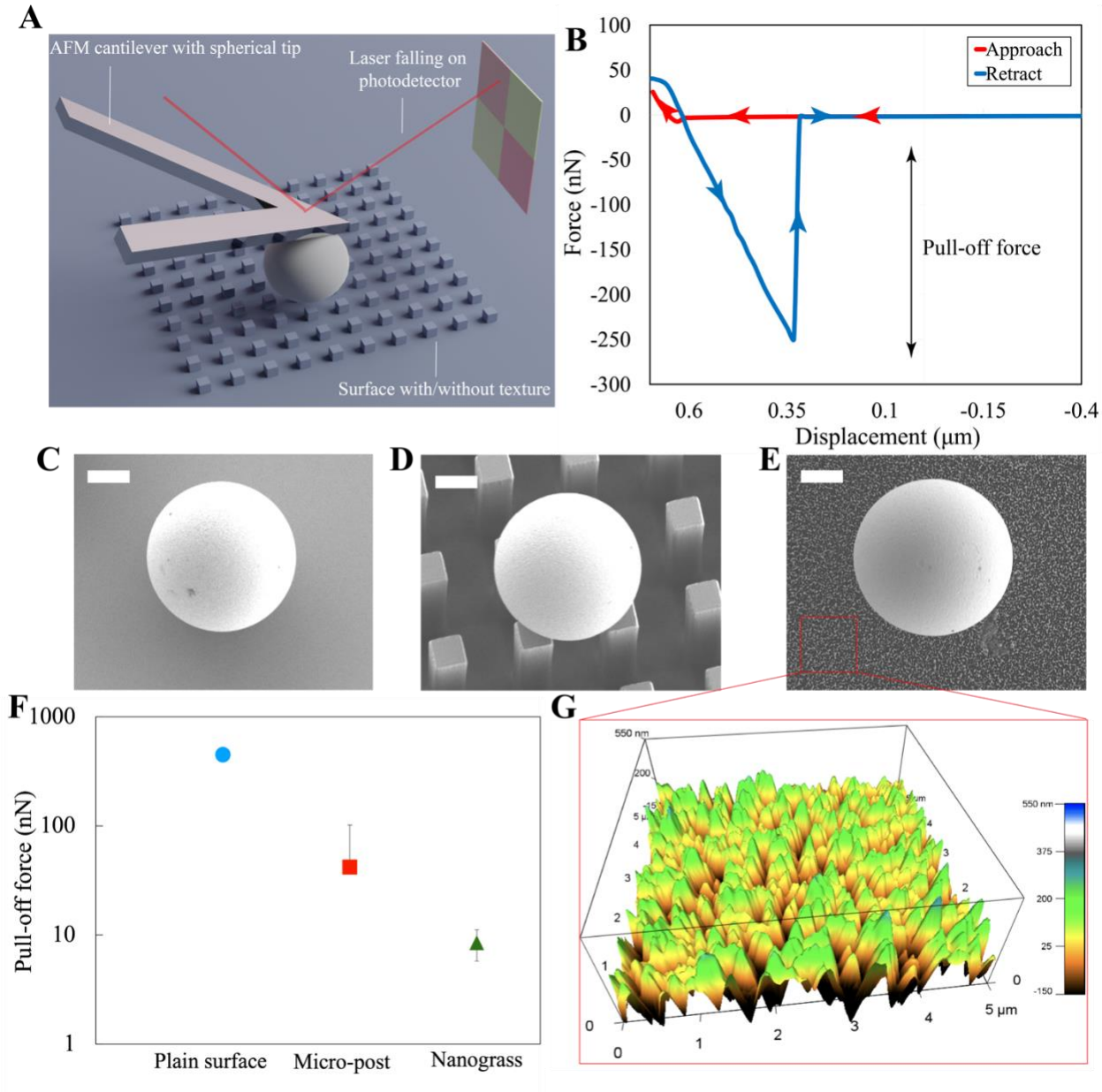


Figure 3-3. **Nanotexture reduces force of adhesion significantly compared to micro-scale texture. (A)** Schematic showing AFM pull-off force experiment. The tip of the cantilever is

attached with a silica microbead. The laser from the beam source reflects off of the top shiny surface of the cantilever and a photodiode detects a change in voltage. The voltage change is converted to cantilever deflection which is converted to a force measurement by using the beam stiffness value. **(B)** Plot showing force vs displacement in a typical pull-off force experiment. The cantilever snaps onto the surface during approach (red) and snaps off from the surface during pull-off or retraction (blue). Pull-off force is manifested as a sudden jump in the force-displacement curve. **(C)**, **(D)** and **(E)** SEM images of microparticle (~25 $\mu m$) resting on plain, microtextured and nano-textured surfaces respectively. From **(E)** it can be seen that the features are much smaller compared to particle size in the case of nano-textured surface. Scalebar is 5 $\mu m$**. (F)** Pull-off force measurements. Nanotexture reduces the pull off force by about two orders of magnitude compared to a plain surface. There is some reduction in the average pull-off force while using micro-post surface. This is attributed to the particle attached on cantilever contacting post edges or post corners and thereby reducing the degree of particle-substrate contact. **(G)** AFM surface image of nano-grass surface. The feature height and width are both ~200 nm, an order of magnitude smaller than microparticles.

Figure 3-3B shows a typical pull-off force experiment where we plot the force measured using AFM cantilever as a function of z-axis movement. During the cantilever approach to the substrate surface (red line) the force is initially close to zero and suddenly the probe snaps onto the substrate as shown by a sudden jump in the red curve. To measure pull-off force, the cantilever is retracted away from the substrate, but the particle attached at the tip of the cantilever remains on the substrate due to Van der Waals force of adhesion, resulting in cantilever bending which appears as a sloped negative force measurement as shown in the blue curve of Figure 3-3B. Pulling the cantilever further away from the substrate causes the particle to suddenly snap off from the surface resulting in a sudden jump in the force-displacement curve a shown in Figure 3-3B. This is the pull-off force.

We performed several AFM pull-off experiments on plain, microtextured and nano-textured surfaces using 25 $\mu m$ silica bead attached to cantilever tip. Figure 3-3C, D, E show SEM images of 25 $\mu m$ silica bead on different surfaces, to demonstrate the scale of the particle and scale of surface texture. While the micropost size is comparable to particle size, nanograss texture is significantly smaller (Figure 3-3E).

Figure 3-3F plots the average pull-off force to remove 25 $\mu m$ cantilever bead from the three substrates. As shown in the plot, plain surface has highest Van der Waals force. The force measurement was very consistent between experiments with relatively small error bars.

Microtextured surface pull-off force experiments have high variability depending on the location where cantilever bead taps on the surface. Each force measurement marker the plot is an average of 192 pull-off force measurements obtained by tapping different points on the substrate from a square grid of $8 \times 8$ points spaced apart by 2 microns at 3 different locations on the substrate. Thus, depending on the relative orientation of the $8 \times 8$ tapping grid and the micropost array, the pull-off force measurement varies significantly between experiments as shown by the error bar. When the cantilever bead taps exactly on top of the post, the pull off force measurement is the highest and is comparable to that of plain surface force measurements (Figure 3-4A, Figure 3-4B). When the cantilever bead is simultaneously contacting the corners of microposts as shown in D the pull off force is the lowest (Figure 3-4C). On an average however, the pull of force is still significantly higher than that of the nanograss substrate.

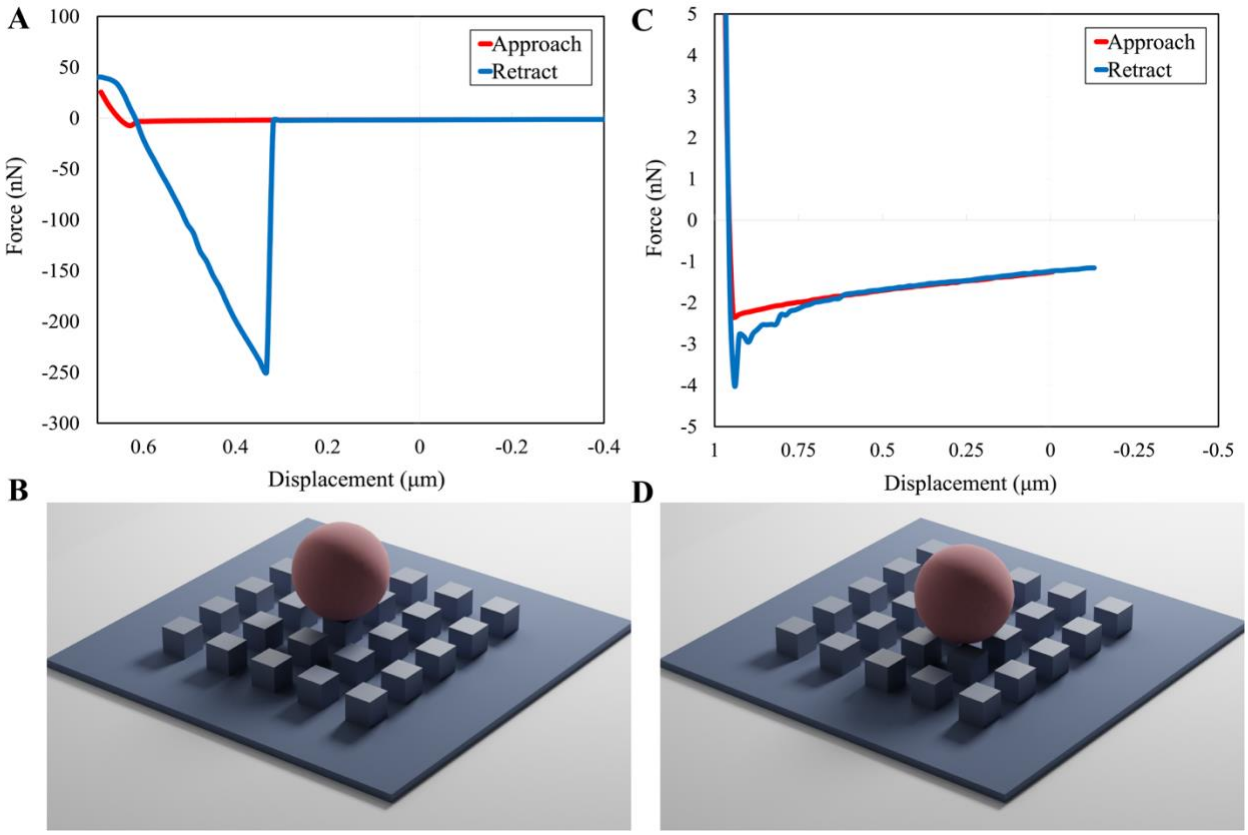


Figure 3-4. **AFM pull-off force dependence on the relative position of the particle compared to micro-posts. (A)** Pull-off force measurement from micro-post surface showing a pull-off force as high as a plain surface (~250 nN). **(B)** The pull off force value indicates that the cantilever bead could be touching exactly on top of a post such that the region of contact between particle and the substrate is like a sphere-plain contact. **(C)** Pull-off force measurement from micro-post surface

showing a low value pull-off force (~4 nN) **(D)** The low value of pull-off force results from the reduced degree of contact between particle and substrate in the case where the particle is exactly resting between 4 posts where the particle-surface contact is limited to the contact at 4 corners of 4 different adjacent micro-posts.

In dust removal experiments where the particle size has a non-monodisperse distribution, there will be set of particle sizes that are less than, almost equal to and larger than the post-spacing. The advantage of having micro-post texture for reducing adhesion is only realized for those particles in the distribution that end up being deposited exactly between the edges or between the corners of microposts. In all other cases, the particles either rest exactly on top of one or multiple microposts. Moreover, there could be certain particles that might end-up getting stuck between the posts which might be even harder to remove compared to removing dust particles from a plain, untextured surface. Therefore, removal of dust particles from micro textured surface to reduce the total surface residue after application of voltage is challenging as demonstrated in Figure 3-2E.

### 3.3.3. Fabrication of transparent, electrically conductive, nanotextured glass

As demonstrated in Figure 3-3, nanotexture significantly enhances electrostatic dust removal. However, for applying this concept to solar panels, we require the following characteristics for the solar panel surface- (1) high transparency for letting sunlight through, (2) electrical conductivity for inducing charge on dust particles and (3) nanotexture for reducing Van der Waals force of adhesion. Thus, our goal to achieve practical application is to fabricate a novel surface that is transparent, electrically conductive and nanotextured at the same time.

Fabrication of a glass surface with above characteristic could be visualized as a two-step process (1) texturing the glass and (2) coating the texture with any TCO (Transparent Conductive Oxide) material such as Indium doped Tin Oxide (ITO) or Aluminum doped Zinc Oxide (AZO). There could be several potential techniques to fabricate textured glass including chemical etching [123], nanowire growth via sol-gel process [124,125], laser etching [126] etc., resulting in different kinds of textures. Scalability of the etching process for different sample sizes is a major consideration for practical application. Therefore, we use a copper nanodrop-mask based reactive ion etching process to create nanotextured glass [127]. This is a multi-step process.

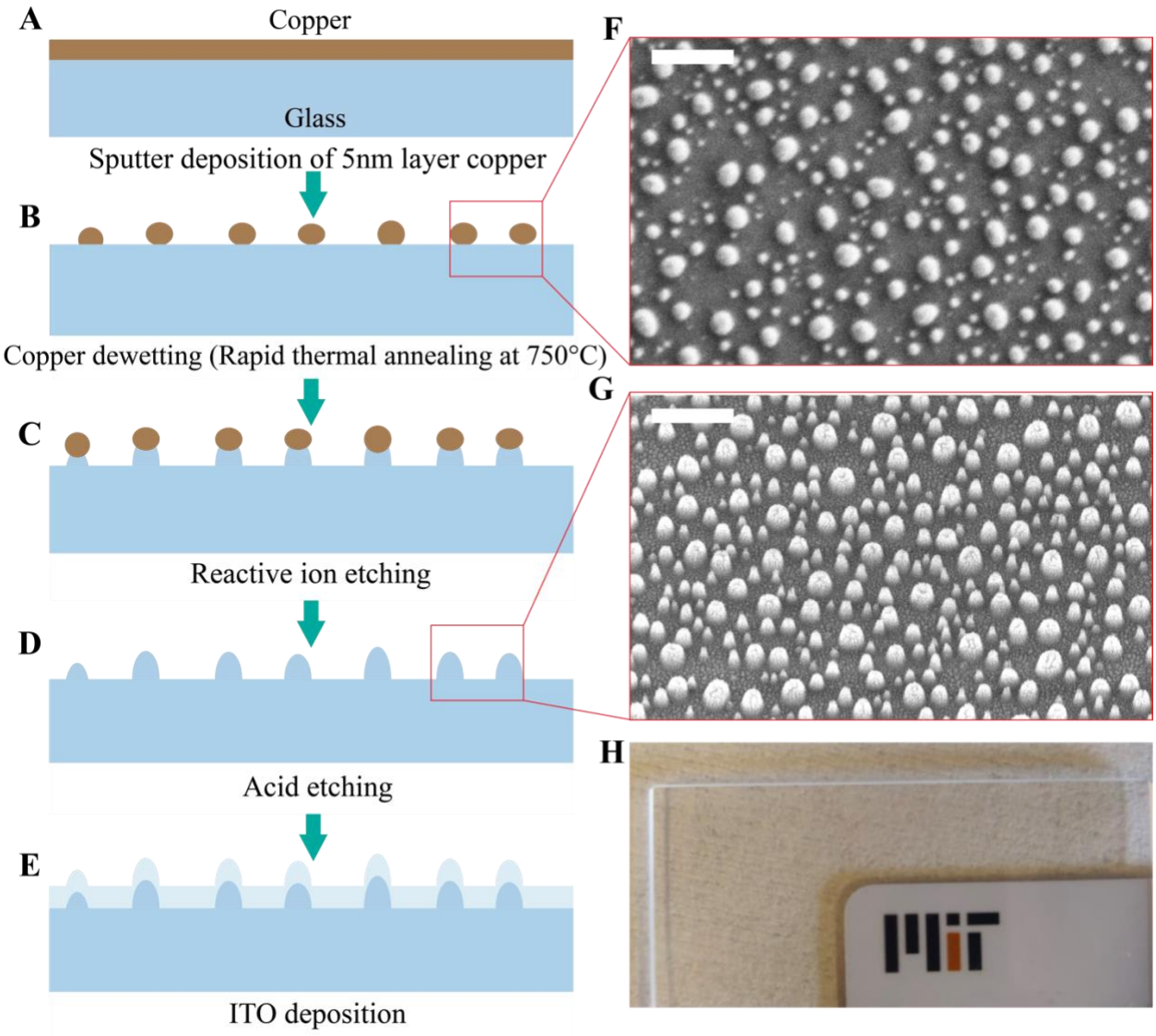


Figure 3-5. **Fabrication of transparent nano-textured electrically conductive glass (A)** In the first series of steps, we fabricated nano-textured glass before depositing ITO. In the first step a 5nm thin copper layer is sputter deposited on the fused silica glass substrate of thickness 2 mm. **(B)** In the second step we heat the substrate to 750 $^{o}$C which is not above the melting point of copper but is just enough to de-wet the copper layer to form nanometric copper droplets. Figure **(F)** shows the SEM images of copper droplets after solidification. Scalebar is 500 nm. These droplets, when cooled down act as a nano-mask for etching the glass surface. **(C)** Then we etch the substrate using Reactive Ion Etching resulting in nano features with copper deposition atop the features. This happens because copper acts as a mask and remaining portion of the glass is exposed to RIE process. **(D)** Then we wash away the copper using acid washing resulting in nano-grass like features on the glass as shown in figure **(G)**. By the end of this step, we obtain transparent nano-textured glass. **(E)** In the last fabrication step we conformally coat the surface with 15 nm

thick ITO to make the surface conductive while maintaining transparency and surface features. **(H)** Image of the glass surface for qualitative demonstration of transparency.

In the first step as shown in Figure 3-5A we sputter deposit a 5 nm thick copper layer on the fused silica (softening point 1700 $^{o}$C) glass substrate of thickness 2 mm and a characterization sample size of 2.5cm x 2.5cm. In the second step we heat the substrate to 750 $^{o}$C (rapid thermal annealing) which is below the melting point of copper (1085 $^{o}$C) that makes it de-wet from the glass surface to form nanoscale copper droplets as shown in Figure 3-5B. After the substrate cools down, the copper droplets solidify, to form nanoscale mask on the glass surface as shown in the SEM image of Figure 3-5F. Then we etch the substrate using Reactive Ion Etching (Figure 3-5C) which results in nano features with copper deposition atop the features. This happens because copper will not get etched and acts as a mask, whereas the remaining portion of the glass is exposed to RIE process. Then we wash away the copper using acid washing (Figure 3-5D) resulting in nano-grass like features on the glass as shown in the SEM image of Figure 3-5G. By the end of this step, we obtain a transparent nano-textured glass with average feature size ~150 nm (Figure 3-5G and Figure 3-6) and high transmittance (Figure 3-8).

In the last fabrication step we conformally coat the surface with 15 nm thick ITO to make the surface conductive while maintaining transparency and surface features (see Experimental Methods for more fabrication details). Figure 3-5H shows the **i**mage of the glass surface for qualitative demonstration of transparency (also see Figure 3-7). For performing control experiments, we also fabricated plain glass surfaces with 15 nm thick ITO coating. Figure 3-6A and Figure 3-6B shows the AFM surface morphology of nano-textured glass. It can be seen that the scale of the morphology is comparable to that of silicon nanograss surface. In Figure 3-6C we plot the AFM pull off force of 25 $\mu m$ silica beads from nanotextured and plain glass surfaces. It can be seen that there is significant reduction in force of adhesion similar to the case of silicon substrate. The pull-off forces were measured for textured and untextured samples and were found to be ~120 nN and ~10 nN respectively (Figure 3-6).

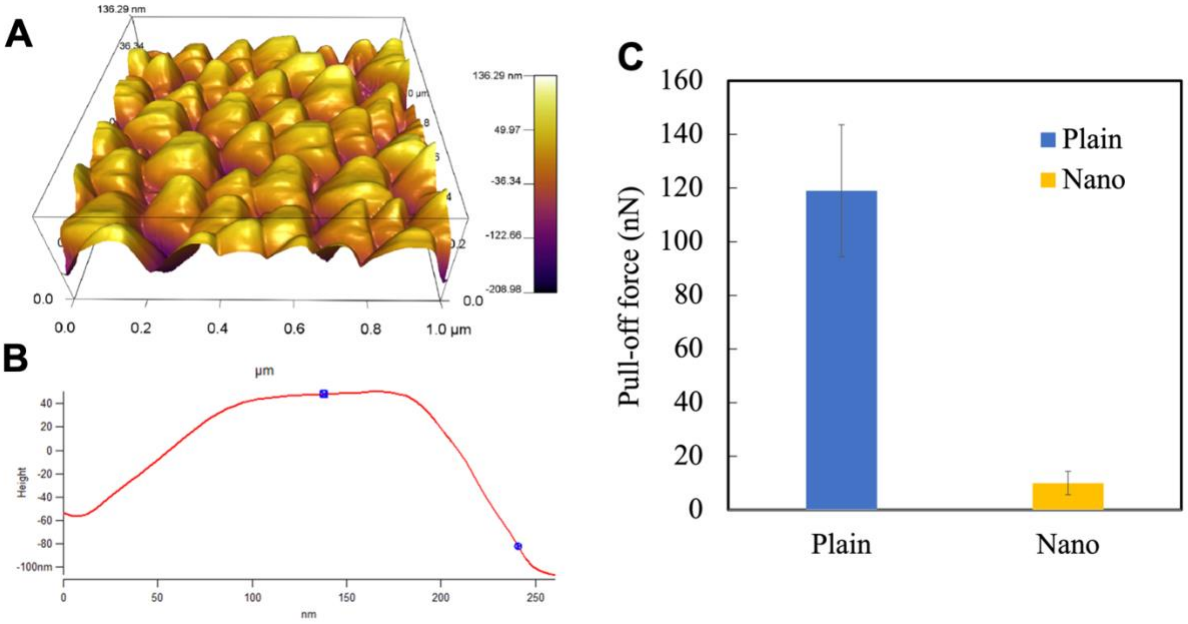


Figure 3-6. **AFM morphology and pull-off force measurement from transparent, nanotextured glass. (A)** AFM surface morphology of nanotextured glass. The features are about 200 nm in width and 150 nm in height, similar to nanograss feature size on silicon. **(B)** AFM surface scan of a single nanofeature showing nanometric dimensions. **(C)** AFM pull off force measurements from glass surface vs nano-textured glass. It can be seen that nanotexture significantly reduces the force of adhesion.

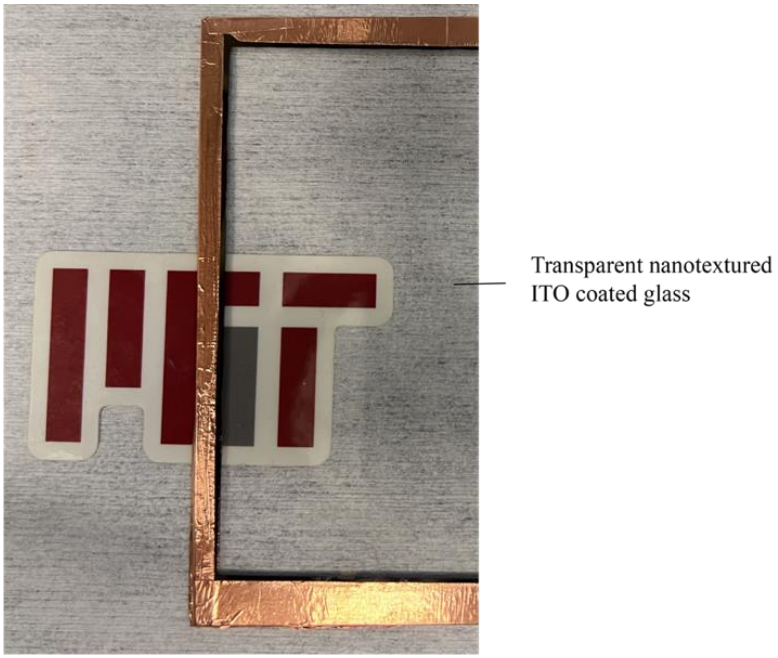


Figure 3-7. **Qualitative demonstration of transparency of the fabricated substrate.**

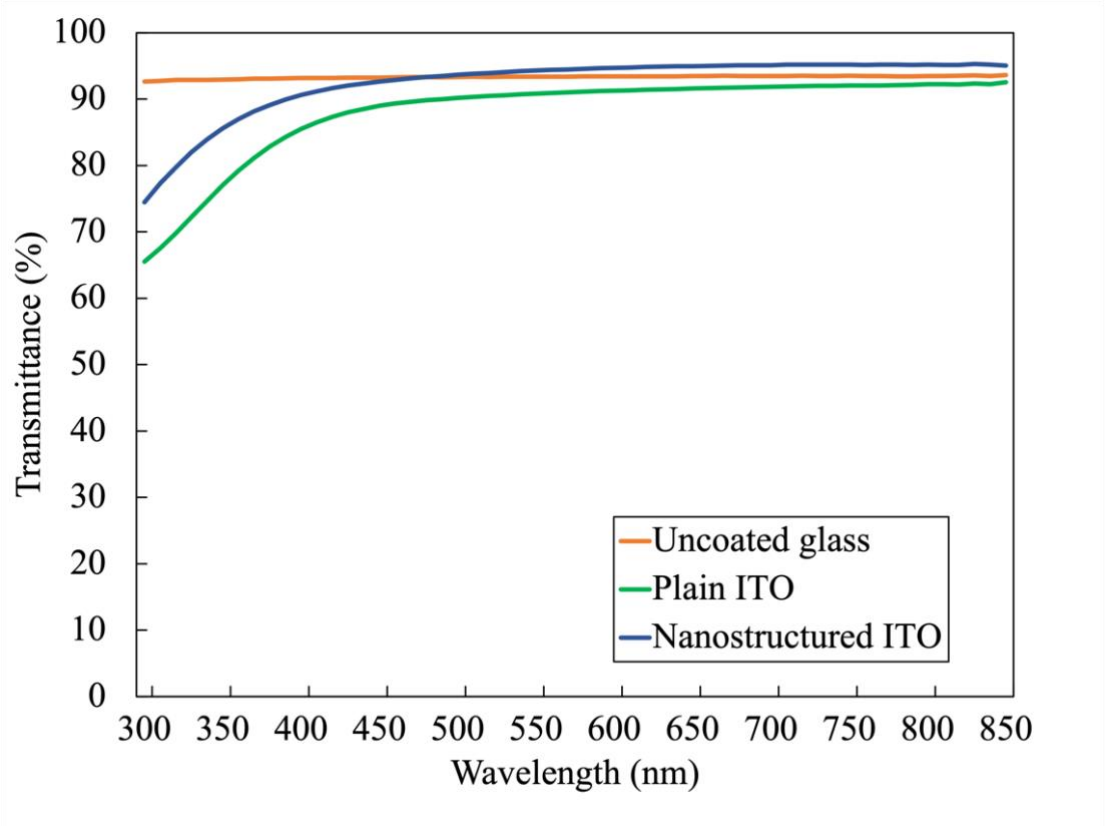


Figure 3-8. **Transmittance of various glass substrates.** In the visible spectrum, especially in the higher wavelength, nanotextured ITO glass substrate has higher transmittance than that of the plain uncoated glass. Nanotextured glass has higher transmittance compared to plain ITO coated glass at all wavelengths.

### 3.3.4. Power output recovery

Last, we designed and fabricated a larger (10cm x 10cm) sample of transparent, electrically conductive, nano-textured glass using the steps described in Figure 3-5 for retrofitting on top of a mini lab scale solar panel (output 1 W). The textured surface was coated with a 15 nm thick ITO (Indium doped Tin Oxide). For solar panel applications, power output recovery is the parameter of interest regardless of the surface area coverage by dust residue. Therefore, we performed dust repulsion experiments using different dust particles and quantified the power output before and after dust removal. The control experiments were performed using ITO coated plain glass surfaces. High-voltage supply was connected to the glass electrode and another parallel plate metallic electrode was used as the electrical ground with electrode gap of 1 cm between both electrodes (~10 kV applied) as demonstrated in Figure 3-9A (see Experimental Methods).

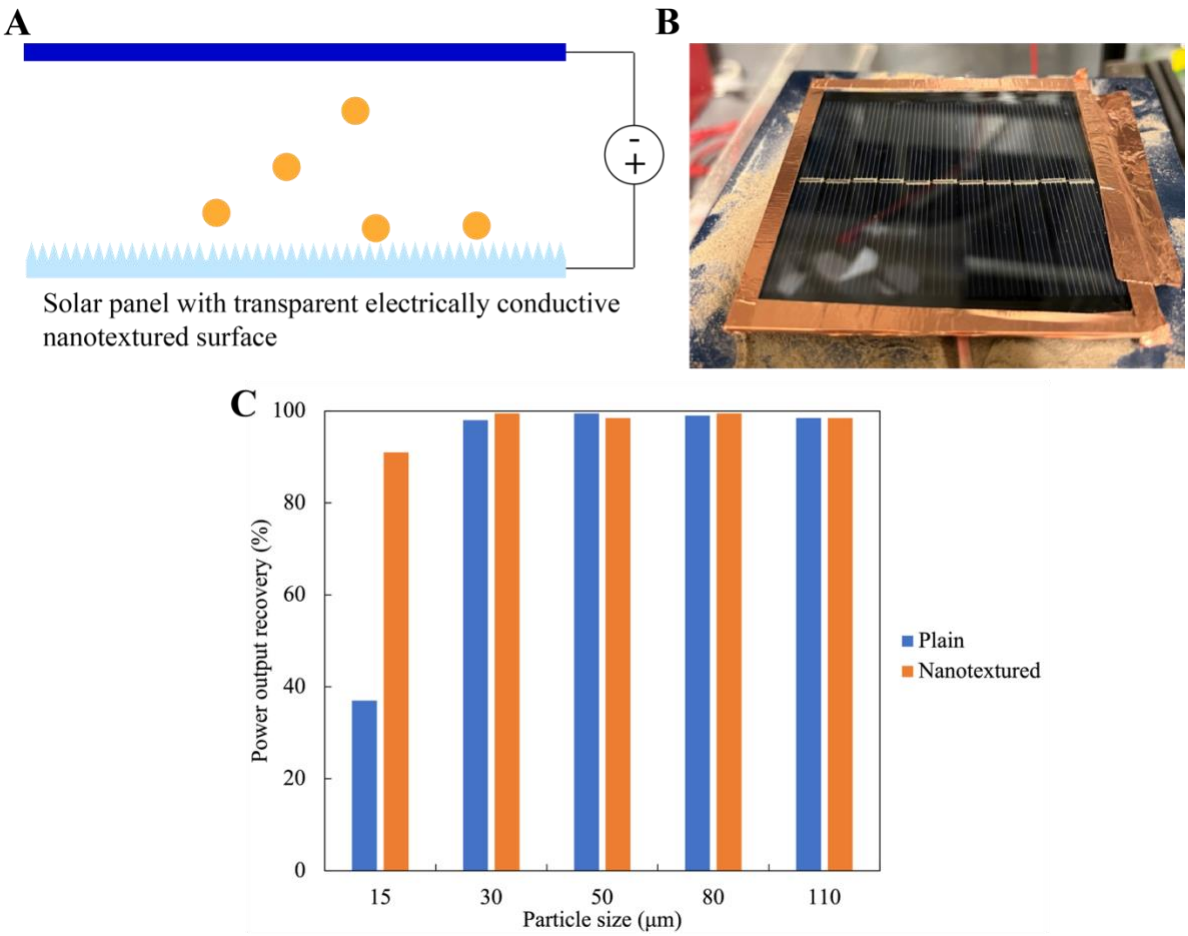


Figure 3-9. **Enhanced power output recovery using nanotextured surface. (A)** Schematic of the experimental setup for performing dust repulsion from solar panel. Transparent nanotextured conductive surface is installed on top of a mini solar panel surface. Potential difference (~12 kV) is applied between the panel surface and a top electrode placed at a 2cm gap. The dust particles are removed, and the power output is measured by bringing the solar panel under a white light source. Power output was measured by measuring the voltage drop across a known resistor connected between the solar panel leads. **(B)** Lab-scale solar panel (5 W) with nanotextured glass installed atop. **(C)** Power output recovery using transparent conductive surfaces with and without nanotexture. Both surfaces perform equally well for particle sizes >30 microns. However, when particle size is ~15 microns nanotextured surface can recover ~90% of the lost power output whereas plain non-textured surface can only recover ~38%, providing a significant enhancement to the existing electrostatic dust removal system.

Figure 3-9B shows the surface of the solar panel with conductive nanotextured glass installed. Voltage was applied to the electrode using copper tapes (see Experimental Methods). We performed dust repulsion experiments using various particle sizes ranging from 15 $\mu m$ to 110 $\mu m$ and quantified the power output recovery. The power output was measured by measuring the

voltage across a resistor (1000 ohm) connected between the solar panel leads (see Experimental Methods). Figure 3-9C shows the power output recovery for different particle sizes using plain and nanotextured surfaces where the power output is normalized by the power output in the absence of any dust particles. For large particles above 30 $\mu m$, both plain and nanotextured surfaces perform equally well, recovering almost 99% of the lost power output since electrostatic force of repulsion overcomes adhesion. However, as particle size gets smaller (~15 $\mu m$) and adhesion dominates, it can be seen that for plain surface only ~38% of the lost power output can be recovered whereas nanotextured surfaces enable ~2.4X more power output recovery (>90%).

Our approach demonstrates that by making use of surfaces with texture dimension an order of magnitude smaller than that of the size of target dust particles, we can significantly enhance the capabilities of charge induction based electrostatic dust removal systems. By enabling removal of almost all of the dust particles above 15 $\mu m$, our electrostatic dust removal approach ensures the operation of more than ~70% of the solar farms with zero water footprint[27].

## 3.4. Experimental Methods

### 3.4.1. AFM pull-off force experiments

The pull-off force measurements were performed using a multi-mode atomic force microscope operated on a Nanoscope 5 controller by Bruker. Since dust particles consist of ~75% silica ($SiO_2$) [76,77] we attached a silica bead of radius $25 \pm 0.5\ \mu m$ to the cantilever tip. Cantilevers with spring constants ranging from 0.1 nN/nm to 100 nN/nm were used for pull-off force measurements. For plain surface, since force of adhesion was highest, the AFM measurement will either become non-linear or saturate for low spring constants. Therefore, we selected stiffer cantilever (~100 nN/nm) for plain surfaces and compliant one (~0.1 nN/nm) for nanograss experiments. The spring constants of the cantilevers were calibrated based on the ambient thermal fluctuations. Static charge build up was prevented by electrically grounding the substrate and the experimental setup to not have its effect in force of adhesion. Finally, ambient humidity was limited to <40%, thus making capillary effects negligible [82].

### 3.4.2. Creating nanotexture on glass surface

Samples of two different sizes were fabricated using fused silica. For characterization purposes 2.5cm x2.5cmx0.1cm samples, and for the power recovery experiments 10x10x0.16cm samples were used. The fabrication of nano-textured glass contains four steps: (I) Deposition of 5nm copper film on fused silica, (II) Rapid thermal annealing (RTA), (III) Reactive ion etching (RIE) and (IV) Cleaning sample with acid (a mixture 75wt% phosphoric acid, 5wt% nitric acid, and 20wt% DI water**)**. The AJA Orion 5 sputter system was used to deposit copper at a rate of 0.05nm/s in a pure Argon atmosphere. RTA was carried out at 750 °C for 100s in 1atm N2 atmosphere using the AnnealSys AS One-150. To etch the samples, the SAMCO 230iP was used. The samples were etched for 90s at 1Pa, 400W and 30sccm CF4 and 60sccm Argon plasma.

### 3.4.3. ITO deposition on glass

The AJA Orion 5 sputter system was used to deposit indium tin oxide at a rate of 0.05nm/s in a pure Argon atmosphere. After deposition of ITO, 2-5mm wide area around the edges was sputtered with copper, enhancing the electrical contact between sample and a conductive tape, which is used as the electrical connection to the power supply (see Figure 3-7).

### 3.4.4. Transmittance measurement

The transmittance was measured with a PerkinElmer LAMBA 1050 UV/Vis/NIR Spectrometer for three different 2.5cmx2.5cmx0.1cm fused silica samples: (i) uncoated and untextured (ii) coated with 15 nm ITO and untextured and (iii) coated with 15 nm ITO and nano textured. The ITO coating on the untextured sample reduced the transmittance compared to the uncoated and untextured sample. However, the nanotexture reduces reflective losses and therefore increases the total transmittance [127].

### 3.4.5. Conductivity measurement

The conductivity was measured with a four-point probe on two 2.5cmx2.5cmx0.1cm fused silica samples: (i) coated with 15 nm ITO and untextured and (ii) coated with 15 nm ITO and nano-textured. The conductivity was measured at five different locations each, repeating conductivity measurements 25 times at each location. Finally, the average for each sample was calculated by averaging over all conductivity values. The probe spacing was 5 mm. Although the film thickness

was identical for both samples, the conductivity for the nanotextured sample is significantly lower and has a high variation, due to a larger pathlength for the current resulting from the texture and the reduced contact area between the probes and the nano-textured surface.

| Surface type | Conductivity (S/m) |
|---|---|
| Plain ITO coated | $335.7 \pm 62.3$ |
| Nanotextured ITO coated | $7.13 \pm 5.6$ |

Table 3-1. **Electrical conductivity (S/m) of plain ITO coated and nano-textured ITO coated glass**.

### 3.4.6. Power output measurements

Power output recovery from solar panels was performed on a mini 1 W solar panel purchase from Fielect. We used phlox white light to simulate sunlight inside the lab. We performed dust repulsion experiment and power output measurement separately. First, the nanotextured solar panel was installed with a parallel plate metallic electrode at the top. Dust particles of sizes from 15 $\mu m$ to 110 $\mu m$ (in separate experiments) were uniformly distributed on the solar panel surface to reduce the power output to less than 20% of the power output in the absence of dust. Then we applied ~10 kV between the solar panel and the top electrode which are spaced apart by 1 cm. After repelling the dust, we switch off the voltage and place the solar panel at a precise location below the light source. We connect the solar panel power output leads to a resistor of resistance 1000 ohm and measure the voltage across the resistor. Using the measured voltage and resistance values, we obtain the power output from the solar panel which we normalize using the power output in the absence of dust.

## 3.5. Conclusion

In this chapter we demonstrate that electrostatic dust removal for solar panel cleaning in small particle regime (<30 $\mu m$) can be significantly enhanced using nano-textured surfaces. Using AFM pull-off experiments we demonstrate that nanotextured surfaces can have up to two orders of magnitude reduction in Van der Waals force of adhesion compared to plain or micro-textured surfaces. We show that the reduction in pull-off force manifests as a ~3.5x better electrostatic removal of 15 $\mu m$ particles compared to plain or micro-textured surfaces in terms of surface area

coverage. To translate this finding into application on solar panels that require transparent surfaces, we fabricate transparent, electrically conductive, nanotextured glass that can be retrofit on top of solar panel surfaces. We fabricate the textured glass substrates using a scalable copper nano-mask based nanofabrication technique such that the approach can be also translated to full-scale solar panel glass surfaces. We design a bench-top solar panel dust removal setup with nanotextured solar panel and show that we can recover > 99% of lost power output for particles >30 $\mu m$ and recover > 90% of lost power output in the small particle regime. Given the tremendous potential and global applicability of active dust repulsion system in photovoltaics, our approach that enables significantly higher dust removal efficiency in small particle regime almost completely eliminates the water footprint of photovoltaic systems, contributing to truly sustainable operation of solar farms.

THIS PAGE INTENTIONALLY LEFT BLANK

# 4. Phase separation of water-in-oil nanoscale emulsion using non-Laplacian electric field

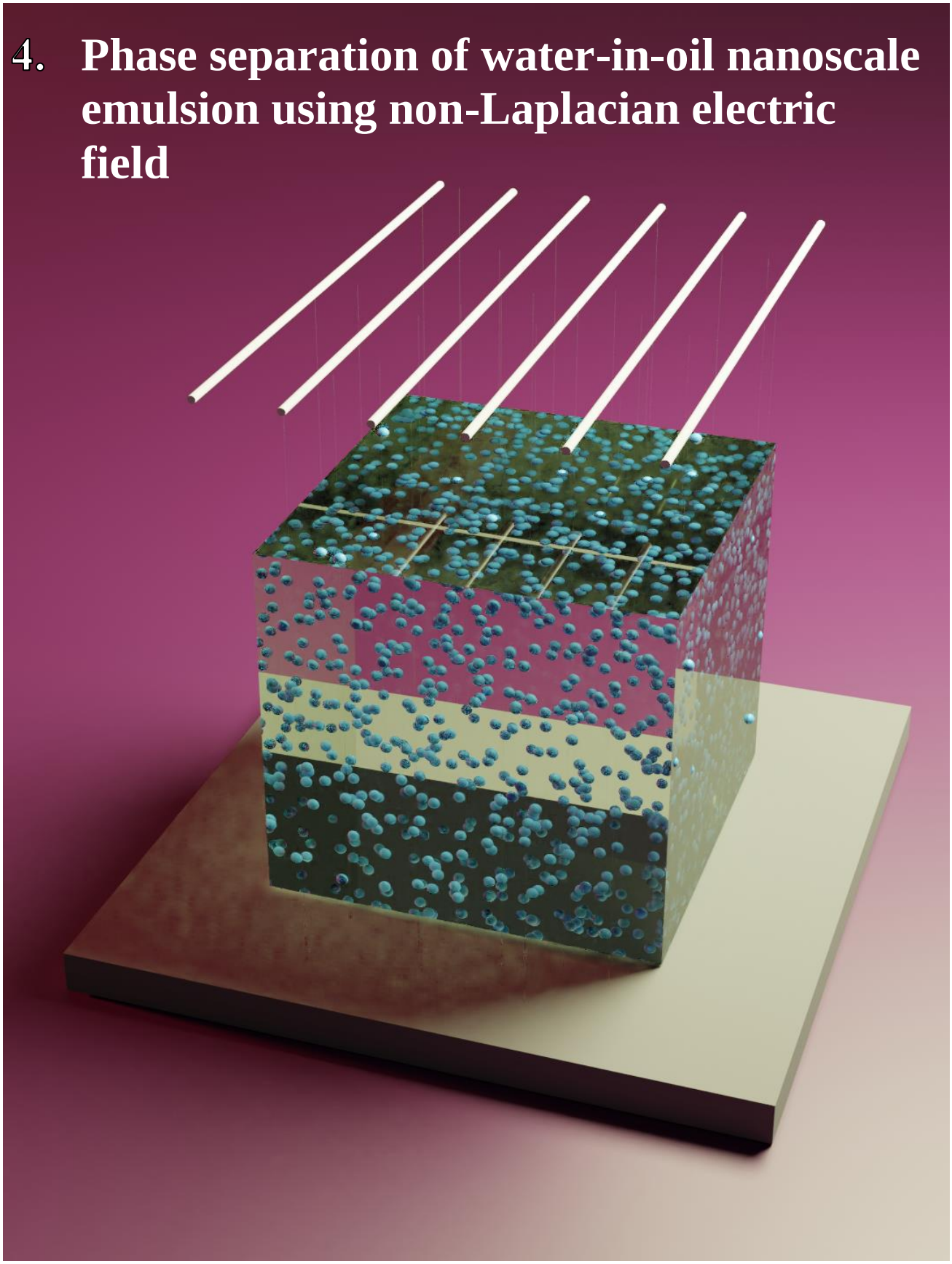

## 4.1. Abstract

Refinement of crude oil, especially oil-water separation, is one of the most complex steps in oil and gas processing industry. Crude oil extracted from the underground contains significant amounts of water in the form of emulsified droplets. Gravity-based separation of water drops from oil is impractical due to small droplet sizes, especially when they are nanoscale. Conventional electrocoalescers using immersed electrodes for oil-water separation limit their applied electric field strength to mitigate electrical shorting, making them ineffective for coalescing nanoscale droplets. Therefore, to further promote coalescence and enhance the efficiency of separation of water from oil, environmentally toxic chemicals such as demulsifiers are mixed with crude oil which end up in the effluent that reaches water bodies including the ocean and fresh water. In this chapter we propose a significantly more effective electro-coalescence method based on corona discharge that drastically enhances the rate of phase separation of nanoscale emulsions and eliminates the use of toxic demulsifiers. We demonstrate that by introducing space charge emitter electrodes that provides an air gap between the electrode and the emulsion, we can avoid droplet-mediated electrical shorting and apply ~8 times stronger electric field, resulting in much faster phase separation of water-in-oil nanoscale emulsions at different water fractions ranging from 2%-20%. We visualize the droplet chaining and coalescence events and demonstrate that the rate of oil-water separation scales with the square of applied voltage, showing that the enhanced electric field quadratically enhances the rate of electro-coalescence. Finally, we design a practical embodiment for our approach; a flow-through space-charge emitter demulsifier that enables rapid, continuous oil-water separation of nanoscale emulsions.

## 4.2. Introduction

### 4.2.1. Water-in-oil emulsion is found in various industries

Oil-water separation when one phase is dispersed in the other as emulsion is a challenge that is present across various industries[19,25]. In refineries oil spills have become frequent, with US government reporting more than 20,000 oil-spill events every year. The spilled oil gets mixed with fresh or sea water sources forming a layer of difficult to separate emulsion[128,129] and has long-lasting environmental impact[18,130,131]. In food industry, recycling of waste cooking oil is one of the ways to make food production more sustainable. However, since cooking oil often gets mixed with

water, separating water and oil is one of the most challenging steps for converting waste oil into value added products such as biodiesel[132,133].

### 4.2.2. Water-in-oil emulsion in crude oil industry

In oil extraction industry, the crude oil extracted from the underground has significant amount of water present in it, called produced water which is the naturally occurring underground water that is pumped out along with oil[23,24]. It is estimated that for every barrel of crude oil, nearly three barrels of produced water is being produced, which is the single largest waste stream generated in the oil and gas industry[25]. Produced water has considerable amount of salt content present in it ranging from 0.01-5 M[134]. The presence of salt in produced water causes challenges in the downstream refinery such as pipe corrosion, pump malfunction and catalyst deactivation. Therefore, water needs to be removed from crude oil, where ready to ship crude oil should contain no more than 0.2% water[26]. The process of removal of water from oil is called dehydration/desalting[135].

Figure 4-1. **On-shore crude oil extraction rig.** Image source: Adobe Stock Images licensed asset (#158528339).

Desalting is a complex multi-staged process broadly consisting of three steps- washing, mixing and separation. In washing step, the crude oil is heated and mixed with fresh water (also called wash water) to dilute salts, surfactants, and other water-soluble components. Salt dilution using water washing also reduces the catalyst poisoning and corrosion effects of oil-entrained water droplets in the downstream refinery. In the mixing step, to ensure proper interaction between the incoming crude oil and wash-water, the water-oil mixture is sent through mixing-valves, resulting in further breakup of water and formation of emulsified droplets in addition to the water droplets already present within the incoming crude oil[136,137]. Even though most of the water present in the oil is in the form of free water, up to 20% of water in the oil can be in emulsified form[27]. The emulsified water droplets must be removed before sending the oil for further downstream processing.

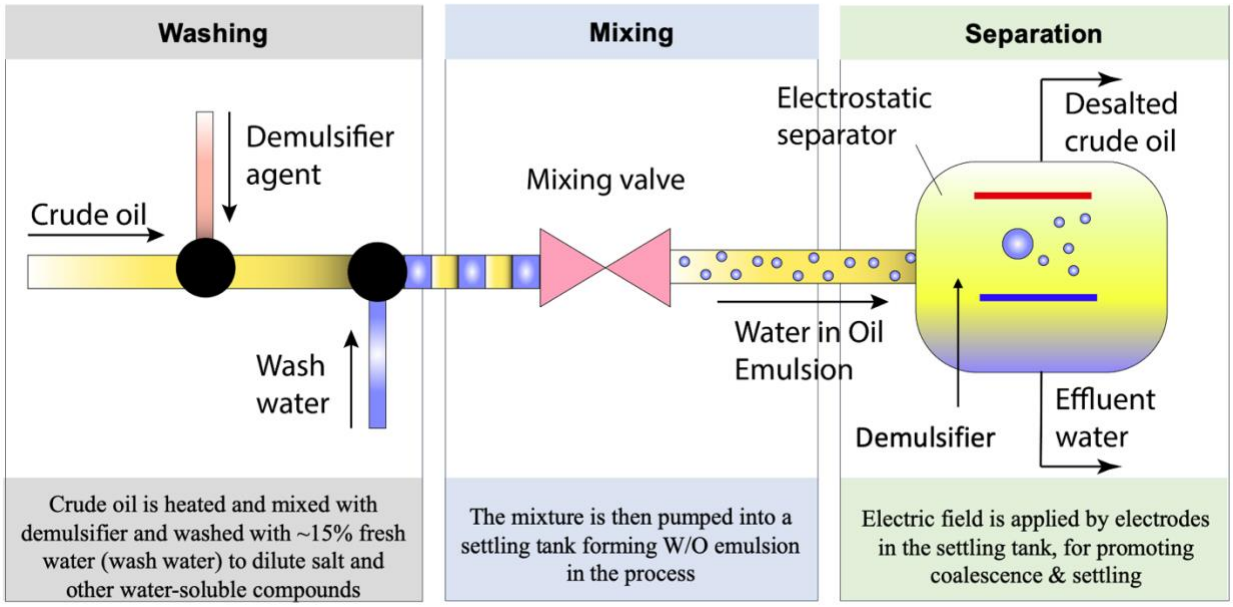


Figure 4-2. **Crude oil desalting steps.** Washing, mixing, and separation are the main processes in the complex multi-stage process of desalting. Salts, surfactants, and other water-soluble components are diluted in the washing process by heating the crude oil and mixing it with fresh water. The effects of oil-entrained water droplets in the downstream refinery's catalyst poisoning and corrosion are also lessened by salt dilution via water washing. The water-oil mixture is sent through mixing-valves during the mixing step to ensure proper interaction between the incoming crude oil and wash water. This results in additional water breakup and the formation of emulsified droplets in addition to the water droplets already present in the incoming crude oil. Up to 20% of

the water in the oil can be in the form of an emulsion, despite the fact that the majority of the water present in the oil is free water. Before transporting the oil for additional downstream processing, the emulsified water droplets must be removed.

### 4.2.3. Methods for separating water and oil phases

Among several methods for oil-water separation including mechanical[131,138], chemical[139], electrical[140–142] and magnetic[143], a combination of electrical and chemical separation methods is most commonly used. After washing and mixing, crude oil-water mixture is sent to large separation tanks. Bulk of the free water is removed by separation due to gravity owing to density difference between water and oil phases. However, depending on the size of the droplets, the emulsified droplets remain suspended in the oil for much longer duration. Often, the emulsified droplets of water present in the oil are sub-micron in size, known as nano-scale emulsion[20]. Apart from the small size of the droplets that prevent settling down, the droplets are further stabilized due to naturally occurring emulsifying agents in the crude oil such as asphaltenes that act as surfactant to prevent droplet coalescence[28,29]. Therefore, to force the coalescence of droplets, an electric field is applied using immersed electrodes in the emulsion. The electric field polarizes the saline droplets to induce dipole-dipole attraction which forces droplets to undergo coalescence[144,145] in spite of being stabilized by surfactants.

### 4.2.4. Dipole-dipole force of attraction

Applied electric field polarizes conductive water droplets in the oil. Assume that there are two droplets A and B in the vicinity of each other, with radius $a$ and $b$ respectively, whose centers are separated by distance $r$. If we assume that the electric field is acting in the z direction as shown in Figure 4-3, we can convert all vector parameters to spherical polar coordinate notations. The electric field in radial and angular directions are given as following[86].

$$E_r(r,\theta) = E_0\, cos\theta$$

$$E_\theta(r,\theta) = -E_0\, sin\theta$$

Here $E_0$ is the magnitude of external applied field. Assume that the origin is at the center of droplet B.

Dipole moment of droplet B induced by the external applied field is given by the following.

$$p_{B,r} = 4\pi\epsilon E_r b^3$$

$$p_{B,\theta} = 4\pi\epsilon E_\theta b^3$$

By substituting the expression for radial and angular components of the electric field we get expressions for the dipole moment of droplet B.

$$p_{B,r} = 4\pi\epsilon b^3 E_0\, cos\theta$$

$$p_{B,\theta} = -4\pi\epsilon b^3 E_0\, sin\theta$$

Force on a dipole due to external electric field is given by the following.

$$F = (p.\nabla)E$$

Here, the dipole B is experiencing the field induced by dipole A and the externally applied field. This field can be represented as $E_A$ and can be separated into radial and tangential components as shown below.

$$E_{A,r}(r,\theta) = E_0\, cos\theta \left[\frac{2a^3}{r^3} + 1\right]$$

$$E_{A,\theta}(r,\theta) = E_0\, sin\theta \left[\frac{a^3}{r^3} - 1\right]$$

Therefore, the force experienced by dipole B becomes the following.

$$F_B = \left[p_{B,r}\frac{\partial E_{A,r}}{\partial r} + p_{B,\theta}\frac{1}{r}\frac{\partial E_{A,r}}{\partial \theta}\right]\hat{e}_r + \left[p_{B,r}\frac{\partial E_{A,\theta}}{\partial r} + p_{B,\theta}\frac{1}{r}\frac{\partial E_{A,\theta}}{\partial \theta}\right]\hat{e}_\theta$$

In our case, since we assume that droplets align each other along z axis, we have $\theta = 0$.

Hence $\frac{\partial E_\theta(\theta=0)}{\partial r} = 0$ and $p_{B,\theta} = 0$. Thus the $\hat{e}_\theta$ component of the force $f$ vanishes.

$$F = \left[p_{B,r}\frac{\partial E_r}{\partial r}\right]\hat{e}_r$$

$$F = 4\pi\epsilon b^3 E_0 * E_0 \left[\frac{6a^3}{r^4}\right]\hat{e}_r$$

$$F = 24\pi\epsilon b^3 {E_0}^2 \left[\frac{a^3}{r^4}\right]\hat{e}_r$$

If we assume that both A and B have equal radii $a$, then the magnitude of the force of attraction between two dipoles become the following Equation 4.1.

$$F = 24\pi\epsilon {E_0}^2 \left[\frac{a^6}{r^4}\right] \quad 4.1$$

Here $r$ is the distance that separates the centers of the two spheres. If we assume that the spheres are in close proximity, then we can approximate $r \sim a$ and we obtain the dipole-dipole force of attraction as Equation 4.2.

$$F \sim 24\pi\epsilon {E_0}^2 a^2 \quad 4.2$$

Here $\epsilon$ is the permittivity of the oil, $E_0$ is the applied electric field, $a$ is the droplet radius and $r$ is the center-to-center distance between two droplets. As shown in Equation 4.1 the force of attraction between the droplets scales with the square of applied electric field strength ($F_{dipole} \sim E^2$). If the distance between the droplets is on the order of droplet size ($a \sim r$), we can simplify equation 1 as $F_{dipole} \sim 24\pi\epsilon {E_0}^2 a^2$, which means that the force of attraction scales with the square of droplet size ($F_{dipole} \sim a^2$). Thus, for smaller droplets especially on the order of nanoscale, increasingly strong electric fields are required to induce rapid coalescence.

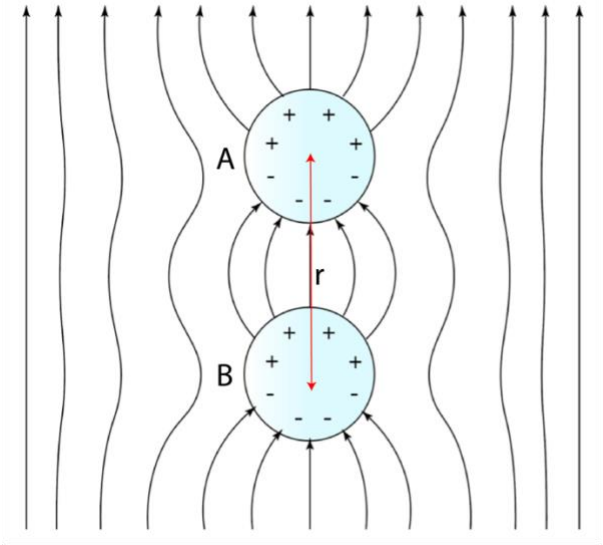

Figure 4-3. **Two conducting spheres in the vicinity of each other in a uniform applied electric field**. Both spheres get polarized due to electric field and also influence each other's polarization. The spheres experience a dipole-dipole force of attraction due to the charge distribution that results from the external electric field.

### 4.2.5. Electrocoalescer: state of the art and challenges

Traditional electrocoalescers, however, must limit their applied electric field strength for the following reasons. Many of the electrocoalescer units utilize bare metallic electrodes immersed into the emulsion. It is well understood that water droplets form long continuous chains in presence of strong electric field[146]. Therefore, often the droplet chains can grow in length and contact both electrodes simultaneously to form a highly conductive electrical pathway, causing sudden undesirable surge in current during electrocoalescer operation. This occurs because the electrical conductivity of the water droplets is 6-7 orders of magnitude higher than that of the crude oil. One way to mitigate the electrical shorting is to insulate the electrodes to avoid direct electrical contact with droplet chains. However, insulated electrodes significantly weaken the electric field in the oil because most of the applied voltage drops across the insulation. This is a consequence of the fact that the presence of surfactant compounds makes the oil non-insulating due to ion pair solvation effect[147,148] and therefore typically the electrical conductivity of crude oil ($\sigma \sim 10 - 200\ nS/m$) is 5 to 8 orders of magnitude greater than the electrical conductivity of insulators or that of pure oils ($\sigma \sim 10^{-5} - 10^{-7}\ nS/m$)[149]. As a result, even thin insulating coating results in significant voltage drop across the coating, weakening the electric field strength in the emulsion (Figure 4-4). Therefore, to ensure that all of applied voltage drops across the emulsion, most of the conventional electrocoalescers employ bare metallic electrodes. However, to reduce the likelihood of long droplet chains and electrical shorting, the electric field strength is typically limited to below ~1 kV/cm[150]. Thus, even though electrocoalescers can remove up to 70% of the water droplets that are tens to hundreds of microns in size[30], they are quite ineffective for electro-coalescence and phase separation of nanoscale droplets owing to limited electric field strength and weak dipole-dipole attraction between the droplets (Figure 4-5). The unseparated oil-water mixture is often collected and diluted with more water to be dumped into the environment. In US alone, it is estimated that nearly 15 billion barrels of micro-nano droplet contaminated wastewater is generated annually[22].

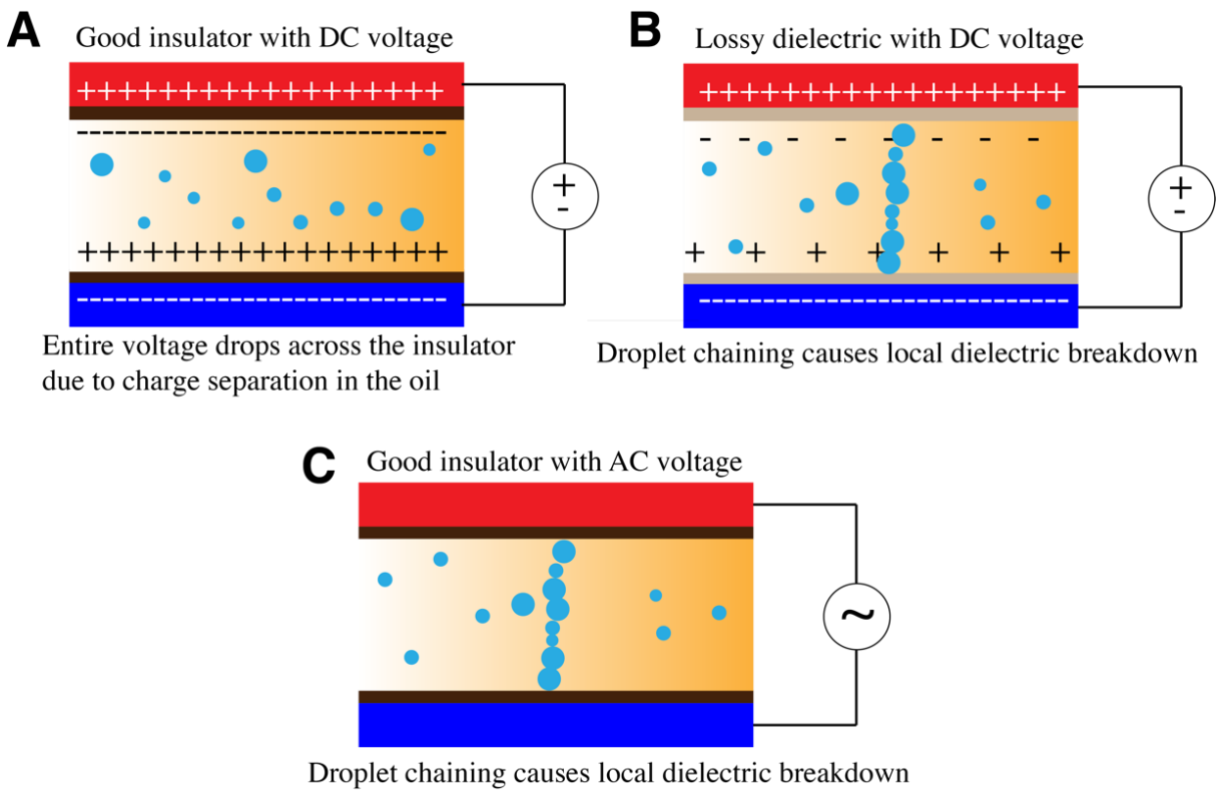


Figure 4-4. **Insulated electrodes and dielectric breakdown. (A)** The schematics shows an electrocoalescer configuration with the electrodes coated with dielectric material coated electrode. In this case the voltage division between the oil and the coating is in accordance with the relative resistance between the coating and oil. Typically, the resistance of the coating is much higher than that of the oil. This results in entire voltage to drop across the coating and negligible electric field in the oil. **(B)** Semi-conductive material (or lossy dielectrics) coated electrodes can result in some voltage drop across the oil. However, the dielectric coating on the electrode cannot prevent droplet chaining. Droplet chains can contact both electrode and result in local dielectric breakdown of the coated material. **(C)** Sometimes the electrodes can be coated with a good electrical insulator along with a DC high frequency voltage such that there is charge accumulation as shown in **(A)**. However, AC voltage does not prevent droplet chaining because dipole-dipole attraction is still present. Thus, even in this case the droplet chain can result in local dielectric breakdown.

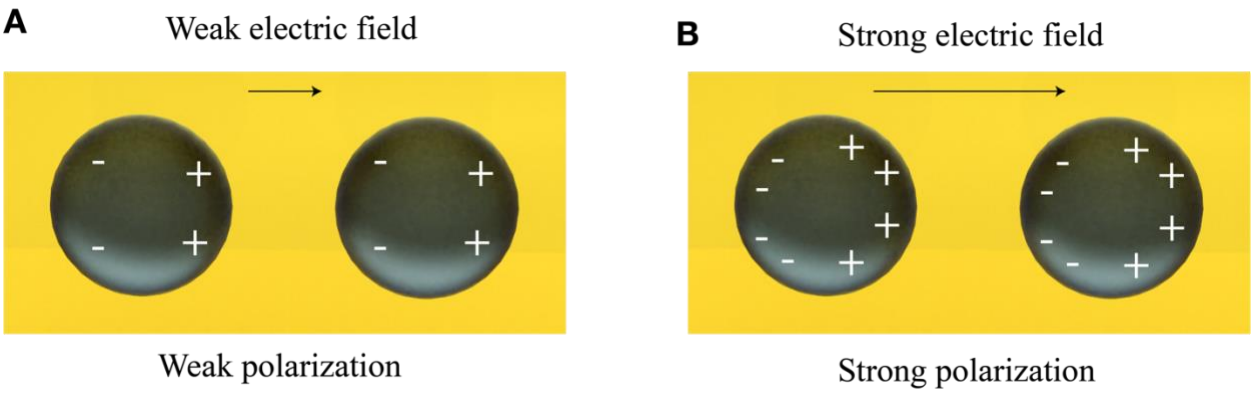


Figure 4-5. **Droplet polarization and attraction (A and B).** Even though the water droplets are electrically neutral, they can attract each other due to presence of polarization in presence of an external electric field. The schematic qualitatively shows how weak electric field results in weak polarization of the droplets and therefore weak force of attraction.

To enhance the efficiency of electrostatic oil-water separation, the water separation process is chemically aided with the mixing of demulsifiers[31,32]. Demulsifiers are compounds that destabilize water-oil interface by disrupting the surfactant film around droplets. However, many of the conventional demulsifiers are extremely toxic chemicals[33] for many fresh water and marine organisms including shrimp[34]. This is especially important in the case of offshore refineries where most of the effluents end up back in the ocean. Furthermore, the inefficiency of oil-water separation process promotes the need for a robust upstream water-washing step to dilute the salinity of the droplets that may entrain with the oil and reach downstream oil processing units. Currently, water washing in crude oil desalting process bears a large water footprint. We estimate that nearly 150 billion gallons of fresh water is being consumed worldwide for crude oil desalting purposes, which can otherwise satisfy the annual water requirements of nearly 30 million people in developing and underdeveloped regions. Crude oil desalting is also an expensive business. The current market cap of desalting industry is estimated to be at ~$2.6 billion dollars, of which demulsifier industry alone is a ~$2 billion market that exists primarily for catering to the crude oil industry.

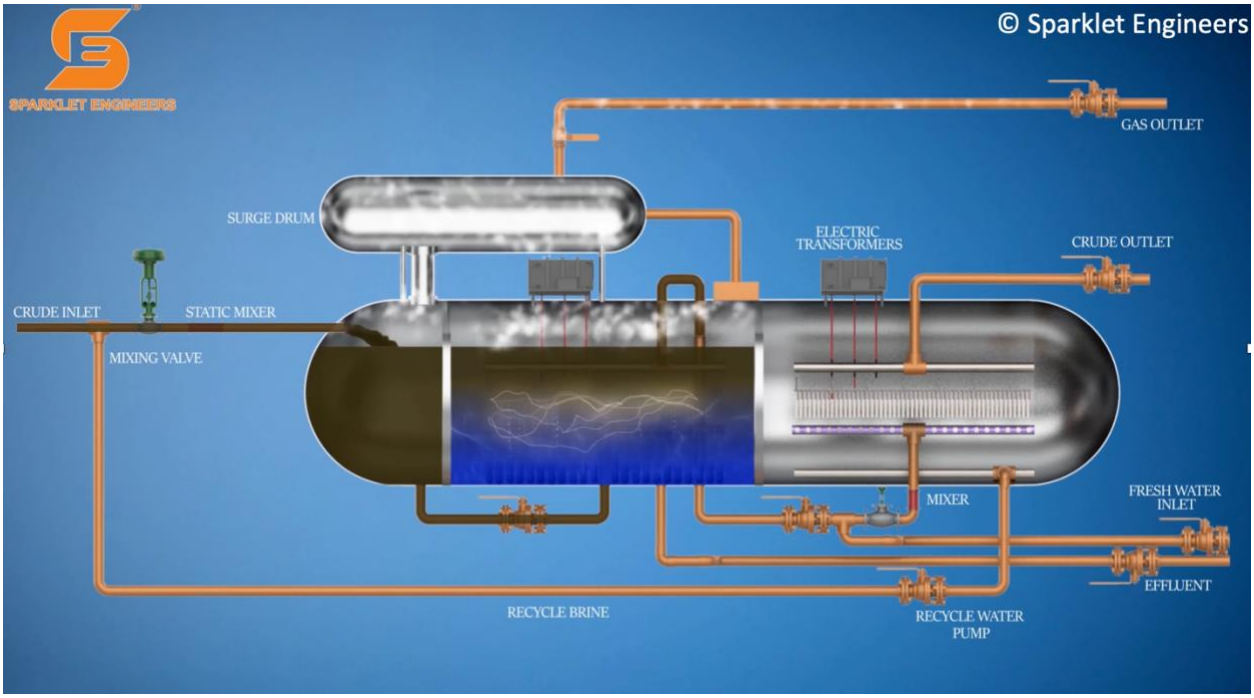


Figure 4-6. **Traditional electrocoalescer design**. Source: Sparklet Engineers ®.

### 4.2.6. Our approach

In this chapter we propose a significantly more effective electrocoalescer system for separating nanoscale water droplets from oil. Unlike traditional electrocoalescers which immerse both electrodes in the emulsion, we immerse only one of the electrodes (bottom electrode) in the oil, while the other electrode on top is placed in the air above the oil-water emulsion[151,152]. We call our proposed system as *non-Laplacian electrocoalescer* to distinguish from traditional immersed electrode electrocoalescer setup. Under low-voltage conditions, the air gap would act as a perfect insulator and the entire applied voltage would drop only across the air and therefore the electric field experienced in the emulsion would be negligible. However, in our proposed system, the electrode placed in the air has a sharp geometry (thin wire or sharp needle) such that on application of sufficiently high voltage it acts as a *space charge emitter* or *corona discharge emitter*, resulting in a non-Laplacian electric field[86,153]. Having space charge emission ensures that there is an electric field setup across the air and across the emulsion. At the same time, the air gap acts as a *physical barrier* that prevents droplet chain from contacting both electrodes simultaneously, thereby eliminating the droplet chain mediated electrical shorting. We demonstrate that via this

mechanism, we can apply much stronger (up to ~8X) electric field compared to conventional immersed electrode electrocoalescers. This results in significantly more effective phase separation of nanoscale emulsion for different water fractions ranging from 2%-20%, thus potentially eliminating the need for the use of toxic demulsifiers to ensure proper oil-water separation. By ensuring proper oil-water separation, the water washing step can also be potentially eliminated, resulting in a much more sustainable oil refinement process. We experimentally visualize droplet attraction and coalescence dynamics including formation and collapse of droplet chains in presence of strong electric field to demonstrate the dipole-dipole attraction effect. By performing a series of experiments at various voltages above the onset of corona discharge, we also demonstrate that the rate of demulsification scales with the square of applied voltage, showing that the enhanced electric field quadratically enhances the rate of electro-coalescence. Last, we design and fabricate a lab-scale practical embodiment for implementing our approach; a flow-through *non-Laplacian electrocoalescer* that enables rapid and continuous oil-water separation for nanoscale emulsion.

## 4.3. Results and Discussion

### 4.3.1. Model system

Crude oil has varying physico-chemical properties depending on the geographic location and the oil extraction process. As a result, the emulsified water fraction in the oil can vary between 1% to 20%. Therefore, to perform systematic experiments, we designed a model emulsion that mimics the physical properties of water-in-crude oil emulsion system using hexadecane as the oil, span80 as the surfactant and 0.5 M brine solution as the emulsified water in our experiments as shown in Figure 4-7A. As shown in table 1 (see Experimental Methods), our model system mimics the physical properties (density, electrical conductivity, and viscosity) of a common class of crude called light crude oil. We emulsify the water using a probe-sonicator (see Experimental Methods) that breaks up water into tiny droplets dispersed within the oil. The droplets are stabilized by span80 surfactant, and we measure the droplet size distribution using Dynamic Light Scattering (DLS) (see Experimental Methods). The average droplet size is between 150-700 nm depending on the water fraction, meaning that the dispersed water droplets in the oil form a nanoscale emulsion (Figure 4-7B). The droplet size distribution also results in a milky-white opaque

appearance due to scattering of light in all directions and the emulsion remains stable without any visible oil-water phase separation for even up-to few months depending on the water fraction.

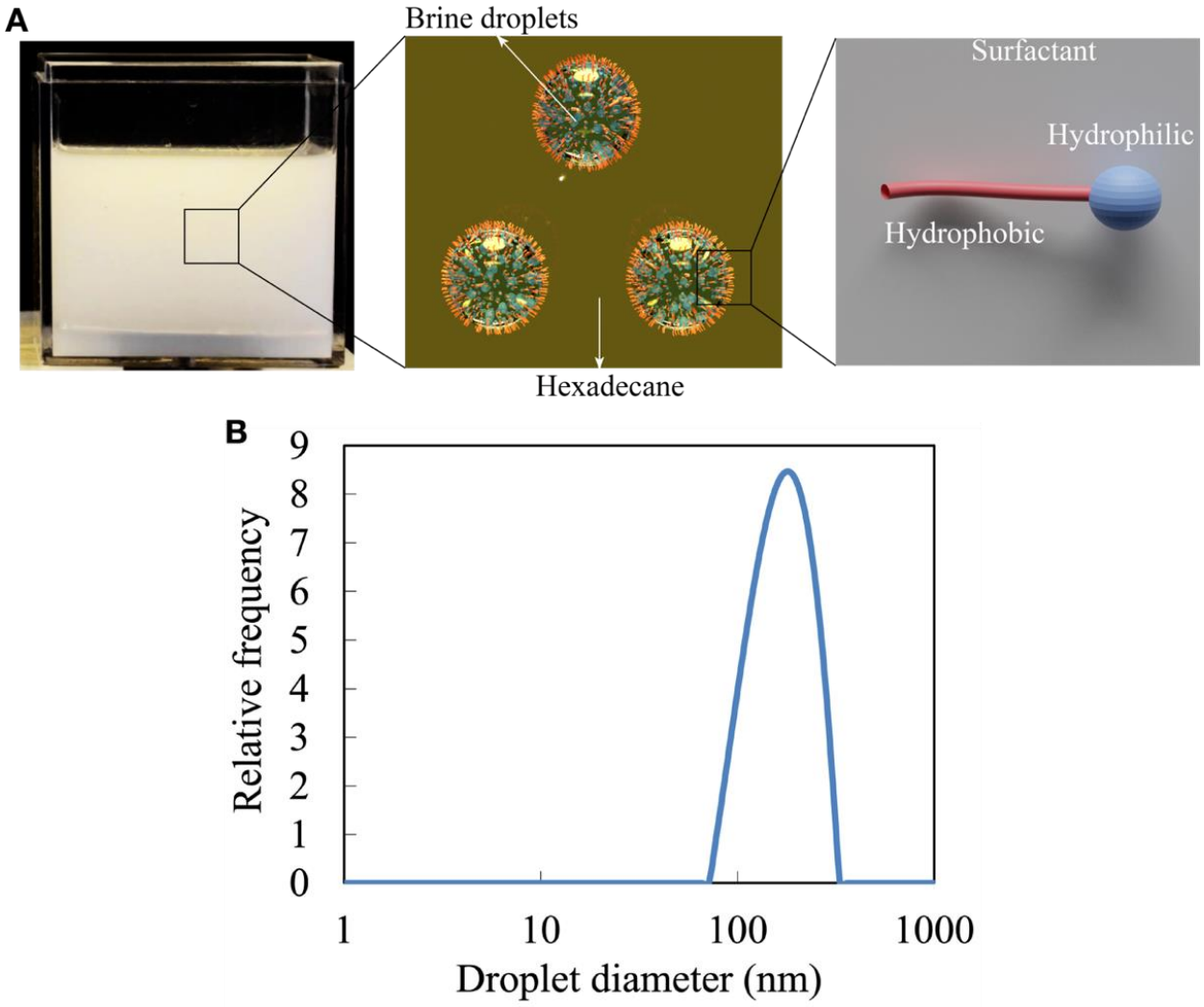


Figure 4-7. **Our model water-in-oil nanoscale emulsion. (A)** Nanoscale emulsion is prepared by probe sonication of hexadecane-water-span80 mixture. The appearance of the emulsion is milky white to due to scattering of light by nanoscale water droplets dispersed in hexadecane. Unless specified we use 0.5M brine water for preparing the emulsion. As shown in the schematic span80 provides steric hindrance for the droplets to come close to each other and coalesce, keeping the nanoscale emulsion stable without any visible phase separation for months, depending on the amount of water. **(B)** Size distribution of droplets. The mean droplet diameter is on the order of hundreds of nanometers depending on the water fraction, surfactant cut and emulsification time. Mean droplet size is estimated using Dynamic Light Scattering (DLS).

### 4.3.2. Application of stronger electric field using non-Laplacian electrocoalescer

Traditional electrocoalescer design consists of array of electrodes immersed into the emulsion[30]. The physical geometry of the electrodes vary depending on the specific requirements of the design, such as plates, mesh, honeycomb, cylinders etc[28,154]. However, the simplest unit that replicates the system of electrodes is a pair of parallel plate electrodes that apply nearly uniform electric field between them. We model the traditional electrocoalescer system of immersed electrodes using two parallel-plate electrodes (dimensions $4.5cm \times 4.5cm$) spaced apart by a few centimeters ($2 - 5cm$) immersed into a transparent cubic beaker of volume 125 ml ($5cm \times 5cm \times 5cm$) that contains the emulsion as shown in the schematic of Figure 4-10A. In contrast to this, the schematic of Figure 4-10B shows the model of our proposed system where we introduce a non-Laplacian space charge emitter electrode made of sharp geometry (thin wire or sharp needle) and an air gap between the emitter electrode and the emulsion. Since air is a nearly perfect insulator, if the applied voltage between the electrodes is below a certain threshold, the entire voltage drops across the air gap and there will be negligible electric field inside emulsion (Figure 4-8). However, when the applied voltage exceeds the threshold voltage for corona onset[155] (where air becomes ionized and there is emission of space charge from the vicinity of sharp electrode), a continuous current flow is setup between the electrodes through the emulsion resulting from a strong electric field across the emulsion.

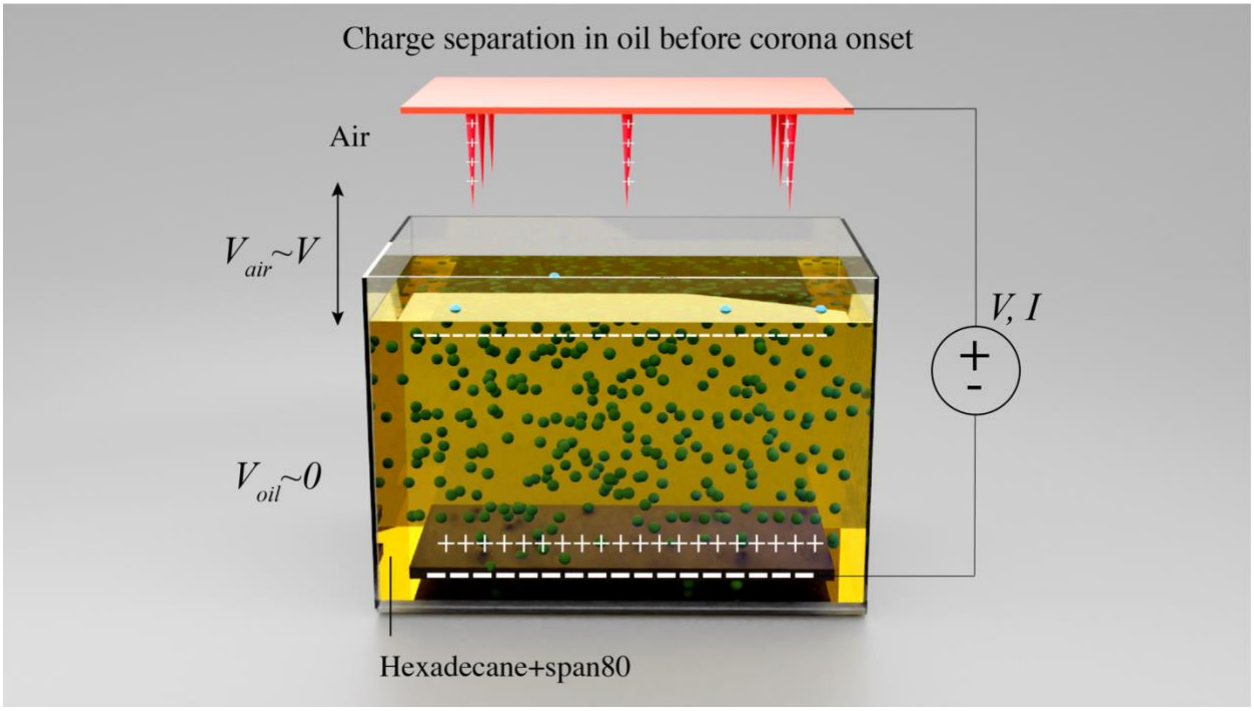


Figure 4-8. **Electric field strength in the oil before the onset of corona discharge.** Since air acts as a perfect insulator in comparison to hexadexane-span80 mixture before the onset of corona discharge, the entire applied voltage drops across the air at voltage below corona onset voltage. This is also manifested as a zero current flow through the oil.

We apply a voltage $V$ across the gap $d$ between the electrodes. In the case of parallel plate electrodes, since the entire applied voltage drops across the oil and since the electrode geometry is like a capacitor, the electric field ($E$) in the emulsion is well estimated as $V/d$. However, in the case of non-Laplacian electrocoalescer setup, it is challenging to predict the exact voltage drop across the oil due to the presence of air gap. Moreover, the electric field lines are non-uniform due to the sharp geometry of the top electrode, resulting in a non-uniform field strength in the oil. To simplify our model and to estimate the average electric field strength in the oil, we performed experiments using hexadecane-span80 mixture where we applied different voltages across the emitter and bottom electrodes and measured the resulting current flow through the oil as shown in the schematic of Figure 4-9A. The current flow is a result of enhanced conductivity of the oil due to the addition of the surfactant span80 that causes ion-pair solvation effect in the oil[147,156–158]. In the absence of span80 there is no current flow through the oil. The average electric field in the oil can be estimated as $E \sim \frac{J}{\sigma}$ where $J$ is the current density (obtained by dividing the current flow with

area of the bottom electrode) and $\sigma$ is the conductivity of the hexadecane-span80 mixture obtained from literature[86,156]. It should be noted that we do not introduce water droplets in these experiments because span80-hexadecane mixture is what contributes to the current flow through the emulsion and not the dispersed water droplets. In Figure 4-9B we plot $\frac{J}{\sigma}$ against the quantity $\frac{V}{d}$. It can be seen that there is a linear correlation between $\frac{J}{\sigma}$ and $\frac{V}{d}$ at voltages high enough to induce space charge injection. This means that similar to the immersed parallel-plate configuration, we can approximate the average electric field in the oil in the case of non-Laplacian electrocoalescer setup as $E \sim \frac{J}{\sigma} \sim \frac{V}{d}$.

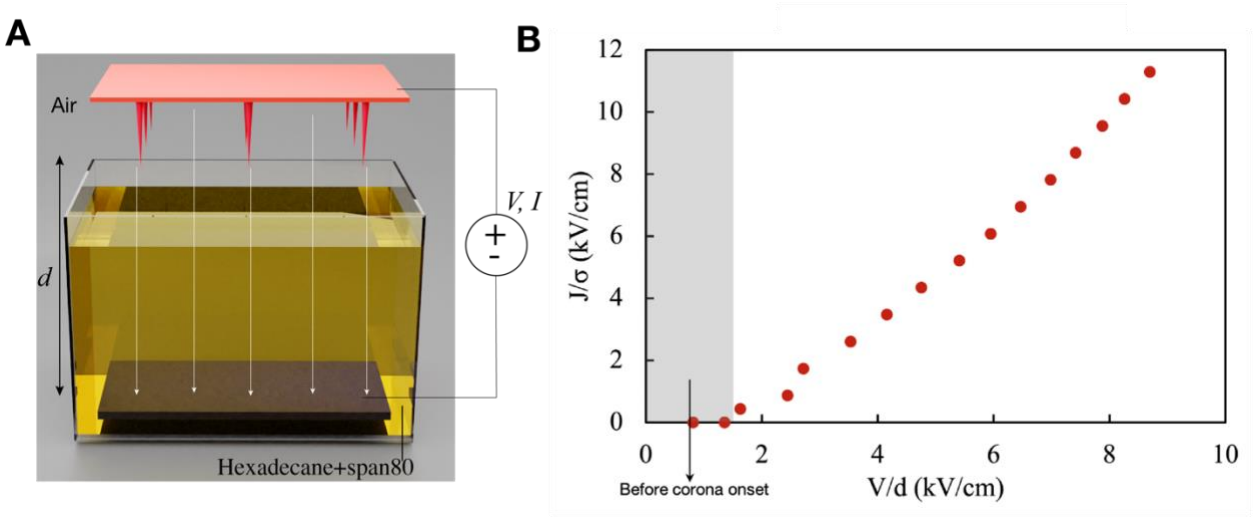


Figure 4-9. ***V/d* as a proxy for electric field in the oil. (A)** Experimental setup for applying corona discharge in oil and measuring the current that corresponds to the applied voltage. **(B)** Plot of $J/\sigma$ against *V/d* showing the linear correlation between both parameters. The linear correlation has a slope close to 1; indicating that *V/d* is a fair approximation of the average electric field strength in the oil.

For performing experiments where we apply electric field across the emulsion, we prepared water-in-oil emulsion consisting of 20% 0.5 M water in hexadecane with 1% span80 as the surfactant (see Experimental Methods). The average droplet diameter is ~500 nm as measured using Dynamic Light Scattering (DLS). For the non-Laplacian electrocoalescer setup, we use an array of 5 steel needles (tip diameter ~60 microns) spaced at 2.5cm apart as the top electrode and a bare metallic plate as the bottom electrode. In the parallel plate electrode setup, when both plates (non-insulated bare metallic electrodes) are immersed in the emulsion as shown in Figure 4-10A

(with a gap *d*~3.5cm), as the applied voltage increases, the current flow through the emulsion also increases. In Figure 4-10C, we plot the measured current vs applied *V/d*. It can be seen that in this setup that mimics the conventional immersed electrode electrocoalescer, the current suddenly spikes up by more than 1000x when *V/d* reaches approximately 1 kV/cm. This means that the maximum electric field strength (*V/d)* that can be safely applied without introducing electrical shorting is below ~1 kV/cm in our model conventional electrocoalescer design.

We varied the distance between the electrodes from 2-5 cm and find that the critical electric field for shorting is in the range of 0.9-1.1 kV/cm. In Figure 4-10C we also plot the measured current vs *V/d* for our proposed non-Laplacian electrocoalescer setup. In contrast to the immersed electrode setup, even at an average electric field strength as high as ~8 kV/cm there is no current surge or electrical shorting in the non-Laplacian electrocoalescer setup. This means that we can apply nearly 8 times stronger electric field strength using non-Laplacian electrocoalescer system for the case of 20% water-in-oil nanoscale emulsion. Beyond 8 kV/cm, we observed vigorous electrohydrodynamic flow[159–161] (as demonstrated in Figure 4-11), and sporadic onset of electrical arcing in the air due to the local electric field strength near the sharp electrode reaching the breakdown field strength of air. Therefore, we safely limited the maximum applied *V/d* to ~7.5 kV/cm.

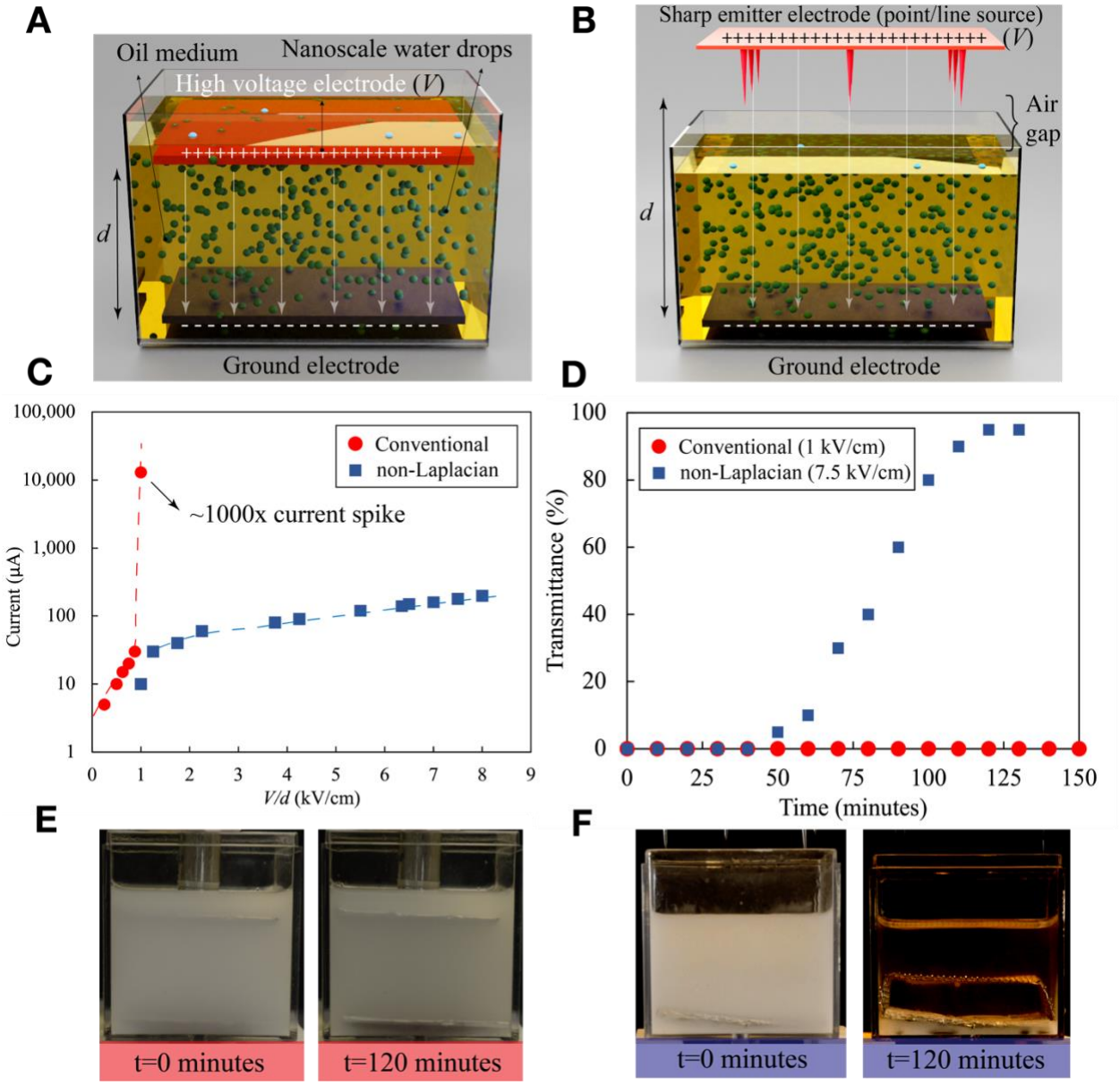


Figure 4-10. **Non-Laplacian electrocoalescer setup enables application of much stronger electric field and therefore faster phase separation of water-in-oil nanoscale emulsion. (A)** Schematic showing conventional electrocoalescer system with immersed electrodes in water-in-oil emulsion. **(B)** Our proposed non-Laplacian electrocoalescer setup that makes use of space charge injecting emitter electrodes to setup strong electric field across the emulsion. **(C)** Plot of current vs normalized voltage (average electric field) in conventional vs non-Laplacian electrocoalescer system for a 20% w/o emulsion. The maximum electric field is limited to ~1 kV/cm before current spikes in the case of immersed electrodes. On the other hand, with non-Laplacian electrocoalescers up to ~8 kV/cm can be applied with no current spike. **(D)** Transmittance of emulsion as a function of time under applied electric field. Presence of stronger field enables effective phase separation of oil and water phases which is not possible using

conventional immersed electrode setup with limited electric field strength. The transmittance is normalized by the transmittance of pure hexadecane and 1% span80 solution. **(E)** Images of emulsion before and after application of electric field using immersed electrodes. Due to weak electric field (E~1 kV/cm), there is virtually no phase separation. **(F)** Images of successful demulsification of 20% water-in-oil emulsion after ~120 minutes of application of strong electric field (~7.5 kV/cm).

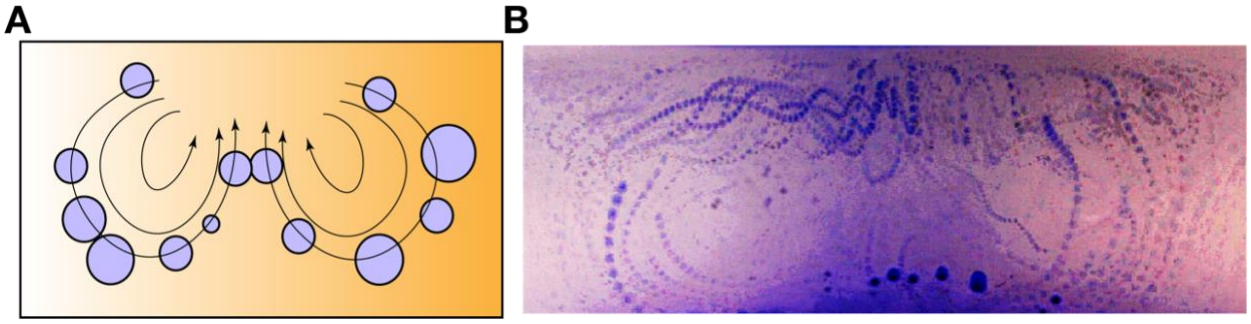


Figure 4-11. **Electrical conductivity of the oil and resultant electrohydrodynamic flow. (A)** Adding oil soluble surfactants results in the solvation of ion pairs and enhances the electrical conductivity of the oil. A gradient in the applied field also causes a gradient in electrical conductivity within the oil. This causes electrohydrodynamic flow of the oil and small water droplets keep circulating with the oil. **(B)** Time-lapse image of dyed water droplets circulating in the oil under applied electric field.

To compare and quantify the rate of demulsification in the immersed electrode setup vs the non-Laplacian electrocoalescer configuration, we performed experiments that were more than hour-long where we applied the maximum possible electric field strength for up to ~120 minutes across the emulsion. It must be noted that in the case of immersed electrode configuration the limit is ~1 kV/cm and in the case of non-Laplacian electrocoalescer configuration it is ~7.5 kV/cm. We kept the applied voltage steady and measured the relative transmittance (transmittance of emulsion normalized by the transmittance of pure hexadecane-1% span80 mixture) of the emulsion over time as shown in Figure 4-10D. Since the non-Laplacian electrocoalescer configuration enables application of much stronger electric field without electrical shorting, the emulsion turned from milky white to nearly transparent as shown in Figure 4-10F (see Movie 4-2), resulting in saturation of relative transmittance to >95% as shown in Figure 4-10D. The transition of the emulsion from milky white to transparent is the consequence of electro-coalescence and settling down of water droplets at the bottom due to higher density compared to hexadecane. In contrast, for the immersed electrodes where electric field strength is limited, the relative transmittance of the emulsion

remains at almost 0%, and the emulsion remains milky white even after 120 minutes of application of electric field as shown in Figure 4-10E (see Movie 4-1).

### 4.3.3. Effect of water fraction on the limiting field strength for traditional electrocoalescers

Since water droplet chains are the reason for the occurrence of electrical shorting in traditional electrocoalescers, the applied electric field limit depends on the amount of water present in the oil. At 0% water fraction where the medium is just pure oil, there will be no electrical shorting even at very high electric field unless the oil breaks down. On the other hand, at 100% water fraction where the medium is water, there will be immediate electrical shorting even at very low voltage. Therefore, for systematically studying the electrical shorting behavior of nanoscale emulsion, we performed experiments using immersed electrodes at various water fractions.

First, we performed qualitative experiments to visually demonstrate the electrical shorting phenomenon and its consequences. We prepared micro-emulsion (for visualizing the droplets) consisting of relatively larger droplets of water (initial size in the range of ~1-50 microns) and water fraction 5% such that the emulsion is translucent. Figure 4-12A demonstrates the outcome of the application of electric field (~2 kV/cm) using immersed needle electrode, where droplets form chains to provide a continuous electrical pathway, and result in arcing that appears as a bright glow. We performed several qualitative experiments using immersed needles, immersed wires and immersed plate electrodes and observed that electrical shorting happens regardless of the electrode geometry as long as both electrodes are immersed in the emulsion. We visualized the droplet chain formation resulting from the electric field application using high speed, high magnification imaging (see Experimental Methods) as shown in the magnified inset of Figure 4-12A. The inset shows one of the droplet chains where water droplets of different sizes (ranging from 2 to 70 microns) align due to dipole-dipole force of attraction.

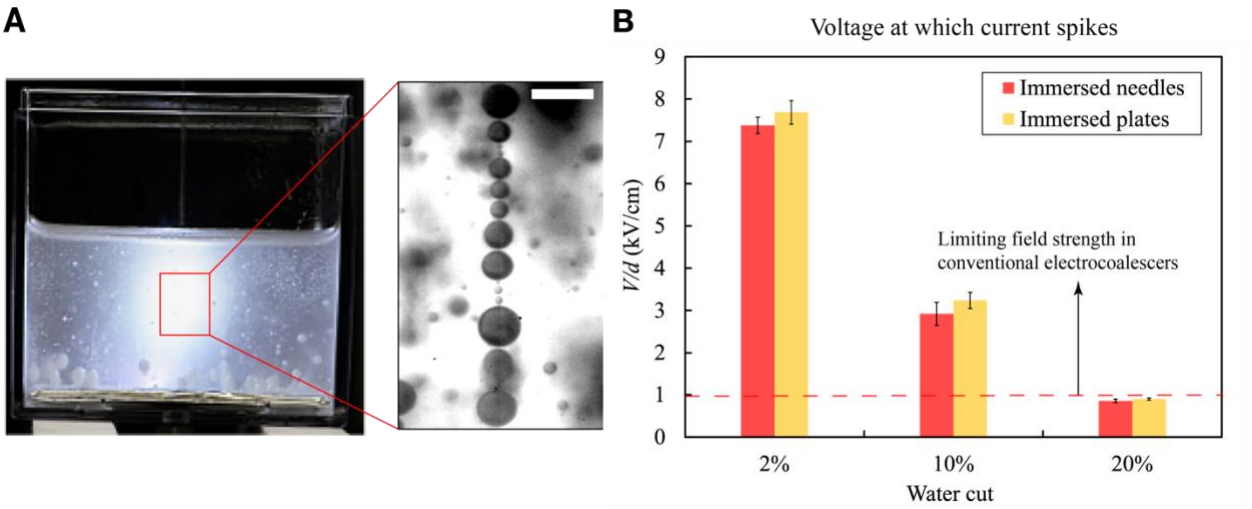


Figure 4-12. **Current spike and electrical arc in conventional electrocoalescers are due to formation of water droplet chains that result in conductive pathway between the electrodes. (A)** Electrical shorting between two immersed electrodes in water-in-oil emulsion (top needle and bottom plate). Zoomed in image in the expanded inset shows a representative image showing the formation of long continuous chain of water droplets that can create a conductive pathway between electrodes. Scalebar is 100 $\mu m$. **(B)** The propensity for arcing due to chaining increases with an increase in water fraction. In conventional industrial electrocoalescers, the applied electric field is limited such that $E$<1 kV/cm, to ensure electrical arcing-free operation at all water fractions.

Next, we systematically investigate the effect of water fraction on the electrical shorting characteristics of nanoscale emulsion. We performed experiments at water fractions of 2%, 10% and 20% (with 1% span80 in hexadecane as the continuous medium). We limit our study at a maximum of 20% water fraction because typically, light crude oil emulsions with highest amount of water have around 20% water fraction in emulsified form. Since the water droplets are nanoscale, the emulsion is milky white (nearly opaque) and therefore the electrical arc is hard to visualize in this case. However, the electrical shorting is manifested in current measurements, using which we identify the critical voltage and electric field at the onset of arcing as previously described in Figure 4-10C.

Figure 4-12B shows the critical shorting electric field for immersed electrodes at different water fractions. To generalize our results, we performed experiments using immersed needle and immersed plate configurations at 3 different electrode spacings from 3-5cm. As expected, we find that the maximum electric field that can be safely applied without shorting the electrodes depends on the amount of water present in the oil. At 20% water fraction, shorting happens at ~1 kV/cm

similar to what is previously demonstrated in Figure 4-10C. However, as water fraction reduces to 2%, the critical voltage can be as high as 7.5-8 kV/cm.

This observation suggests that for all water fractions below 20%, electrical shorting can be avoided altogether if the applied voltage is less than ~1 kV/cm when both electrodes are immersed in the oil. Since the amount of water in crude oil fluctuates, traditional electrocoalescers are designed to handle the worst-case scenario of 20% water fraction. Thus, for safe and effective operation of electrocoalescers, the applied voltage between the electrodes, regardless of the geometry, is typically limited to the range of 0.1-1 kV/cm[150].

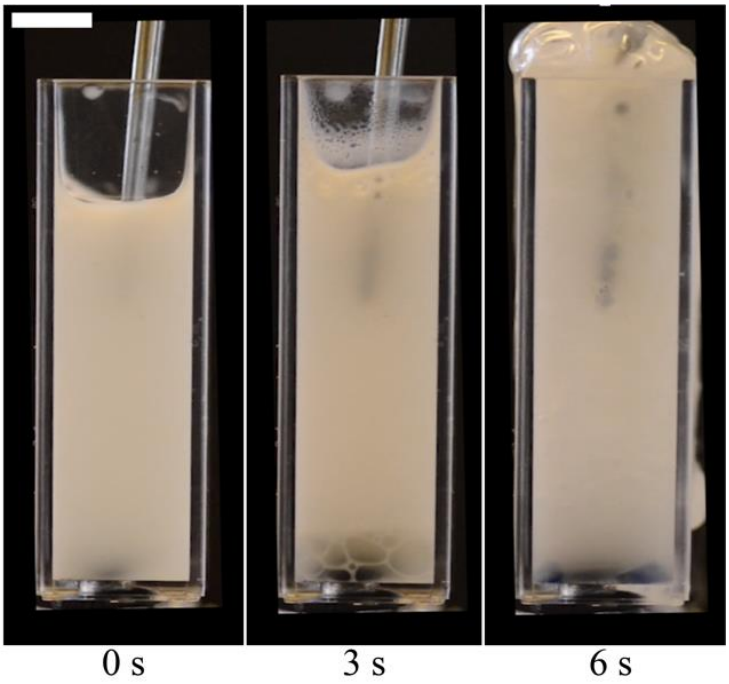


Figure 4-13. **Demonstration of electrolysis due to electrode shorting.** Droplet chains form a continuous electrical contact between the two immersed electrodes. The series of images show electrolysis of water and emulsion spillage due to gas evolution resulting from current flow through water droplets. Scale bar is 0.5 cm.

Apart from the potential damage to the electrical circuitry and other expensive equipment, electrical shorting also introduces several other challenges. Increased local current flow due to electrical shorting can render electrocoalescence ineffective in the remaining volume of the emulsion, resulting in saline water droplets entraining with the oil flow and reaching downstream oil processing units. Electrical shorting via droplet chains can also result in electrolysis of water

due to current flow, resulting in undesirable trapped gases in the oil. In Figure 4-13 we demonstrate the application of voltage using immersed electrode in a 10% emulsion and the resultant evolution of gas bubbles due to electrolysis (see Movie 4-4). In industrial electrocoalescers where the entire system is enclosed and not open to air, gas bubbles get trapped in the oil, acting as a physical insulating barrier between electrode and oil. This can further weaken the electric field in the emulsion and drastically reduce the efficacy of electrocoalescer.

### 4.3.4. Effect of water fraction in non-Laplacian electrocoalescer

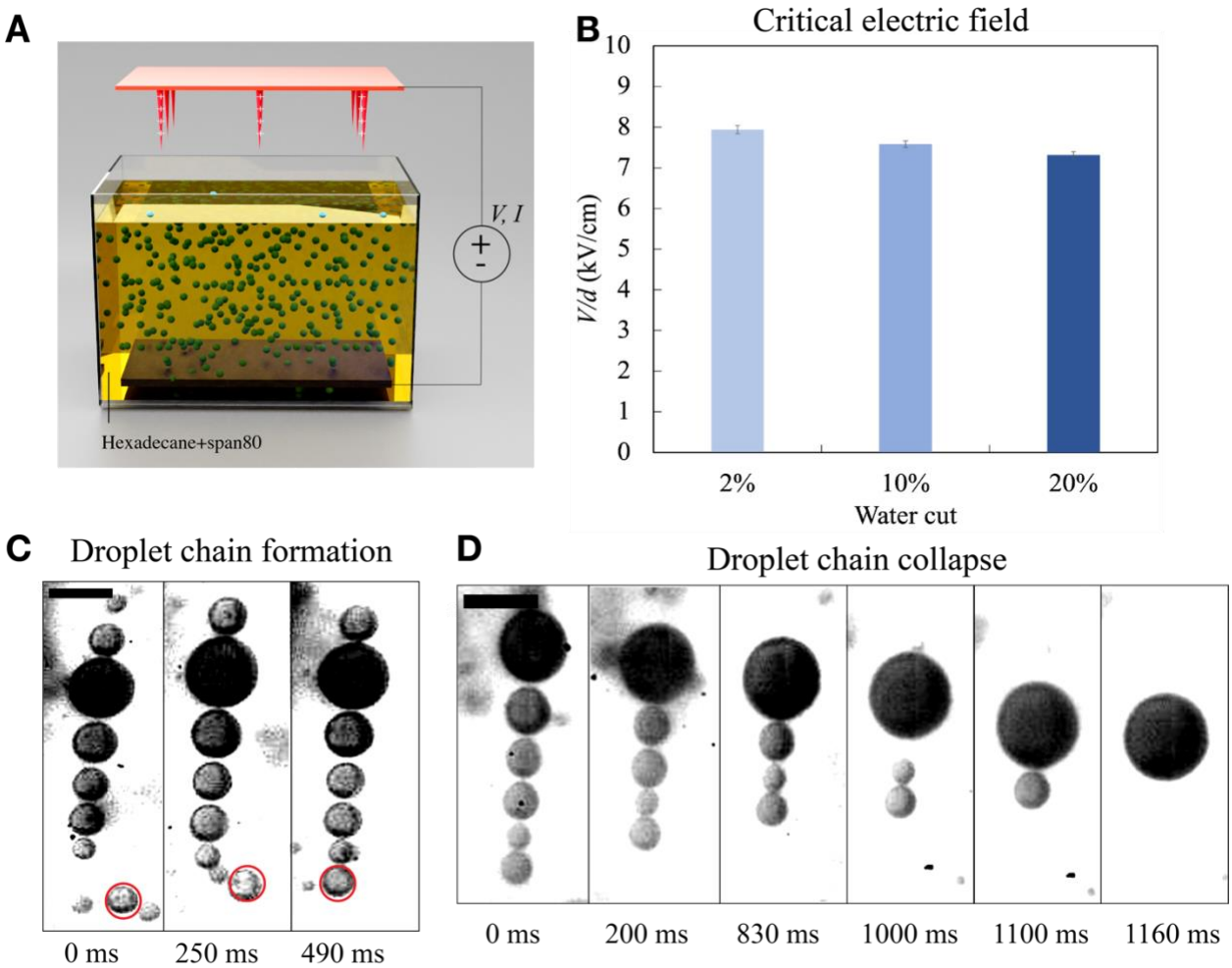


Figure 4-14. **Demonstration of chaining events in emulsion on application of electric field using the non-Laplacian electrocoalescer setup. (A)** Schematic of the experimental setup. **(B)** The maximum voltage (normalized by the distance) that can be applied in a space charge injection setup is much higher compared to an immersed electrode setup. The critical field strength is agnostic to the water fraction in the range of 2-20% water, which means that the present method overcomes the *V/d* limit of traditional electrocoalescers, which is close to ~1 kV/cm. **(C)**

Visualization of droplet chain formation using high magnification, high-speed imaging. The series of images show how a new droplet gets attracted to the chain via dipole-dipole attraction to increase the length of the chain. **(D)** Visualization of chain collapse and droplet coalescence. The series of images show how a multi-droplet chain coalesces into a single large droplet. Scale bar is 50 $\mu m$.

As shown in Figure 4-12, droplet chaining is governed by the applied electric field strength and not by the electrode geometry. Therefore, chaining of droplets is unavoidable even in the case of non-Laplacian electrocoalescer setup. However, the presence of air gap between the top electrode and the emulsion as shown in Figure 4-10B acts as a physical barrier, preventing direct electrical path formation between the electrodes. For systematically designing a non-Laplacian electrocoalescer based electrocoalescer setup that is agnostic to water fraction, we must understand the limits of the applied electric field strength as a function of the amount of water present. For investigating effect of water fraction, we performed experiments 2%, 10% and 20% water using the non-Laplacian electrocoalescer configuration as shown in Figure 4-14A.

The applied voltage between the electrodes was increased to a point where the emitter electrode starts to sporadically cause electrical arcing in the air. We measured the applied voltage and normalized it by the gap between the electrodes to estimate the electric field strength. Figure 4-14B plots the limiting field strength as the maximum possible *V/d* that can be applied before observing arcing in air at 3 different water fractions. It can be seen that the maximum electric field strength is almost independent of the water fraction. Unlike immersed electrode case where *V/d* was limited to ~1 kV/cm in the case of 20% water fraction, we can safely apply between 7-8 kV/cm using non-Laplacian electrocoalescer setup even when the water fraction is as high as 20%. This finding opens a completely new pathway for faster electrocoalescence of nanoscale droplets, and thereby efficient oil-water separation without using demulsifiers, which is impossible in a conventional electrocoalescer design.

We further probe into the dynamics of droplets by observing droplet behavior as voltage is being applied, using high-speed, high-magnification imaging (see Experimental Methods). Since dynamic imaging of nano-scale droplets under high voltage is very challenging, we observed the dynamics of micron-scale droplets (see Experimental Methods).

Figure 4-14C shows a droplet chain formation event in the non-Laplacian electrocoalescer setup ($E$~5 kV/cm) as a series of images (see Movie 4-5). Here, an individual droplet forms part of the already formed droplet chain due to dipole-dipole attraction, thus elongating the length of the chain in the process. Similar to the formation of chains due to dipole-dipole attraction, chains can also undergo sudden collapse due to the same force of electrostatic attraction that pressurizes the thin oil film between two droplets to drain out[162]. Figure 4-14D, in a series of images, shows the collapse of the same droplet chain shown in Figure 4-14C, which demonstrates the dynamic nature of droplet-droplet interaction (see Movie 4-6, Movie 4-7). Overall, the droplet chain formation and collapse are difficult to model processes because of the complexity of the system. As a result, there could be a wide distribution in the size of droplet chains within the emulsion at a given point of time. However, in general, the propensity for formation of longer chains increases as the electric field strength is increased. This experiment also confirms that by incorporating the non-Laplacian electrocoalescer configuration, we are not eliminating droplet chain formation. Instead, we are preventing the electrical shorting by not providing a continuous pathway for the droplets to let current flow between the electrodes.

We also image the dynamics of water droplets in the bulk volume by performing experiments with blue dyed droplets and observing their size evolution with time (Figure 4-15). To enable droplet visualization, we start with a 5% microemulsion of average droplet size ~5 microns. On application of electric field (~5 kV/cm) via the non-Laplacian electrocoalescer configuration, we observe the bulk droplet size evolution with time. Figure 4-15 shows the evolution of droplet size against time. Before the application of voltage, there are large number of small micron-scale droplets in the oil. However, as the electric field is applied, droplets continuously coalesce and grow in size to form small number of large millimetric droplets that eventually gravity separate (see Movie 4-8). This observation shows that regardless of the randomness of chain formation and collapse, overall, the droplets undergo coalescence in the bulk volume before undergoing density separation.

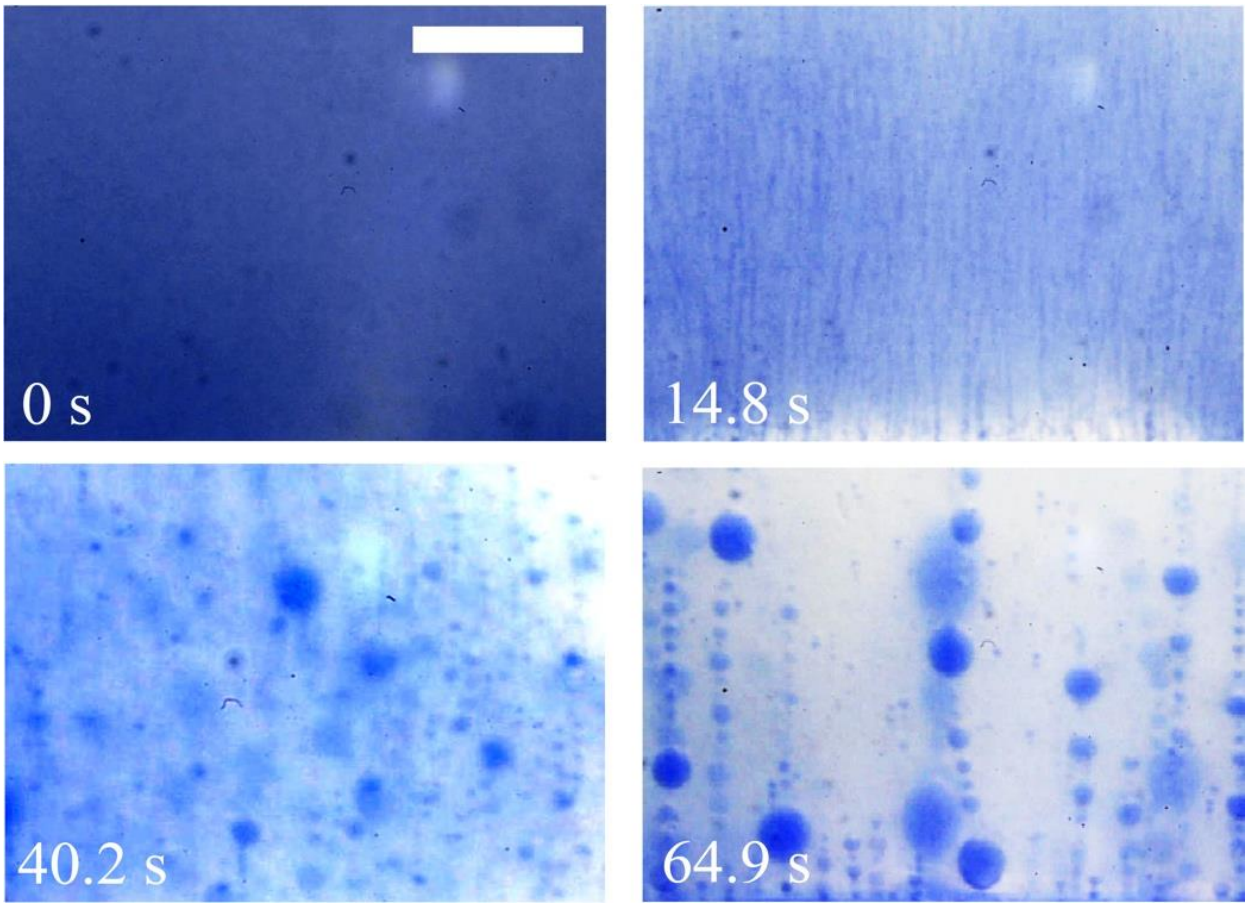

Figure 4-15. **Coalescence of water droplets in the bulk volume of the emulsion.** Evolution of water droplets is visualized using droplets dyed with blue food dye. In this experiment the initial droplet size was ~10 $\mu m$ to aid the visualization of droplet size evolution since it is extremely hard to visualize the size evolution of nanoscale droplets. Before the application of voltage, there are large number of small droplets on the order of 10 $\mu m$ in size. As time progress, droplets in the bulk undergoes coalescence to form large droplets on the order of 500 $\mu m$. Scale bar is 1 mm. Applied electric field is ~ 6 kV/cm.

### 4.3.5. Quantifying the rate of oil-water separation

As demonstrated in Figure 4-10, the rate of phase separation is dependent on the electric field strength. For nanoscale droplets, higher electric field strength is favorable for faster demulsification. In addition, since demulsification is dependent on the coalescence and settling down of water droplets, the rate of demulsification will also depend on the amount of water initially present in the oil. Systematic design of a non-Laplacian electrocoalescer setup therefore requires quantification of demulsification rates as a function of applied voltage and water fraction. For

quantifying the of rate of demulsification, we performed two sets of experiments: (1) varying the voltage by keeping water fraction constant and (2) varying the water fraction by keeping applied voltage constant.

First, for quantifying the effect of voltage, we prepared 2% emulsion of water in hexadecane (mean size ~200 nm) and observed the evolution of transmittance of the emulsion with time while applying the voltage. We define demulsification time as the time when the normalized transmittance (with respect to pure hexadecane-1% span80 mixture) of the emulsion saturates above 95%. Since sampling the emulsion from the experimental beaker frequently to perform transmittance measurement using DLS interrupts the experiment, we define a proxy for transmittance using the visible emulsion color in the images (RGB values) (see Experimental Methods). Based on the proxy transmittance (Figure 4-16), we quantify the time taken for demulsification when the normalized emulsion color value saturates to 0.95.

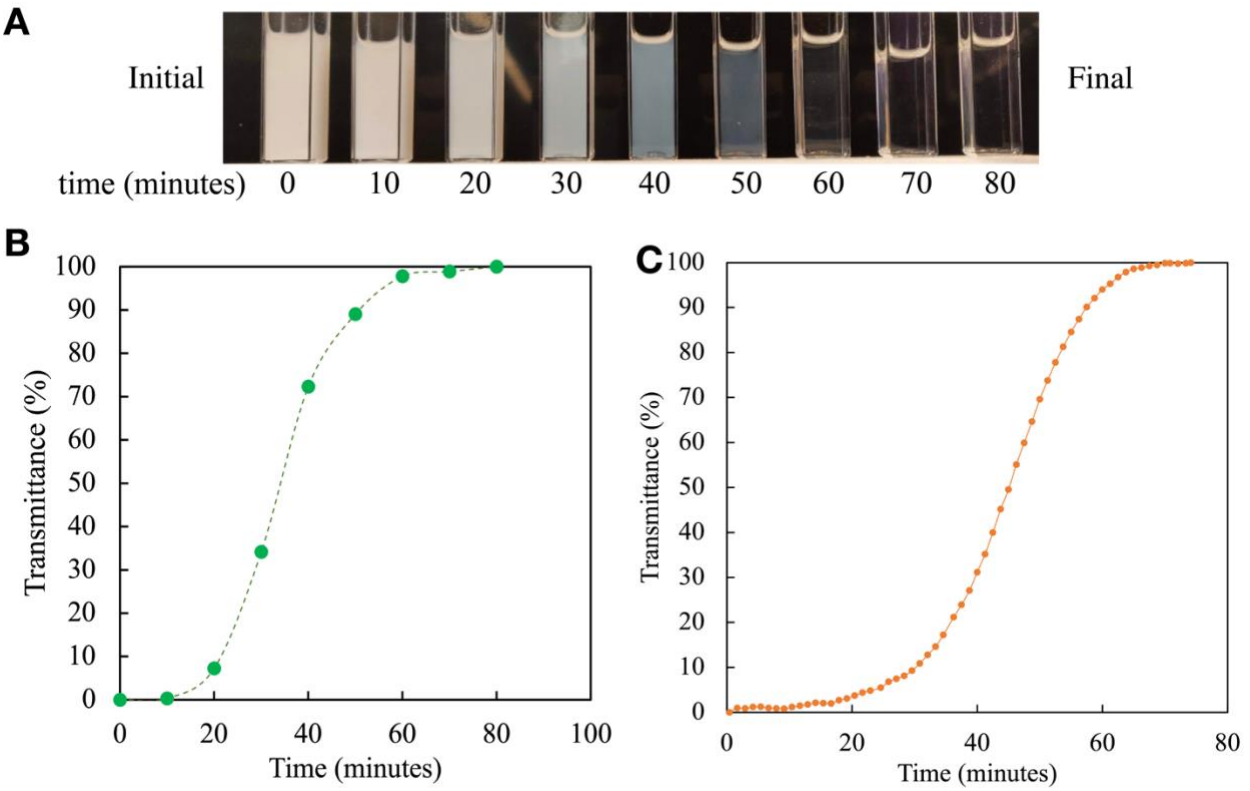


Figure 4-16. **Defining rate of demulsification. (A)** Series of images of emulsion sampled from demulsification setup showing how the emulsion transforms from milky white to almost transparent after separating oil and water. **(B)** Transmittance value of emulsion normalized against the transmittance of pure hexadecane-span80 mixture. Transmittance is measured using DLS

instrument. **(C)** A proxy for transmittance can be obtained by mapping the average color of the emulsion (white in the beginning to the dark color of the background in the end). It can be seen that both DLS transmittance and normalized color value saturates at ~60 minutes showing how to estimate time taken for phase separation of oil and water. We used 10% water-in-oil emulsion for this experiment.

In Figure 4-17A, we plot the rate of demulsification as a function of applied voltage. At voltages below the onset of corona discharge, the entire applied voltage drops across the air and therefore there is negligible electric field across the emulsion. Hence, the emulsion remained stable even after the application of voltage for ~110 minutes. Above the corona onset voltage, as the voltage is increased the rate of demulsification also increases. We plot the demulsification time against applied voltage and the data points collapse on to a curve that scales as $t \sim V^{-1.95}$ as denoted in Figure 4-17A. As previously shown in equation 1, the force of attraction scales with the square of electric field strength ($F_{dipole} \sim E^2 \sim V^2$). Therefore, the droplet-droplet force of attraction increases quadratically with applied voltage. Since the rate of demulsification is proportional to rate of coalescence, the time taken for demulsification ($\tau$) goes approximately with the inverse of square of the applied voltage ($\tau \sim V^{-2}$) as demonstrated in Figure 4-17A. This observation hints to the fact that electrostatic phase separation using non-Laplacian space charge emitter setup is governed by the coalescence of the droplets due to dipole-dipole force of attraction.

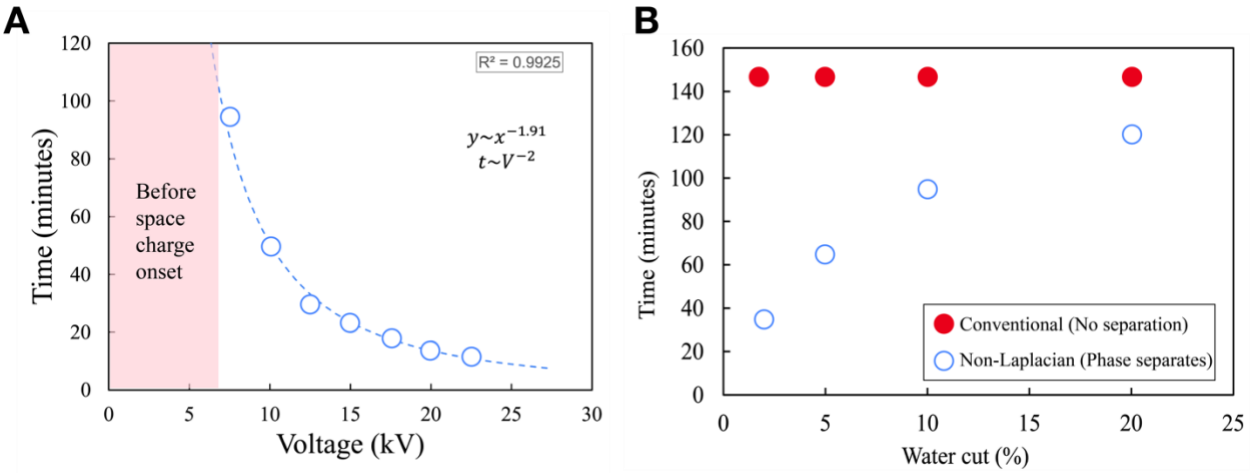


Figure 4-17. **Rate of demulsification at different voltages and different water fractions. (A)** Rate of demulsification as a function of applied voltage (or electric field strength). In this experiment we prepared 2% emulsion of water-in-oil with 1% span80 of mean droplet size ~200 nm. At low voltages before the onset of corona discharge, the emulsion remains visually stable and milky even after 110 minutes of application of voltage. **(B)** Demulsification time as a function

of water fraction (0.5M brine solution in 1%span80 and hexadecane). Blue circular markers show that demulsification takes longer with increasing water fraction. Applied electric field strength is ~7.5 kV/cm. It is almost impossible to demulsify water-in-oil nanoscale emulsion regardless of the water fraction using conventional immersed electrode setup that limits electric field strength to ~1 kV/cm. Red square markers show the emulsion remains stable with no sign of oil-water separation even after 145 minutes of application of voltage.

Since droplet approach and coalescence are stochastic, we expect that the time taken for all or most droplets in the emulsion to undergo coalescence increases with increase in number of droplets. Since the number of droplets is proportional to the water fraction for a given droplet size, the water fraction will have significant effect on the rate of demulsification. To investigate the effect of water fraction on rate of oil-water separation, we performed a series of experiments for observing the time taken for demulsification at different water fractions ranging from 2%-20%. To compare the efficacy of our non-Laplacian electrocoalescer configuration against conventional electrocoalescence systems, we also performed experiments using immersed parallel plate electrodes by limiting the applied electric field strength to 1 kV/cm. In contrast, for non-Laplacian electrocoalescer configuration, we applied a constant electric field strength of ~7.5 kV/cm regardless of the water fraction as we found from Figure 4-14C. We plot the results in Figure 4-17B. It can be seen that in the non-Laplacian electrocoalescer configuration, the time taken for demulsification increases with water fraction. However, the electrocoalescence was much effective compared to the immersed electrode system where no visible demulsification was observed even after application of electric field for >145 minutes. The emulsion remained milky white throughout the experiments.

In a traditional oil-water separation system, despite the use of chemical demulsifiers, the total residence time of the emulsion in the series of separation tanks that employ immersed electrode electrocoalescers vary vastly from few minutes to ~60 minutes, depending on the operating conditions and emulsion characteristics. Our experiments demonstrate that depending on the water fraction, the non-Laplacian electrocoalescer system can achieve similar or much faster rate of oil-water separation from nano-scale emulsion while completely eliminating the use of chemical

demulsifiers. This finding mitigates one of biggest environmental concerns associated with oil refinery effluents.

### 4.3.6. Practical embodiment: Flow-through non-Laplacian electrocoalescer

Last, we develop a lab-scale practical embodiment of the proposed non-Laplacian electrocoalescer system that incorporates continuous flow (see Experimental Methods). For this, we designed and fabricated an emitter electrode array-based oil-water separation chamber that consists of a flat bottom electrode on which the emulsion flows, and an array of thin wires that act as space charge emitter electrodes on the top. The emulsion flows from a full container to an empty container due to gravity as shown in the schematic of Figure 4-18A.

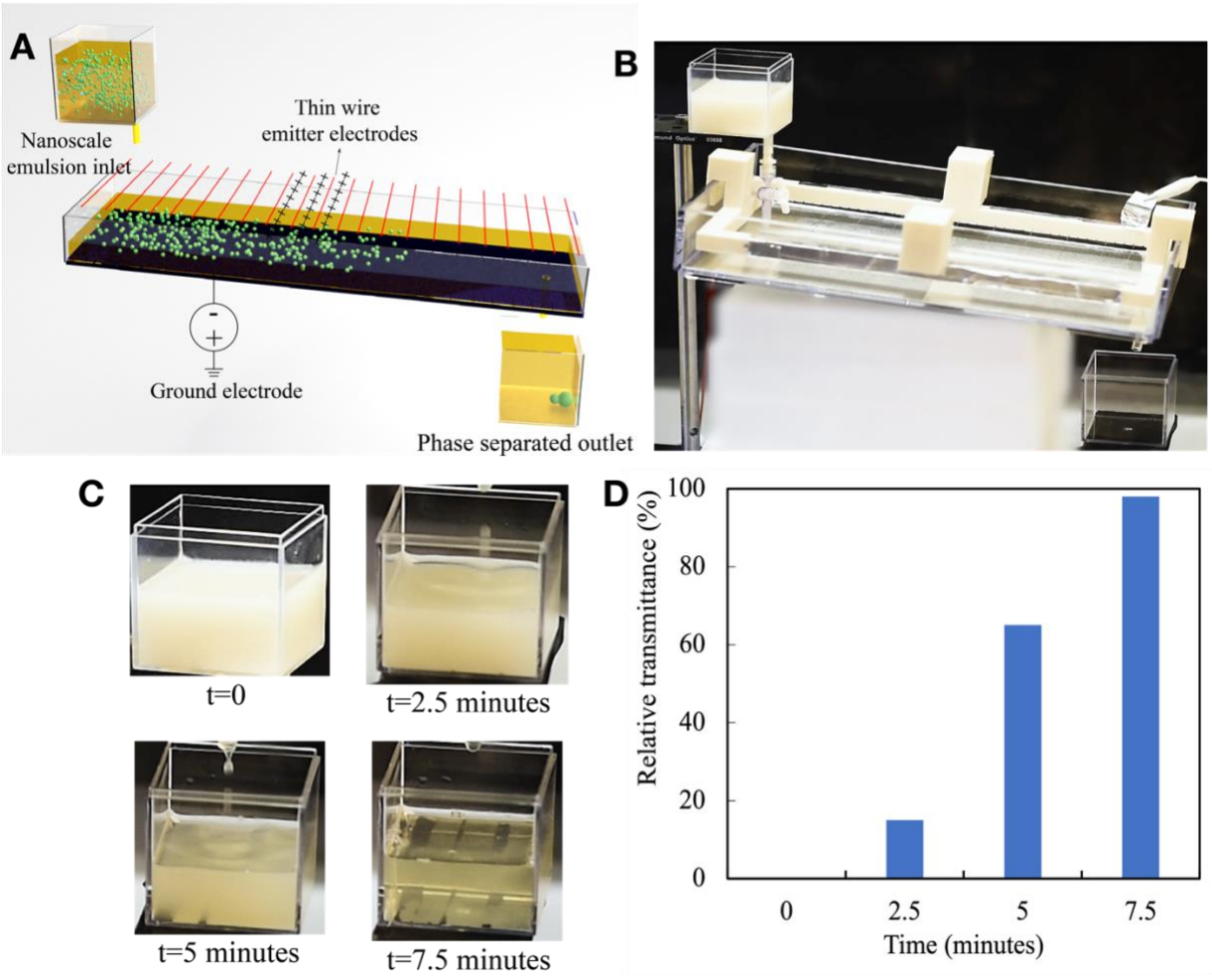


Figure 4-18. **Practical embodiment: Flow-through corona demulsification setup (A)** Schematic of the practical embodiment of our concept. We use an array of thin wire emitter electrodes (spaced ~1.5cm apart) at a high voltage that are arranged parallel at a constant spacing (~2.5 cm) from the bottom plate electrode which is electrically grounded. Electric field is

established between the wires and the ground via space charge injection. The emulsion flows from the inlet beaker on the top left to the collection beaker on the bottom right driven by gravity. **(B)** Lab-scale prototype for phase separating water-in-oil nanoscale emulsion. **(C)** The water-in-oil emulsion (2% water, 1% span80 in hexadecane, mean droplet size ~250 nm) phase separates and transforms its appearance from opaque milky white to transparent yellow tinge of the oil-span80 mixture in about 7.5 minutes, where we loop the flow through the device 3 times. **(D)** The plot shows change in relative transmittance of the emulsion mixture as a function of time. The transmittance almost reaches its saturation value which corresponds to the case where there are no water droplets, indication the phase separation efficacy using our device.

As the emulsion flows (2% water in hexadecane-1% span80, mean droplet size ~250 nm) through the setup, an electric field of ~7.5 kV/cm is applied between the electrodes. Figure 4-18B shows a snapshot of the setup. Since the flow is controlled by gravity in the current version of the setup, flow rate cannot be adjusted controllably. Therefore, once the top beaker fully empties, we pour back the collected partially demulsified emulsion from the bottom beaker to the top beaker to continue the electrocoalescence process. The snapshots of the emulsion at various stages of electrocoalescence are shown in Figure 4-18C. It can the seen that starting from the milky white appearance, the nanoscale emulsion almost turns transparent after ~7.5 minutes of flow through the setup and the relative transmittance reaches ~97% as shown in Figure 4-18D (see Movie 4-9). The yellow tinge at the end of demulsification results from the presence of span80 (which is yellow/light brown in color) in hexadecane.

## 4.4. Experimental Methods

### 4.4.1. Equipment and materials

- DC High voltage power source: Spellman; model no. SL30P600.
- High speed camera: Photron SA-Z
- DSLR camera: Nikon D750
- Hexadecane: Millipore sigma
- Span80: Millipore sigma
- Dynamic Light Scattering instrument: Anton Paar
- Probe sonicator: Sonics Vibra Cell VCX 750

- Sharp needles and thin wires from McMaster Carr

### 4.4.2. Preparation of nanoscale emulsion

The emulsion was prepared in batches of 100 ml. After adding appropriate amount of water, hexadecane and span80 to the beaker (corresponding to volume fraction of water), the probe of the sonicator is immersed 2 cm into the emulsion and the sonicator is operated for 2 minutes at 60% of the power. In table 1 we show the physical properties of the hexadecane-span80 mixture in comparison to that of light crude oil[149,156,158,163,164].

| **Material** | **Emulsion stabilizer** | **Density (kg/m$^3$)** | **Conductivity (nS/m)** | **Viscosity (cSt)** |
|---|---|---|---|---|
| Light crude oil (API gravity 30-40) | Asphaltene (1-10%) | <870 | ~10-200 | 2-8 |
| Hexadecane | Span80 (1-5%) | ~773 | ~10-100 | 4.46 |

Table 4-1. **Comparison of physical properties; model system vs light crude.** Physical properties of our model system using hexadecane as the oil and span80 as the surfactant emulates light crude oil, which is a common class of crude oil. The main properties of our interest are density, viscosity, and electrical conductivity of the oil medium.

### 4.4.3. Measuring the droplet diameter

The mean size of water droplets in the emulsion was measured with Dynamic Light Scattering (DLS) at room temperature using Anton-Paar instrument. The mean hydrodynamic diameter of the emulsions varied based on the water fraction from 150nm-700nm. Higher water fractions resulted in higher average droplet diameter between 500-700nm.

### 4.4.4. Experiments for measuring the maximum electric field strength

To estimate maximum electric field across the emulsion in a non-Laplacian electrocoalescer configuration, the current flow and electrical conductivity of the emulsion should be known. Electrical conductivity ($\sigma$) of hexadecane-span80 mixture was obtained from literature[156,158,164]. A sharp needle array of 5 needles was used as the emitter electrodes. A 75 ml cubic beaker was filled with 60 ml of hexadecane-5% span80. The spacing ($d$) between the immersed plate electrode and the tips of the needle electrode array was 5.5 cm. As the applied voltage ($V$) between the electrodes was increased, we measured the current flowing through the emulsion. For simplicity, to estimate

an average current density ($J$) we assumed that the current was flowing uniformly over the cross-sectional area of the emulsion beaker. Figure 4-9 shows the linear correlation between the parameters $\frac{J}{\sigma}$ and $\frac{V}{d}$.

### 4.4.5. Preparation of micro-scale emulsion

Microemulsion for qualitative droplet visualization experiments shown in Figure 4-14 were prepared by injecting a jet of brine water into a 10 ml vial of hexadecane- 1% span80 mixture using a 32-gauge needle pressed using the thumb. The exact droplet size here does not matter due to the qualitative nature of the experiment. The initial average droplet size was measured to be in $\sim 10\ \mu m$.

### 4.4.6. High-speed high-magnification imaging

Droplet chain formation and coalescence dynamics were visualized using high-speed high-magnification imaging. For this the nanoscale emulsion was poured in to a $1\ cm \times\ 1\ cm$ acrylic cuvette. Since droplet diameter and camera's depth of focus in this experiment are both on the order of 10 microns, it is quite challenging to obtain a complete droplet chain and its dynamics within the focus. The fully focused footage of chain formation and collapse was obtained after few careful trials.

### 4.4.7. Measurement of transmittance using mean gray value of the images

Nanoscale emulsion in the beginning is milky white in color and completely opaque. DLS measurement showed 0% transmittance through a 1cm cuvette. We define relative as the ratio of transmittance of emulsion to that of hexadecane-span80 mixture. We also defined a proxy for the relative transmittance of the emulsion using the color of the emulsion by mapping the color of the emulsion to a transmittance percentage. At the start of an experiment, the mean gray value of the color of the image of the emulsion is mapped to a transmittance value of 0%. We also take an image of the pure hexadecane- span80 mixture under similar lighting conditions with a black color background and map the mean grey value of the solution to a value of 100%. As electric field is applied across the emulsion the mean gray value slowly transitions from pure white to pure black color of the black background. We interpolate the intermediate mean grayscale values of the image of the emulsion beaker to obtain the transmittance percentage of the emulsion.

### 4.4.8. Quantification of rate of demulsification

We define the time taken for demulsification as the point of time when the relative transmittance of the emulsion reaches 95%. The transmittance can be measured using DLS transmittance or using the mean gray value.

### 4.4.9. Practical embodiment- flow setup

Emulsion flow setup for the practical embodiment was fabricated using thin wire array (120 microns diameter) as the emitter electrodes and a flat electrode as the bottom electrode. The flow was setup inside an acrylic box with top side open. The inside bottom of the box is made of conductive Aluminum tape that acts as the bottom electrode. The thin wire array was held on position using a plastic 3d printed fixture as shown in Figure 4-18B.

## 4.5. Conclusion

In summary, we demonstrate a simple non-Laplacian electrocoalescer based approach for significantly enhancing the rate of phase separation of water-in-oil nanoscale emulsion. We find that by using a space charge emitter electrode that introduces an air gap between the electrode and the emulsion, ~8X stronger electric field strength can be safely applied across the emulsion without electrical shorting. We demonstrate that the critical voltage before shorting is agnostic to the water fraction. These insights can lead to the development of a robust electrocoalescer system that works at all water fractions without using any toxic chemical demulsifiers. We visualized the dynamics of droplets to study the droplet chaining and droplet coalescence phenomena. We also demonstrate that the rate of oil-water separation scales with the square of applied voltage, as governed by the equation for the electrostatic dipole-dipole force of attraction. Last, we developed a practical embodiment that allows continuous flow that can efficiently demulsify water-in-oil nanoscale emulsion. Given the ever-increasing concerns of effluents from oil refineries and mitigating its impact on the environment, our chemical-free oil-water separation method completely eliminates one of the major issues of toxic chemical demulsifiers, making the oil-water separation process more sustainable and economic.

THIS PAGE INTENTIONALLY LEFT BLANK

# 5. Enhanced $CO_2$ capture using electrostatically collected mist

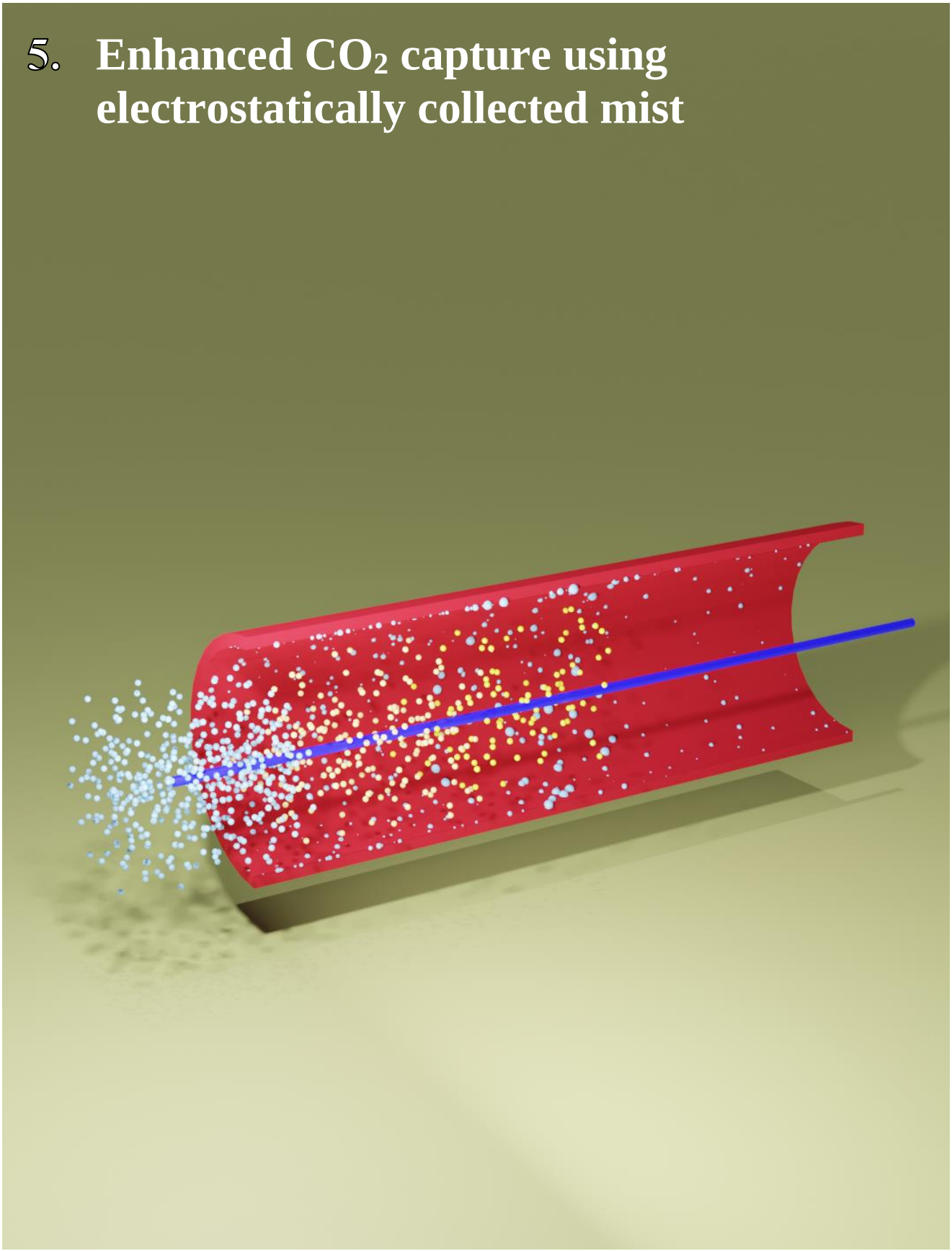

## 5.1. Abstract

Capturing $CO_2$ from concentrated sources such as power plant exhausts is an effective pathway for reducing $CO_2$ emissions at global scale. However, scaling up $CO_2$ capture systems is prohibitively expensive due to the high capital costs of absorption towers that capture $CO_2$ from flue gas. Industrial scale packed-bed absorption towers are few tens of meters in size to maximize the interaction between the gas and absorbent liquid. In this chapter we propose a two-stage $CO_2$ capture system where we utilize mist-size droplets to maximize interfacial area and rapidly absorb $CO_2$ from the flue gas without using conventional packed-bed towers. In the first stage, we mix mist with the flue gas for $CO_2$ absorption and in the second stage we introduce a mist capture unit that electrostatically collects the $CO_2$ laden mist via space charge injection with negligible backpressure. We demonstrate using our lab-scale setup at industrially relevant gas flux that we can achieve >95% $CO_2$ absorption into sorbent mist and collect the mist at ~100% efficiency using the electrostatic mist collection unit. We perform techno-economic analysis of our proposed system and show that our mist-based method can reduce the size of $CO_2$ capture systems by up to 5x, reduce the CAPEX by ~60% and also open the door to a whole new set of environmentally benign catalysts for $CO_2$ capture.

## 5.2. Introduction

### 5.2.1. Current methods for $CO_2$ capture

Global $CO_2$ emissions reached about 41 Gt in 2021 [35], placing an enormous strain on the Earth's climate stability [36,37] (Figure 5-1). Post combustion carbon capture in power plants offers one of the most effective pathways to reducing anthropomorphic emissions as capturing the $CO_2$ produced by a single 500MW natural gas power plant over a year would be equivalent to eliminating emissions from two hundred thousand cars over the same timespan [38,39]. Post-combustion carbon capture technologies can be classified into three main approaches: chemical, physical and biochemical [40,41,165]. Chemical approaches include adsorption, direct or membrane-assisted absorption into a liquid, and chemical looping combustion [166–170]. Physical approaches include membrane separation, physical absorption and cryogenic distillation [171–173]. More recently a variety of biochemical methods utilizing enzymatic and algae-based approaches have also been

proposed [174,175]. Of these methods, chemical absorption into a liquid absorbent is widely considered to be the most promising technology due to the higher efficiencies, lower costs and techno-economic maturity that it offers [40–44].

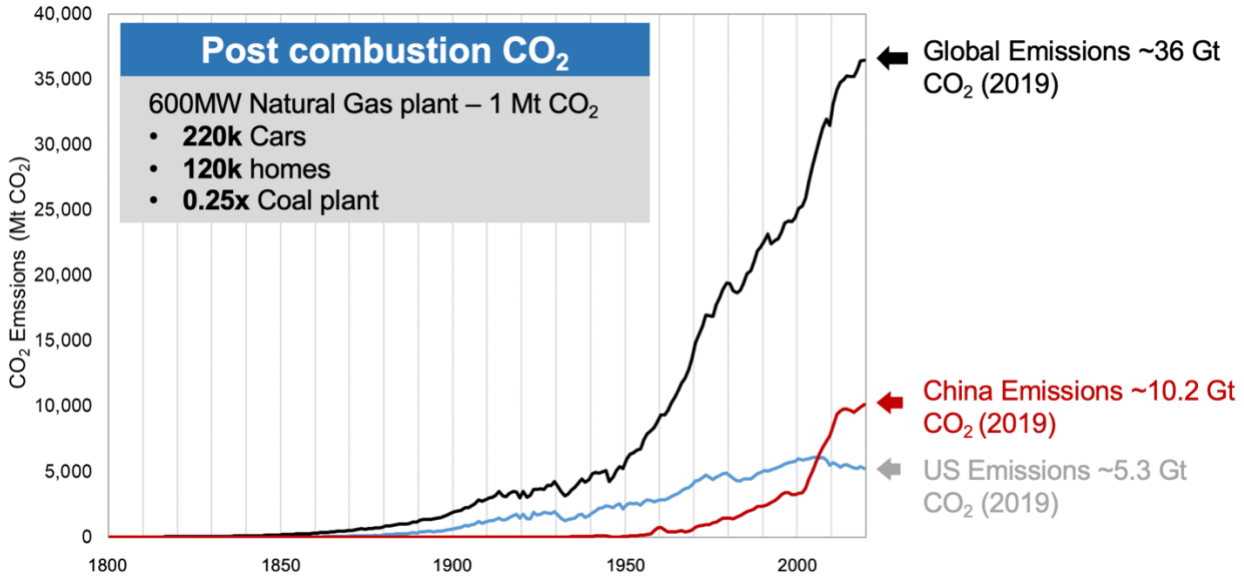


Figure 5-1. **Global $CO_2$ emission increase over the last 200 years**[39]

## 5.2.2. Packed bed for $CO_2$ capture and challenges

Most practical chemical absorption plants utilize packed bed reactors – an illustration of which is shown in Figure 5-4A. These reactors are tall towers filled with a number of packing units. Sorbent solution is provided at the top of the tower and flows down over the surface of the packing units; forming films of liquid that react with the rising flue gas stream. The packing units are designed to enhance the interfacial area and the contact time between the flue gas and the liquid absorbent [45]. In order to capture >90% of the $CO_2$ released from a power plant (where flue gas flow rates can vary between 100-800 kg/s), packed bed reactors need to be large enough to provide enough area and time for absorption to take place [46–48]. As a result, packed bed towers are routinely over 10m in diameter and over 40m in height (Figure 5-2); contributing to approximately 30% of the overall capital requirements for such carbon capture systems [49,50]. With prohibitively expensive costs being the primary reason for only 28 large scale carbon capture facilities existing worldwide

[51], reducing the size of these absorption towers would help enhance the practicality of post combustion carbon capture systems [52].

Figure 5-2. **Absorption tower at Petra Nova $CO_2$ capture facility, Texas**. This is one of the world's largest carbon capture and storage facility that costed more than $0.5 billion to construct. The absorption tower is more that 380 ft tall.[176]: Global CCS Institute.

### 5.2.3. Spray systems for $CO_2$ capture and their challenges

Spray towers theoretically provide a pathway towards much smaller absorber units. In spray towers, droplets of the absorbent are sprayed against the rising gas stream instead of having the absorbent flow as a thin film [177–180]. These droplets absorb $CO_2$ from the flue gas and are collected at the bottom of the tower. Equation set 5.1 demonstrates the enhancement to interfacial area afforded by droplets in comparison to the liquid films in packed beds.

$$\frac{A_p}{V} = \frac{1}{t}; \frac{A_d}{V} = \frac{N4\pi R^2}{N\frac{4}{3}\pi R^3} = \frac{3}{R}; \frac{A_d}{A_p} = \frac{3t}{R} = \frac{6t}{D} \qquad 5.1$$

In the above equations, $N$ is the total number of droplets, $A_p$ is the area of the packed bed, $V$ is the volume of the liquid absorbent, $t$ is the thickness of the liquid film in the packed bed, $A_d$ is

the area of the droplets that would make up the same volume of absorbent, and *R* and *D* are the droplet radius and diameter respectively. For the same volume of sorbent liquid *V*, the ratio of interfacial area of droplets vs packed bed is given by $\frac{A_d}{A_p} = \frac{6t}{D}$. Thus, if we assume similar characteristic size (*t*~*D*), droplets offer 6 times more interfacial area than films in packed beds [46,48,181]. Despite this advantage, in practice, spray towers offer lower $CO_2$ capture efficiencies than packed beds due to the following reasons. There can be droplet loss to the walls of the reactor which reduces the overall $CO_2$ capture efficiency [177]. Conventional spray towers are counterflow systems and thus rely on gravity to collect the absorbent droplets at the bottom of the towers. Therefore, the drops cannot be smaller than a few hundred microns as they could be entrained by the flue gas and escape through the exhaust (see supplementary). While passive demisters using meshes and other mechanical components could be considered for capturing entrained droplets that are small in size, they tend to fail at high liquid loading rates and introduce unfavorable back pressures to the exhaust system [182,183]. This means that the benefit of high interfacial area cannot fully be exploited in conventional spray towers. Droplets that are too large also present a problem as such droplets have slower reaction rates and fall faster through the tower resulting in lower residence time.

### 5.2.4. Introducing the sorbent as mist for enhanced $CO_2$ capture and reduced CAPEX

Here we propose a two-stage system (shown in Figure 5-4B) to leverage the advantages offered by droplets to its full extent. In the first – absorption stage, we propose using mist-scale droplets with diameters between 5 and 25 µm, which would allow our system to achieve up to a 240-fold increase to the interfacial area available between the absorbent and the gas compared to packed bed reactors for the same volume of liquid. While this could allow for absorber units that are significantly smaller in dimension, droplets of this size will be easily entrained by the gas flow (Figure 5-3). Entrainment and loss of droplets to the flow in mist or spray systems is governed by the non-dimensional parameter Stokes number $St = \frac{Inertia}{Drag} = \frac{2D^2\rho_w U_{flow}}{9\eta_g L}$. Here *D* is the size of the droplet, $U_{flow}$ is the gas flow velocity, $\rho_w$ is the density of the droplet, $\eta_g$ is the gas viscosity, and

*L* is the characteristic dimension of the flow system. Drag force dominates inertia when the droplet size is small.

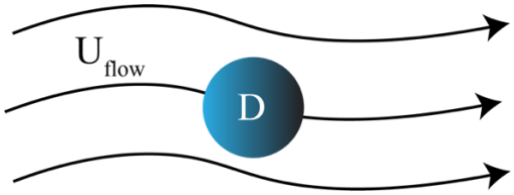


Figure 5-3. **Entrainment of droplets with flow**. The entrainment of droplets with the flow of the medium is characterized by Stokes number that considers the ratio of inertia to drag. Since large droplets have higher inertia, they have higher Stokes number and have lesser tendency to be entrained.

In order to capture the entrained mist droplets, we propose a second – electrostatic droplet capture stage. We introduce a thin wire emitter electrode and a collector electrode inside the exhaust pipe and apply high voltage between the electrodes. When the voltage is increased beyond a critical value (corona onset voltage)[184], the air in the vicinity of the wire electrode undergoes ionization, resulting in an electrostatic space charge injection or corona discharge (as shown in the expanded inset of Figure 5-4B). The space charge injection results in charged mist droplets which will be driven to a collector electrode due to the electrostatic field from where the liquid absorbent can be collected, processed and recirculated [184,185].

To better understand the ability of our proposed system to reduce the overall size of absorbers, we first estimate the lengths required for both stages ($CO_2$ absorption and electrostatic capture) of our system. We can model $CO_2$ absorption into droplets of different radii using existing empirical model as shown in Equation 5.2 developed by Choi et al. [186]. Since the benefits afforded by our proposed mist-based system are agnostic of the specific absorbent chemistry, we will utilize ammonia as a model absorbent.

$$\frac{\dot{m}_{CO_2}}{A} = k^{0.48}\, C_{g,s} C_l \left[ \frac{2.15 \times 10^{-6}}{C_{l,i}^{0.5}} + \frac{1.4 \times 10^{-7}}{D^{0.3}} \left( 1 - \frac{C_l}{C_{l,i}} \right)^{2.5} \right] \qquad 5.2$$

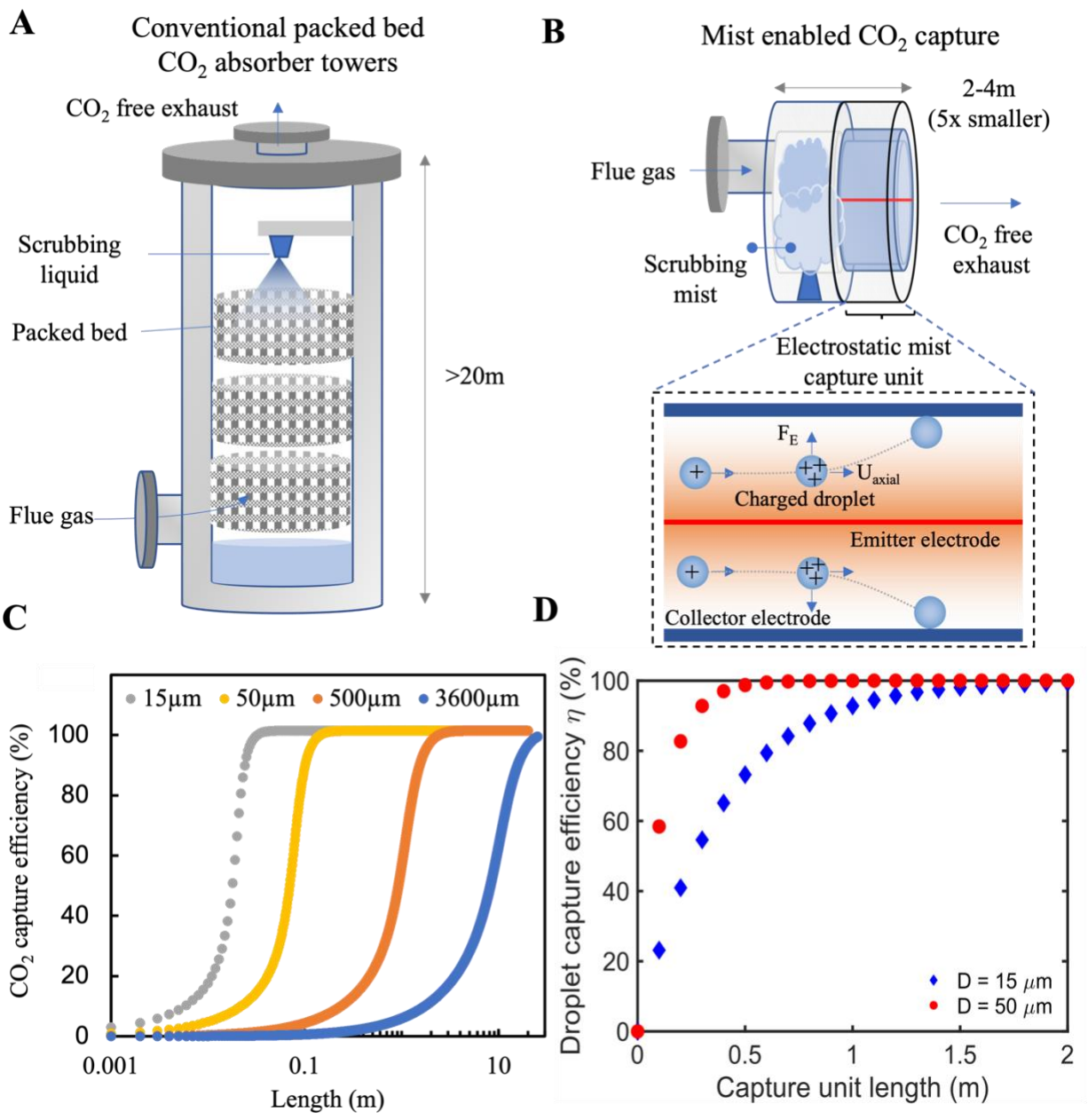


Figure 5-4. **Mist-scale droplets can enable significantly smaller and cheaper $CO_2$ capture systems. (A)** Conventional absorption towers use tall towers (>20m in height) and packed beds to enhance the interfacial area and the residence time of interaction between the scrubbing liquid and the flue gas during absorption. **(B)** Introducing the scrubbing fluid in the form of small mist droplets would allow for significantly shorter absorbers due to higher interfacial areas afforded by small droplets, however such mists are difficult to capture and recycle using passive demisters. Active electrostatic demister that charges the droplets can capture these mists without imposing significant back pressures at very high capture efficiency. **(C)** Calculated $CO_2$ capture efficiency for mist-based CO2 capture as a function of absorber length and droplet size for a liquid to gas

mass flow ratio of 1:1 using single-droplet model from literature. **(D)** Calculated mist capture efficiency for an electrostatic demister unit as a function of length for different average mist droplet diameters.

In Equation 5.2 $\dot{m}_{CO_2}$ is the mass flow rate of $CO_2$ into the droplet, *A* is the droplet area, *k* is the reaction rate constant, *C* represents concentration, and *D* is the droplet diameter. The subscripts, *g* and *l* represent the gas ($CO_2$-air mixture) and the liquid (sorbent) respectively. The subscript *s* represents the surface of the droplet and *i* represents the inlet of gas flow. Using a gas flow velocity of 3 m/s, an inlet $CO_2$ concentration of 15% and an ammonia concentration of 15wt%, we can estimate the $CO_2$ absorbed by a single droplet from its sphere of influence as a function of droplet travel distance. We use a liquid-to-gas mass flow ratio of 1:1 to define the control volume that follows an individual droplet as it travels with the gas flow. Using this framework, we can examine the benefit theoretically afforded by our approach for droplets of different sizes [49]. Since absorbent films in packed bed reactors are typically ~600 µm thick, we can replicate the interfacial area offered by packing units with a droplet diameter of 3600µm (since $\frac{A_d}{A_p} = \frac{6t}{D}$) for a given volume of liquid [48,181]. We find that such large droplets would also require absorber towers that are >20 m tall as shown in Figure 5-4C, confirming the role of interfacial area in absorption. In contrast, when we move to droplet diameters of 50µm and 15µm, the required lengths for >95% $CO_2$ absorption reduce significantly. In practice, the length of the absorption stage will be markedly larger than the dimensions predicted by the single drop model presented in Figure 5-4C as the model doesn't account for droplet-droplet interactions, local concentration gradients and for the practical constraints of introducing up to 800 kg/s of absorbent into a flue gas stream. However, the model does show that drastic reductions in absorber dimensions are possible by transitioning to mist-scale droplets.

For the second stage of our system, we can also estimate the maximum length required to capture ~100% of the mist droplets. Considering the cylindrical design of our electrostatic collector shown in Figure 5-4C we can compare the electrostatic force that a charged droplet would experience with the aerodynamic drag force. We estimate the characteristic radial velocity ($U_r$) of a mist-scale droplet as shown in Equation 5.3 [86]. Using the Deutsch-Anderson equation (Equation

5.4), we can then estimate the droplet collection efficiency ($\eta$) as a function of cylinder length ($L_c$), diameter ($D_c$) and gas flow rate ($Q$) as plotted in Figure 5-4D [184,187–189].

$$U_r \sim \frac{qE}{6\pi\mu R} = \frac{4\pi R^2 \varepsilon_0 E^2}{6\pi\mu R} = \frac{2R\varepsilon_0 E^2}{3\mu} \quad 5.3$$

$$\eta = 1 - e^{\left(-\frac{U_r A_c}{Q}\right)} = 1 - e^{\left(-\frac{U_r \pi D_c L_c}{C_{DA} Q}\right)} \quad 5.4$$

In the above equations $q$ represents the charge accumulated on a single droplet at saturation, $E$ represents the average electric field strength between the emitter and collector electrodes, $\mu$ is the viscosity of the flue gas, $R$ is the droplet radius, $\varepsilon_0$ is the permittivity of free space and $C_{DA}$ is the correction factor to the Deutsch-Anderson equation used for practical systems [184].

From Figure 5-4C and Figure 5-4D we see that the overall length of the absorber unit could be reduced from around approximately 20m in packed bed reactors for a 400MW power plant to less than 4m in the system proposed here [49]. This would enable a drastic reduction to the capital required for $CO_2$ absorber units [50]. To validate these models, we develop and test a scaled down version of our two-stage design. For the first stage of our system, we match the gas flux of industrial absorber units and study the effect of input $CO_2$ and catalyst concentration on $CO_2$ capture efficiency. For the second stage, we explore the droplet capture efficiency of a scaled down electrostatic system as a function of gas flow rate and the electric field strength. Finally, we present a techno-economic analysis to capture the reduction in plant capital expenditure that could be enabled by our mist-based system.

## 5.3. Results and discussion

### 5.3.1. Lab-scale $CO_2$ capture system

Figure 5-5A presents an illustration of the experimental setup we developed in this work. Flow controlled $CO_2$ and air streams were mixed to achieve desired concentrations of $CO_2$ at the inlet to the system. The gas was then introduced to a misting unit where droplets were entrained into the gas flow (see Experimental Methods). In our setup, aqueous potassium hydroxide (KOH) solution was used as the absorbent for simplifying the experimental setup. The gas and the entrained mist then flowed through a fixed length of piping to allow time for absorption. The mixture then flowed into the electrostatic demister unit where all the absorbent drops were

removed. Finally, an infrared $CO_2$ sensor was used to quantify the $CO_2$ captured in the system. Figure 5-5B shows a histogram of droplet diameters produced by our misting unit. The histogram was obtained by visually recording the mist droplets as the passed through the viewing window when the electrostatic droplet capture unit was turned off (see Experimental Methods and Figure 5-6). The histogram gives us an accurate representation of the droplets that are being entrained by the gas flow.

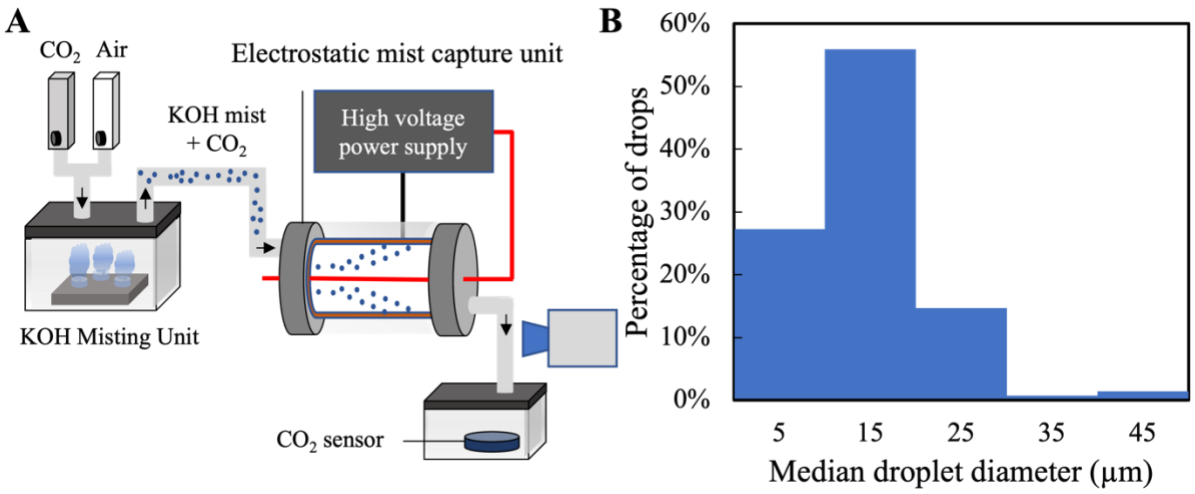


Figure 5-5. **Scaled-down experimental setup for mist-based $CO_2$ capture (A)** $CO_2$ was mixed with air at various ratios and introduced into a misting unit. The catalyst (aqueous KOH solution) mist was entrained by the gas flow and proceeded to absorb the CO2 in the gas stream. The mist laden gas flow was then directed to an electrostatic capture unit before exiting into a CO2 sensor that measured $CO_2$ capture efficiency. (**B**) Histogram of droplet diameters generated by the misting unit indicate that a majority of droplets fall within a diameter range of 5-25 µm.

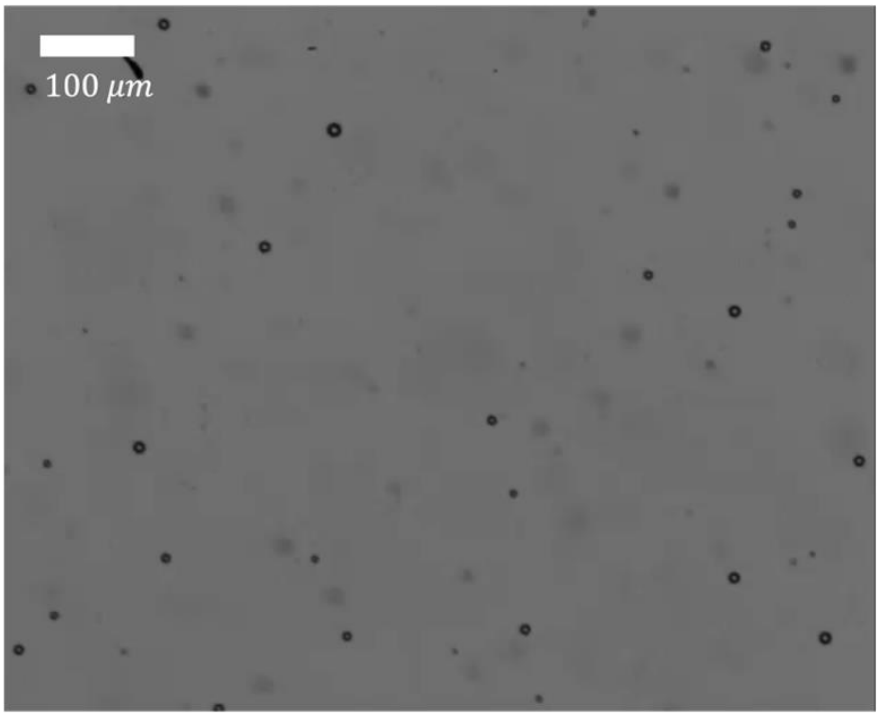


Figure 5-6. **Imaging of mist droplets**. A sample microscope image showing mist droplet distribution. The mist droplet size distribution was analyzed by capturing the flow of entrained mist droplets using high-speed, high-magnification imaging. The droplet size was estimated by image thresholding and calculating the average ferret diameter of circular fit using ImageJ.

### 5.3.2. $CO_2$ absorption efficiency using mists

For appropriately scaling down our experimental $CO_2$ absorber system, the flow rate of the inlet gas was varied between 1 and 5 lpm such that the gas flux is on the same order of magnitude as that of industrial $CO_2$ capture units (1 $kg/m^2/s$). We kept the $CO_2$ concentration constant at 50%. Figure 5-7A shows the $CO_2$ capture efficiency of the system for these experiments. We observe that while the capture efficiency reached ~75 ± 5% for the flowrates of 1 and 3 lpm, it dropped down to about 64 ± 5% for the 5 lpm case. To characterize this reduction in performance, we normalize the gas flux through our experimental setup by the flux achieved in industrial absorption systems [190]. The normalization is performed to consider the fact that industrial absorber systems are carefully designed to optimize the gas flux to achieve the maximum capture efficiency possible. In Figure 5-7B, we plot the ratio of the experimental and the industrial gas fluxes and find that the case of 5 lpm has a flux that is on the higher end compared to the gas flux in industrial systems, thus resulting in the drop in performance.

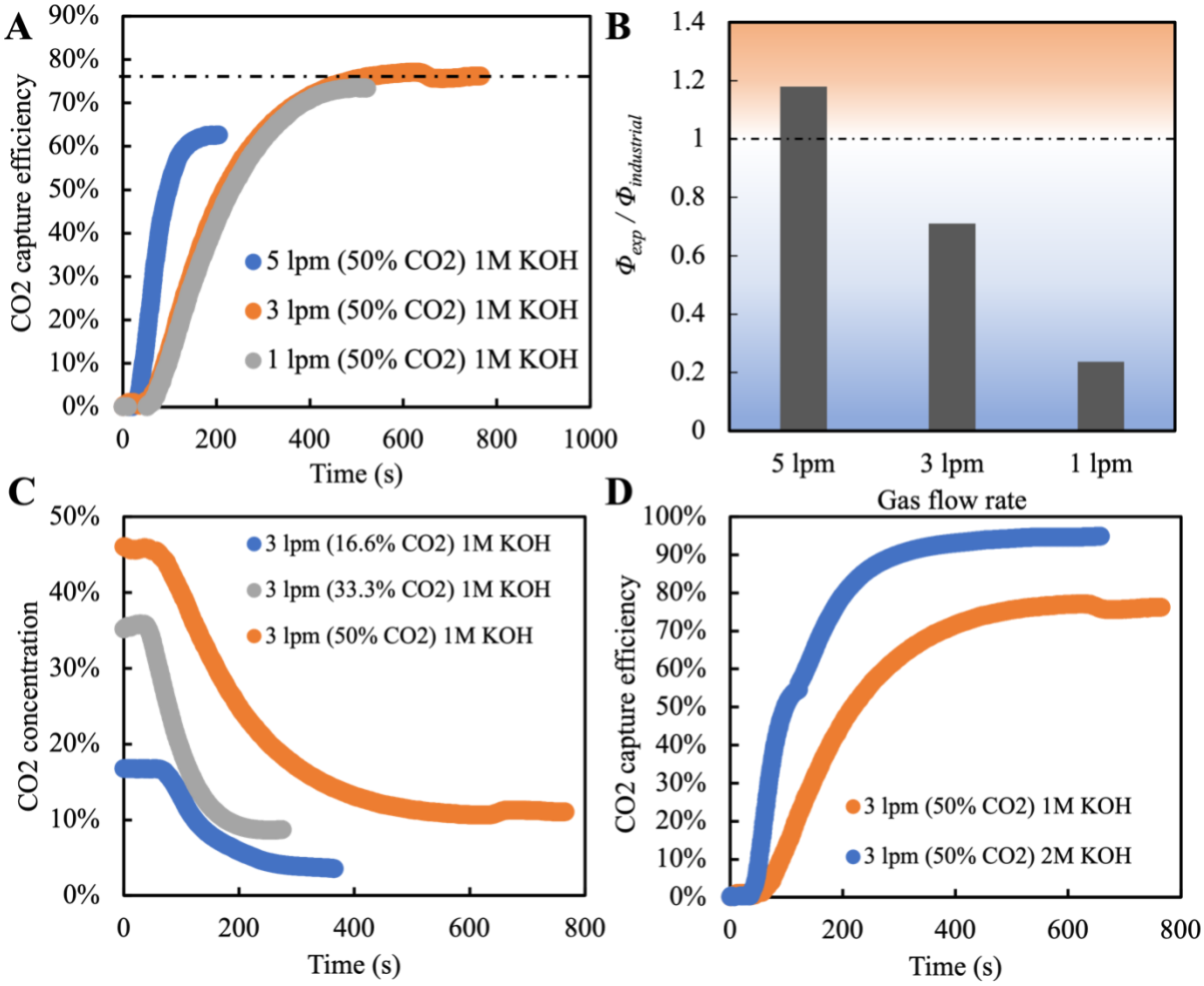


Figure 5-7. **Mists enable high absorption efficiencies.** (**A**) $CO_2$ capture efficiency is plotted as a function of time after the misting unit is switched on for varying gas flow rates, at an input $CO_2$ concentration of 50%. The capture efficiency drops from 75 ± 5% at 1 and 3 lpm flow rate to 64 ± 5 % at a gas flow rate of 5 lpm, indicating that that the liquid to gas ratio and the residence time are too low for the scrubbing to be maximally effective. (**B**) A comparison of normalized gas flux in kg/($m^2$s) of our experimental setup and industrial systems. At 5 lpm gas flow rate, the flux is on the higher end of the industrial system gas flux and is therefore harder to optimize the $CO_2$ capture. (**C**) $CO_2$ concentration plot demonstrates the effect of varying the $CO_2$ concentration while holding flowrates constant. In these experiments, even though the absolute $CO_2$ concentration at the exit were different, the capture efficiencies were > 70% demonstrating the ability of the technique to be robust to input $CO_2$ concentrations and demonstrating that at these conditions, the capture efficiency is limited by absorbent chemistry. (**D**) Illustrates the effect of changing absorbent chemistry by plotting the $CO_2$ capture efficiency for different concentrations of the catalyst (KOH

solution). Up to 95±5% capture efficiency can be achieved with 2M KOH solution. The liquid to gas flow ratio was measured to be 21 ± 5 for these experiments in the case of 3 lpm gas flow rate.

We thus set the flow rate to 3 lpm, to stay in a favorable flux regime for the remaining absorption experiments. First, we varied the input $CO_2$ concentration from ~16.66% to 50% as shown in Figure 5-7C. In all of these cases, we observe a capture efficiency of approximately 70 ± 5% which is consistent with other industrial KOH-based absorption units [191]. The liquid to gas mass flow ratio (L/G) of was measured to be approximately 21 ± 5 for a gas flow rate of 3 lpm (see Experimental Methods) and this value is also on the same order as industrial and other experimental systems [177,191].

Equation 5.5 shows the stoichiometric reaction between KOH and $CO_2$. In our experimental setup, at a gas flow rate of 3 lpm, the molar flow rates of KOH and $CO_2$ are 1.7 and 1.1 milli-moles per second. Since two moles of KOH are needed to react with every mole of $CO_2$, the stoichiometric capture efficiency is ~73% (see section 5.3.3). To validate that the 70 ± 5% experimental capture efficiency observed here is indeed limited by the chemical concentration of the absorbent, we increase the KOH concentration from 1M to 2M and observe that the $CO_2$ capture efficiency increases to 95 ± 5% for the case of a 3 lpm gas flow rate and a 50% inlet $CO_2$ concentration as shown in Figure 5-7D. These results illustrate the promise of mist-based carbon capture, especially in terms of enabling a wider range of absorbents that could have a better environmental and safety profile than the toxic chemicals such as Monoethanolamines (MEA) that are currently preferred in absorber units [41].

$$2KOH + CO_2 \rightarrow K_2CO_3 + H_2O \qquad 5.5$$

### 5.3.3. KOH saturation in mist droplets

Assuming that the whole of KOH reacts with $CO_2$, we can calculate (ignoring the reaction kinetics) how much $CO_2$ capture is possible at maximum. The reaction between KOH and $CO_2$ is given as $2KOH + CO_2 \rightarrow K_2CO_3 + H_2O$. Thus, each mole of $KOH$ can react with ½ mole of $CO_2$. Since 1 mole of air takes 22.4 liters, there are 1/22.4 moles per liter of air. And the equivalent molar mass of air-CO2 mixture in grams/mol is given by Equation 5.6.

$$(1-\phi_{CO_2})29+\phi_{CO_2}44 \tag{5.6}$$

Therefore, we can write the mole flow rate of $CO_2$ in moles/s as $\frac{V_{gas_{lpm}}\phi_{CO_2}}{22.4*60}$. Thus, the mass flow rate of gas (kg/s) is $\dot{m}_{gas}=\frac{V_{gas_{lpm}}}{22.4\times60}\frac{((1-\phi_{CO_2})29+\phi_{CO_2}44)}{1000}$. If $\frac{L}{G}$ is the liquid to gas flow rate ratio by mass, the mass flow rate of liquid (kg/s) is given by Equation 5.7.

$$\dot{m}_{liquid}=\frac{L}{G}\dot{m}_{gas}=\left(\frac{L}{G}\right)\frac{V_{gas_{lpm}}}{22.4\times60}\frac{((1-\phi_{CO_2})29+\phi_{CO_2}44)}{1000} \tag{5.7}$$

Here $V_{gas_{lpm}}$ is the flow rate of gas in lpm, $\phi_{CO_2}$ is the volume fraction of $CO_2$ $\dot{m}_{gas}$ is the mass flow rate of gas, L/G is the liquid to gas flow rate ratio by mass, $\dot{m}_{liquid}$ is the mass flow rate of liquid and $M_{KOH}$ is the molarity of KOH. The mole flow rate of KOH (moles/s) is therefore given as $M_{KOH}\left(\frac{L}{G}\right)\frac{V_{gas_{lpm}}}{22.4\times60}\frac{((1-\phi_{CO_2})29+\phi_{CO_2}44)}{1000}$.

Since each mole of $KOH$ can react with ½ mole of CO2, the maximum possible $CO_2$ capture is given by Equation 5.8.

$$\eta_{capture}=\frac{1}{2}*\frac{\text{Mole flow rate of KOH}}{\text{Mole flow rate of CO2}}*100$$

$$=\frac{1}{2}*\frac{M_{KOH}\left(\frac{L}{G}\right)\frac{V_{gas_{lpm}}}{22.4\times60}\frac{\left((1-\phi_{CO_2})29+\phi_{CO_2}44\right)}{1000}}{\frac{V_{gas_{lpm}}\phi_{CO_2}}{22.4*60}}*100$$

$$\eta_{capture}=\frac{1}{2}*\frac{M_{KOH}\left(\frac{L}{G}\right)\left((1-\phi_{CO_2})29+\phi_{CO_2}44\right)}{\phi_{CO_2}}*100 \tag{5.8}$$

By substituting the following gas flow parameters: 3 lpm gas flow rate, 50% CO2 at the inlet, 1M KOH, L/G~20, we can calculate the maximum possible $CO_2$ capture for the specific flow conditions as $\eta_{capture}=\frac{1}{2}*\frac{1(20)((1-0.5)29+0.5*44)}{0.5*1000}*100=73\%$.

### 5.3.4. Estimation of evaporative loss of mist droplets

Assuming ~30 degrees Celsius after the exhaust gas cools down following the $SO_2$ scrubbing, the mass fraction of water in air is $\phi_{water-vapor} = 0.02684$ if the relative humidity were to reach 100%. If the mass flow rate of air is $\dot{m}_{gas}$, then mass flow rate of liquid lost to air is $\dot{m}_{gas} \times \phi_{water-vapor}$. Thus, fraction of liquid lost if there is complete evaporation is $\frac{\dot{m}_{gas} \times \phi_{water-vapor}}{\dot{m}_{liquid}} = \frac{G \times \phi_{water-vapor}}{L}$.

Assuming $\frac{L}{G} \sim 20$, the percent of water lost is $\frac{G \times \phi_{water-vapor}}{L} * 100 = \frac{0.02684}{20} * 100 = 0.134\ \%$

Assuming all droplets evaporate similarly, the percentage change in droplet size can be calculated by the following set of equations.

$$dV * 100 = 3 * \frac{4}{3}\pi R^2 dR * 100 = 3V * \frac{dR}{R} * 100$$

$$\frac{dR}{R} * 100 = \frac{dV}{3V} * 100 = \frac{0.134}{3} = 0.044\%$$

This shows that even if the droplets evaporate to cause humidity saturation in the flue gas, the size of the droplets change only by 0.044 percent and the volumetric evaporative loss is just 0.134%. Therefore, evaporative losses can be neglected for modeling and practical purposes.

### 5.3.5. Mist capture efficiency using electrostatic capture system

Having demonstrated the ability of mist-scale droplets to achieve $CO_2$ capture efficiencies >95 % we explore the ability of our scaled down electrostatic unit to capture the mist droplets. Figure 5-8A and Figure 5-8B show conceptual schematics of the operation of mist capture unit when there is no applied voltage and when there is a strong electrostatic space charge injection respectively. Figure 5-8C and Figure 5-8D show the images of the exit of the electrostatic demisting unit when the voltage is off vs when there is electrostatic mist collection (see Movie 5-1, Movie 5-2), visually illustrating the ability of our scaled-down demister to completely capture mist for a gas flow rate of 3 lpm and a voltage of approximately 8 kV.

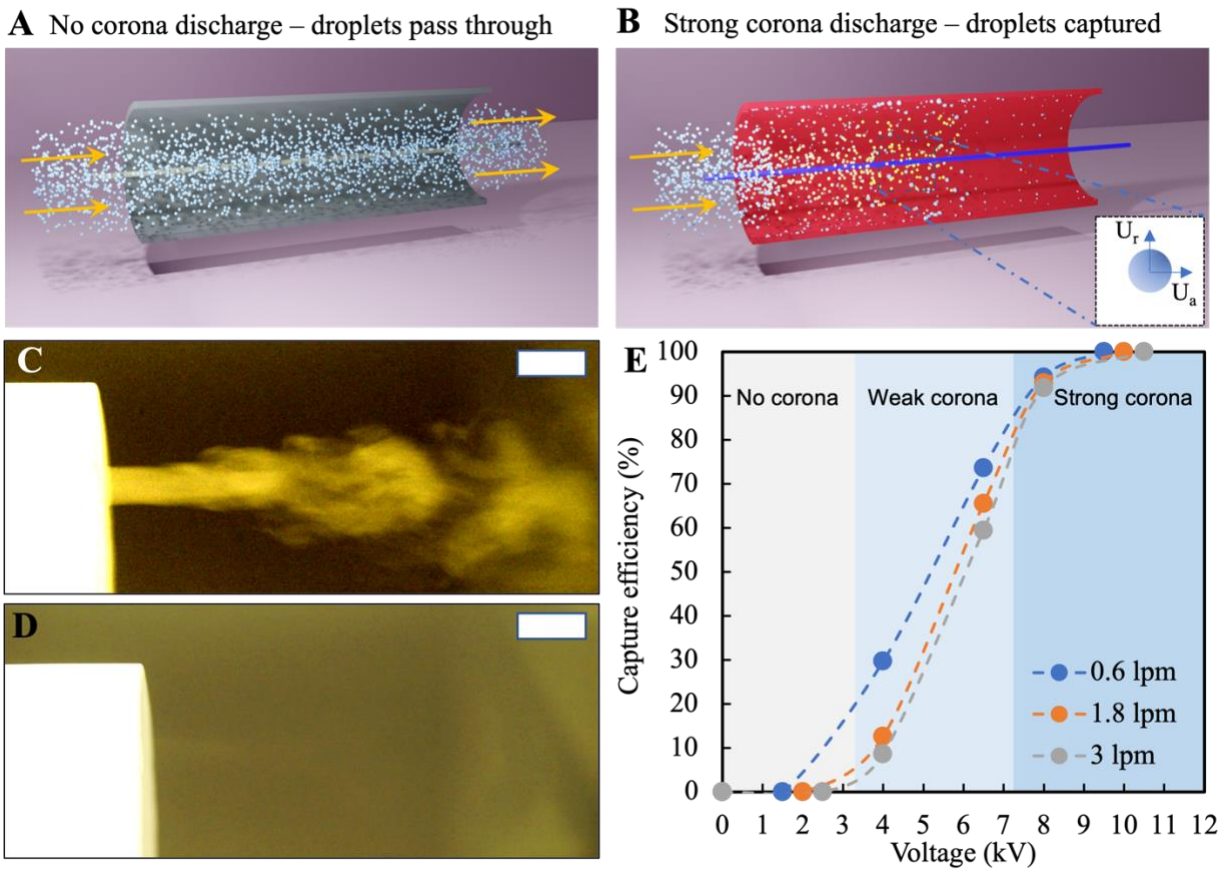


Figure 5-8. **Capturing mist using space charge injection** (**A**, **B**) Conceptual schematics of the mist capture system in the off and on states. (**C**, **D**) Images corresponding to the extreme states tested in the mist capture unit. (**C**) When the voltage source is off, mist exits the capture unit as it is entrained by the gas flow resulting in zero capture efficiency. (**D**) When the emitter electrode produces a strong corona discharge, all the mist is captured on the collector electrode, resulting in no mist entrainment at the gas outlet. Scalebar is 1cm. (**E**) The droplet capture efficiency is plotted as a function of the applied voltage and for different gas flow rates, illustrating the ability of our active approach to efficiently capture ~100% of the mist.

Figure 5-8E shows the mist capture efficiency as a function of gas flow rate and applied voltage. When the voltage isn't high enough to the generate a corona discharge (below the onset of corona discharge), the droplets aren't charged and therefore do not get collected. All droplets are thus entrained along with the gas flow as shown in Figure 5-8C. Thus, even though there is $CO_2$ absorption into the mist, not being able to prevent the entrainment of mist means that the effective $CO_2$ capture efficiency is ~0. As the voltage is increased, the applied voltage overcomes the corona onset voltage and begins space charge injection to electrostatically charge and collect droplets. In this regime, shown as the "weak corona" regime in Figure 5-8E, the electric field is

relatively weak and there is poor concentration of space charge in the gas stream. Thus, the driving force to collect the droplets on the collector does not overcome by the drag force and therefore a fraction of mist is lost due to entrainment resulting in partial $CO_2$ capture. However, in the region of strong corona discharge, we achieve ~100% capture as nearly all the droplets become charged and are transported to the grounded collector. The maximum value of the nominal electric field strength applied in our scaled down system is ~4 KV/cm which is well within the field strength used in scaled-up electrostatic precipitation systems indicating the practical promise of our two-stage system [184].

### 5.3.6. Techno-economic analysis of mist-based $CO_2$ capture

Our experiments demonstrate that when our two-stage absorber is appropriately scaled down, we can achieve $CO_2$ capture efficiencies between up to $95\pm5\%$ and that all the mist droplets can be captured effectively. To assess the economic feasibility of our mist-based post combustion carbon capture approach, we estimate the required capital expenditures (CAPEX) to install our system and compare it to the CAPEX required for a conventional vertical packed bed absorber tower. For the conventional vertical packed bed architecture, two absorber towers of heights 19.06m and diameters of 11.93m are chosen from an optimized MEA $CO_2$ capture system for a 400MW gas-fired power plant with a flue gas rates of 622 kg/s [49]. Purchased costs of the absorber tower housing and the internal components are estimated from average historical data and subsequently adjusted via the Chemical Engineering Plant Cost Index (CEPCI) to 2019 USD [192]. A typical Lang Factor of 4.74 was applied to yield the estimated installed cost of the system components tabulated in Table 5-1.

| Subsystem description | Packed Bed Architecture Cost ($USD MM) | Mist Capture Architecture Cost ($USD MM) |
|---|---|---|
| **Absorber unit - CAPEX** | | |
| Absorber unit housing | 81.3 | 9.0 |
| Packed Bed | 57.9 | -- |
| Liquid nozzles | 4.9 | 3.8 |
| Pressure pumps | 2.8 | 3.4 |
| **Mist capture system - CAPEX** | | |

| | | |
|---|---|---|
| Passive de-misting | 2.5 | -- |
| Space charge capture | -- | 42.6 |
| **Total CAPEX** | **149.4** | **57.3** |

Table 5-1. **Breakdown of costs of scaled up mist-based capture system.** $CO_2$ absorption capital expenditure estimates for a 400MW gas fired coal plant for conventional vertical packed-bed architectures compared to the proposed mist-capture architecture. Owing to the substantial reduction in absorber unit housing size and the avoidance of packed beds, the mist capture architecture has a CAPEX ~2.6x lower than conventional packed bed architectures. Costs are based on historical pricing (Turton et. al) and scaled accordingly for their capacity, material selection, and operational pressures.

The estimated total CAPEX for the packed bed system is $149M, which agrees with values estimated by Agbonghae et al. for the same absorber configuration [49,50]. As expected, the stainless steel-clad carbon steel absorber tower is a key cost driver, accounting for over 50% of the cost. To estimate an analogous CAPEX for our mist-based $CO_2$ absorption system, the same flue gas flow rate and absorber unit housing diameter were used as in the previous case. By leveraging the enhanced absorption kinetics of mists, the absorber housing unit length can be reduced by a factor of 5x as shown in Figure 5-4. Moreover, it can be installed in a horizontal configuration as it no longer uses gravity-driven flows, thereby reducing installation cost factors. The costs of the electrostatic mist capture unit are derived from historical costs and installation factors, scaled for capacity, and adjusted with the CEPCI index [193]. At a CAPEX of $57.3M, our mist-based $CO_2$ absorption system offers a ~2.6x reduction in capital cost compared to conventional packed bed absorption towers. These savings are due to the elimination of the packed beds in addition to a reduction in absorber unit housing costs associated with smaller total dimensions.

## 5.4. Experimental Methods

### 5.4.1. Gas mixing and mist generation

Brooks® mechanical flow meters were used to control the flow rates of the $CO_2$ and air before the two gas streams were mixed using a T-junction. The mixed gas was introduced into the headspace of an air-tight container that contained a bath of the KOH absorbent and an ultrasonic misting unit (Mxmoonant® 6 Head Ultrasonic Mist/Fog maker). The experiments were started with

the misting unit and the mist capture units turned off. The initial concentration of the $CO_2$ was recorded after the gas flowed through the headspace of the air-tight container so that any effects of the bath of absorbent were considered in the control measurement. When the ultrasonic mister was turned on, mist scale droplets were ejected into the headspace of the air-tight container and subsequently entrained by the gas flow.

### 5.4.2. $CO_2$ sensor

$CO_2$ concentrations were measured using a GC-0007 ExplorIR® sensor. After the gas exited the sensor was placed in line with the gas stream in a vented container.

### 5.4.3. Electrostatic mist capture unit

The electrostatic mist capture unit consists of two electrodes. The emitter electrode is made of thin stainless steel in the form of a wire of diameter 0.3 mm. The collector electrode is an annular cylinder of inner diameter ~9 cm made of aluminum. The thin wire runs along the axis of the collector electrode. The gas that exits after reacting with the KOH mist goes the aluminum collector electrode while entraining the mist along with it. We applied different voltages in the range of 0-12 kV between the thin wire and collector electrode using Spellman SL30P600 high voltage device.

### 5.4.4. Mist droplet size analysis

The mist droplet size distribution was analyzed by capturing the flow of entrained mist droplets using high-speed, high-magnification imaging using Zeiss AxioZoom microscope and Photron SA-Z high speed camera. The droplet size was estimated by image thresholding and calculating the average ferret diameter of circular fit using ImageJ.

### 5.4.5. Measuring L/G ratio

The ratio of liquid to gas flow rate by mass is one of the most important parameters that governs the $CO_2$ capture efficiency. The air flow rate is easily estimated by knowing the flow rate of $CO_2$ and air as measured by the flowmeters. The liquid flowrate is estimated by measuring the weight of the collected water over a certain interval of time. For the same interval of time, we

estimate the total mass flow of gas mixture to obtain the parameter L/G by taking the ratio of total mass flow of liquid to gas.

### 5.4.6. Estimating the electrostatic droplet capture efficiency

The electrostatic droplet capture efficiency is estimated using DSLR camera images of the mist exiting out of the misting unit. We placed a black-colored background behind the mist flow exit and measured the mean gray value with and without mist flow when the voltage is off. Since mist droplets scatter light in all directions, the mean grey value of the captured image of mist exit is highest when there is maximum amount of mist exiting the outlet, i.e., when the voltage is switched off. The mean gray value is the lowest (due to dark background) when there is absolutely no mist exiting the outlet, i.e., when the mist generator is switched off. We obtain the mist capture efficiency at various applied voltages by interpolating the mean grey values of images between maximum and minimum values.

## 5.5. Conclusion and outlook

In conclusion, we have demonstrated a simple, yet efficient absorber system to capture CO2 using mist-scale droplets. Using a scaled down experimental setup that matches the gas flux and L/G ratios of various industrial and experimental post combustion carbon capture systems, we were able to achieve $CO_2$ capture efficiencies up to $95\pm5\%$ using potassium hydroxide solution as the absorbent. We were also able to demonstrate the ability of our electrostatic droplet capture unit to collect ~100% of the entrained droplets at an electric field strength that is consistent with industrial systems. Finally, we use chemical engineering plant economic models to estimate that a scaled-up installation of the proposed system could reduce $CO_2$ absorber costs by a factor of ~2.6. While these results are promising there are experimental avenues to explore before the methodology can be validated for scaled up use. Making the L/G ratio independent of the gas flow rate would allow for the exploration of lower liquid fractions and help benchmark the performance under a wider range of industrially relevant operating conditions. Secondly, testing the system with other absorbents would help develop models that can more accurately predict absorption efficiency as a function of length by taking droplet interactions into account. While such efforts and experiments that can more accurately capture the flow conditions inside flue gas streams would greatly improve understanding, the concept, framework, and experimental results

presented in this work prove the promise of using mist-scale droplets for significantly cost-effective CO2 capture.

THIS PAGE INTENTIONALLY LEFT BLANK

# 6. Conclusion

In this thesis, we explored various approaches based on introduction of surface charge at interfaces to improve the efficiency and sustainability in three separate systems in the energy domain- photovoltaics, oil-and-gas, and $CO_2$ capture systems.

In the first part, in Chapter 1, we presented a simple electrostatic induction-based method for recouping the lost power output, mitigating the dust-accumulation problem on solar panels. We discovered that moisture-assisted charge induction can be used to make dust particles reject from surfaces even if they mostly contain insulating silica material. We calculated this charge experimentally and demonstrated that the dust particles are electrically conductive. In order to determine the voltage needed for particle removal, we characterized the dust removal process for various particle sizes. Furthermore, we demonstrated that our method works whenever the relative humidity of the ambient environment is greater than 30% and can restore 95% of the lost power. We explored how to take advantage of the variation in ambient humidity to make our strategy broadly applicable. We expect that our waterless electrostatic cleaning can offer an effective and affordable method for maintaining dust-free solar panels, contributing to the sustainable operation of solar farms.

In Chapter 2, we showed how the use of nano-textured surfaces can considerably improve electrostatic dust removal for cleaning solar panels in the small particle regime (<30 $\mu$m). We showed that, when compared to plain or microtextured surfaces, nanotextured surfaces can exhibit a reduction in the Van der Waals force of adhesion of up to two orders of magnitude. We demonstrated that, in comparison to plain or micro-textured surfaces, the decrease in pull-off force results in a 3.5x greater electrostatic removal of 15 $\mu$m particles. We fabricated transparent, electrically conductive, nanotextured glass that can be fitted on top of solar panel surfaces in order to apply this finding to solar panels that need transparent surfaces. Using a scalable copper nano-mask-based nanofabrication technology, we created nanotextured glass substrates such that the method may also be used to full-scale solar panel glass surfaces. We demonstrated that we could recover > 99% of lost power output for particles >30 $\mu$m and recover > 90% of lost power output in the small particle regime using a bench-top solar panel dust removal setup with nanotextured

solar panels. Our method, which enables significantly higher dust removal efficiency in the small particle regime, almost completely eliminates the water footprint of photovoltaic systems, contributing to the truly sustainable operation of solar farms, given the enormous potential and global applicability of active dust repulsion systems in photovoltaics.

In the second part, in Chapter 3, we showed how to dramatically speed up the phase separation of a water-in-oil nanoscale emulsion using a non-Laplacian electrocoalescer-based method. We discovered that an 8X greater electric field strength can be delivered across the emulsion safely and without electrical shorting by utilizing a space charge emitter electrode that creates an air gap between the electrode and the emulsion. We showed that the water fraction has no effect on the critical voltage prior to shorting in non-Laplacian electrocoalescer system. These findings may help create a reliable electrocoalescer system that operates at all water fractions without the use of hazardous chemical demulsifiers. To investigate the phenomena of droplet chaining and droplet coalescence, we visualized the dynamics of droplets. We also showed that, according to the equation governing the electrostatic dipole-dipole force of attraction, the rate of oil-water separation scales with the square of applied voltage. Finally, we created a practical embodiment that enables continuous flow and effectively demulsifies water-in-oil nanoscale emulsion. Our chemical-free oil-water separation approach mitigates one of the key challenges of using harmful chemical demulsifiers, making the oil-water separation process more sustainable and practical while also reducing the environmental impact of effluents from oil refineries.

In the third and final part, in Chapter 4, we illustrated a simple yet effective absorber system that uses mist-scale droplets to capture $CO_2$. We were able to achieve $CO_2$ capture efficiencies up to 95% utilizing potassium hydroxide solution as the absorbent by using a scaled-down experimental setup that matched the gas flux and L/G ratios of several industrial and experimental post-combustion carbon capture systems. Additionally, we were able to show that our electrostatic droplet capture device can catch ~100% of the entrained droplets at an electric field strength suitable for commercial systems. Finally, we calculate that a scaled-up installation of the suggested system might lower $CO_2$ absorber costs by a factor of about 2.6 using powerplant economic models. Although the results are encouraging, more experimental work needs to be done before the methodology can be deployed for larger-scale application. The exploration of lower liquid fractions and benchmarking performance across a wider variety of industrially relevant operating

circumstances would be made possible by making the L/G ratio independent of the gas flow rate. Second, by taking droplet interactions into consideration, evaluating the system with different absorbents will aid in the development of models that can more precisely predict absorption effectiveness as a function of length. The concept, framework, and experimental findings presented in this work demonstrate the promise of using mist-scale droplets for significantly more affordable $CO_2$ capture, even though such efforts and experiments that can more accurately capture the flow conditions inside flue gas streams would greatly improve understanding.

# 7. Appendix

## 7.1. System level design: Smart electrostatic dust removal system

To progress towards our goal to build a fully autonomous solar panel cleaner that electrostatically removes dust particles, we designed an integrated optical tracker system that provides output to the dust removal mechanism. That way we avoid keeping the solar panel cleaner always on and thereby minimize power consumption and mechanical wear and tear.

Remote identification of dust accumulation is not an easy task. Even though power output could be used as a proxy for dust accumulation, it does not work always because power output can experience significant fluctuation during the daytime due to variation in sunlight, overcast sky etc. Therefore, the only reliable way to track dust accumulation remotely is to make use of a dust fouling tracking device. Even though there are several ways in which we can do that, such as infrared particulate detector, we resort to an optical tracker, which is a retrofit camera. We collect images of solar panel at a sampling location periodically and use those images to predict if there is significant dust accumulation or not. The solar panel cleaning mechanism can be operated using the feedback from optical tracker.

## 7.2. Optical tracker using USB microscope camera

We designed an optical tracker system for the electrostatic solar panel cleaner using a retrofit USB powered microscope camera as shown in Figure 7-1 (left). The camera has a built-in light source and has magnification range of 50x-1000x. Figure 7-1 (right) shows the zoomed in microscopic image of dust particles of average size 150 microns that fouls a 10cmx15cm sized mini solar panel. The camera can easily visualize particles as small as 10 microns and therefore can be used for all practical dust particle detection purposes. By connecting the camera to a PC via USB, the pictures can be captured at desired frequency.

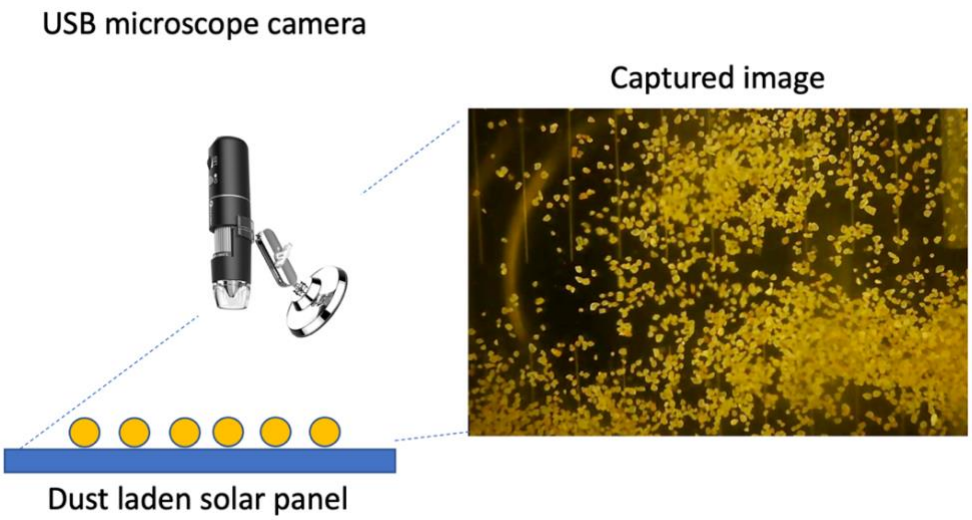


Figure 7-1. **Dust particle tracking.** USB camera for tracking dust particles (left) and images of dust particles of size 150 um accumulated on solar panel

## 7.3. Machine Learning Framework: General

Even though visualizing really tiny particles is possible with the microscopic camera, predicting the presence of dust particles is extremely hard with conventional image processing algorithms. One of the conventional ways to predict dust accumulation is to perform Otsu's thresholding (an image processing algorithm) to make the image binary and then perform image analysis to predict the percentage area of the surface covered by dust particles. We could manually define a cut-off for dust fraction on the surface above which solar panel cleaner is operated. However, this is quite cumbersome to implement in practice because thresholding is heavily dependent on factors such as background lighting, brightness and contrast of the image, particle distribution, background reflection from the solar panel etc. Therefore, an automatic image processing using conventional algorithms will have poor accuracy to predict presence or absence of dust. Therefore, we make use of Machine Learning techniques to perform the hard task of particle identification.

Within machine learning, there are quite a lot of techniques available for performing classification tasks such as Support Vector Machines (SVM), Decision Trees, K-Nearest Neighbor (KNN), Artificial Neural Networks (ANN), Convolutional Neural Networks (CNN) etc. Among these we make use of Convolutional Neural Networks (CNN) for performing image classification

because it is much more robust for classification task, especially for dataset in the form of images. There are also plenty of pre-trained (trained on millions of images) neural networks that we can import and train on our dataset to have superior image classification accuracy compared to any other methods.

Convolutional Neural Network takes the tensor representation of the images as input into their input layer. There are one of multiple hidden layers within the CNN. And at the end there is one output layer where the CNN predicts the class of the image.

In our particular case, there are two types of predictions that we are interested in. Firstly, we would like to know if there is dust or not on solar panels, regardless of the particle size or distribution. Thus, this becomes a binary classification problem. Knowing the presence of dust particles on solar panels is useful to decide when to switch on the dust removal mechanism. The second prediction capability that we are interested in is for us to be able to know the size of the particles that foul solar panels. In previous reports we saw that for each dust particle size distribution of a mean size, there is a characteristic voltage for a certain electrode configuration called as the dust removal voltage, Even though the dust particles that foul solar panels can range in size from anywhere between 10 microns to 400 microns, we can split this range into windows of particle sizes with different mean values, and predict in which window is the current dust particle fouling occurring.

## 7.4. Image classification using Convolutional Neural Network (CNN)

### 7.4.1. Image acquisition

Typically, training the neural network need hundreds to thousands of images per class for effective classification depending on the similarity between different classes. For creating a large dataset of images, we spread dust particles on mini solar panel in different configurations and record a video of dust fouling using the mini-USB camera by attaching the camera to the 2D translation mechanism we discussed in the earlier report. Then we convert the video into screenshots. Since the recording speed is 30 frames per second, we save once in every 5 frames of the video as images to the dataset folder. That way a 20 second video that captures different regions

of the solar panel to cover various fouling conditions effectively generates more that 100 pictures. We repeat the procedure for various dust particle mean sizes ranging from 10 microns to 340 microns and generate a dataset of thousands of images classified into different folders based on the mean size of dust particle distribution as shown in Figure 7-2.

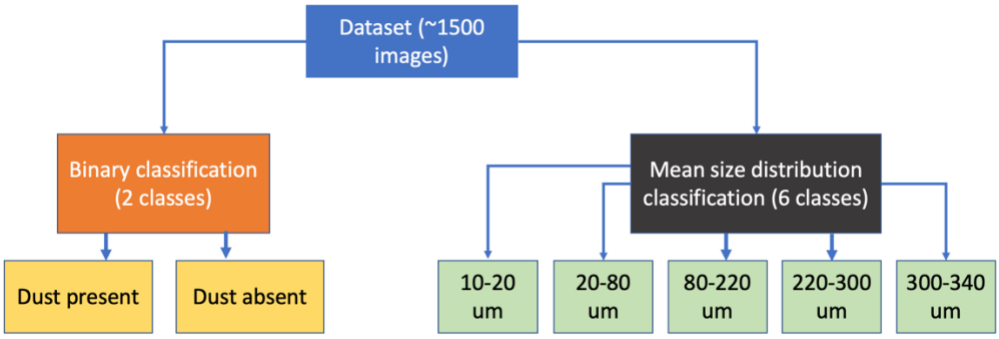


Figure 7-2: **Data classification**

Since images in our dataset are very standard, meaning the background is the top surface of solar panel, there is not much standardization to be performed on the images. The only preprocessing we do on the images are certain transformation such as random rotational transformation and random crop. The cropping also helps to speed up the CNN training due to reduction of the overall size of the image dataset. We select resnet as our neural network as it has shown to have superior performance in image classification tasks. The general architecture (input, hidden, convolution and output layers) of resnet is shown in Figure 7-3.

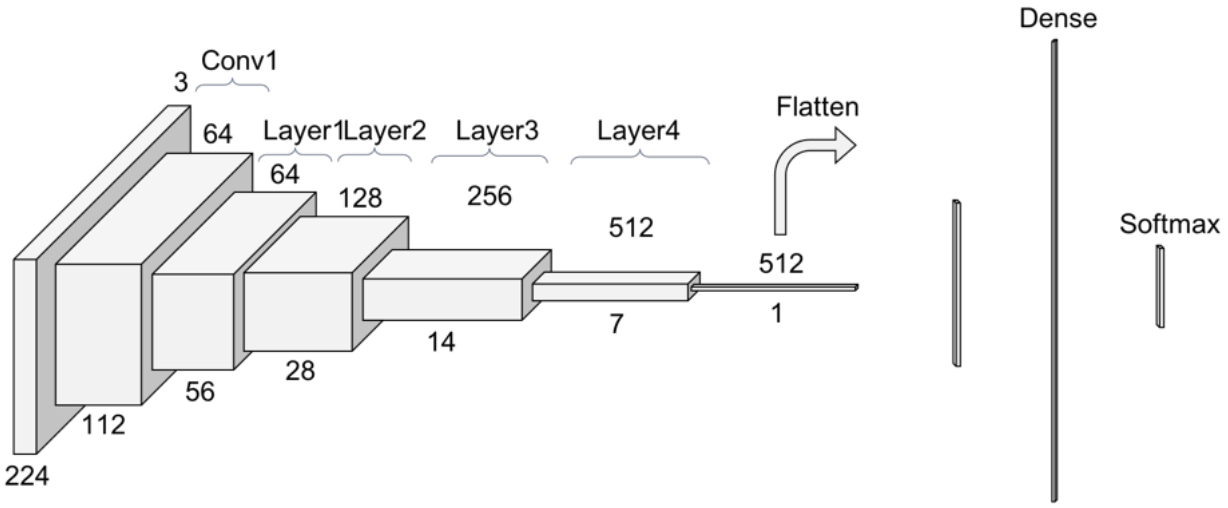


Figure 7-3: **General architecture of resnet**

### 7.4.2. Train-test data split

The collection of our data (images of dust fouling) has to be divided into three categories. Training data, testing data and validation data. Validation dataset could be relatively smaller in size. However, it is critical to decide the relative split of train and test dataset for obtaining high accuracy. Too much training data and too less testing could result in overfitting. Too less training data can result in poor training of the biases and weights in the neural network. Since there is no thumb-rule for selecting an exact train-test data split we choose a 70:30 split. We use pretrained resnet with 34 hidden layers (also known as renset34).

### 7.4.3. Number of epochs

Number of epochs cannot be too large or too less to avoid over or undertraining. We selected an epoch number of 12 based on trial and error. We also take into consideration the relative training and validation loss for determining the optimum number of epochs for training as shown in Figure 7-4. It can be seen that both training and validation losses reduces with epochs, suggesting that neural network gets better at predicting. At 12 epochs, we observe that training and validation losses slowly start to diverge, suggesting that increasing the number of epochs even further could result in overtraining.


Figure 7-4: **Training and validation loss as a function of epochs**

## 7.5. Prediction of dust particle mean size distribution

The first set of experiments we do on the dataset is training the neural network on dust particle sizes classified into different mean size distributions. Figure 7-5 shows the variation of error rate with epochs. It is clear that as the CNN gets trained multiple times with randomized data, the error rate is decreasing.

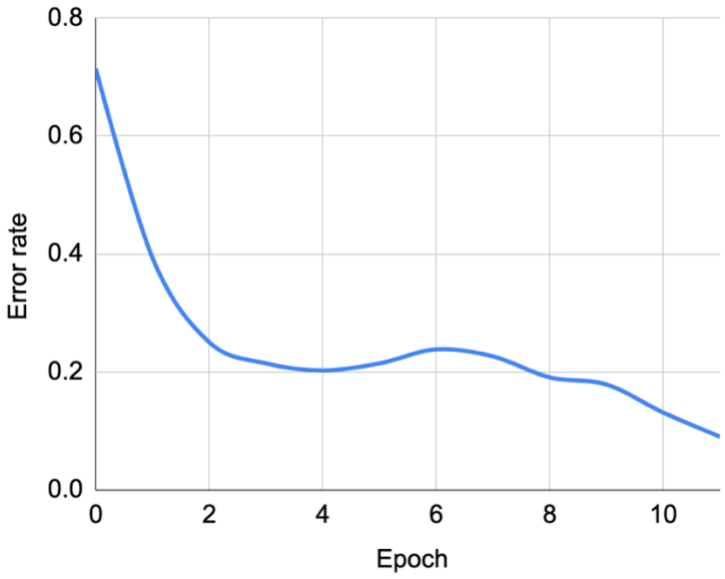


Figure 7-5: **Decreasing error rate as increasing number of epochs**

Figure 7-6 shows the prediction accuracy change with more epochs of training. It can be seen that even with resnet of 34 layers, <5 epochs give a maximum training accuracy of ~75%. However, even though it takes longer to train for 12 epochs, the prediction accuracy for dust particle mean size classification increases to >90% at the end of 12 epochs.

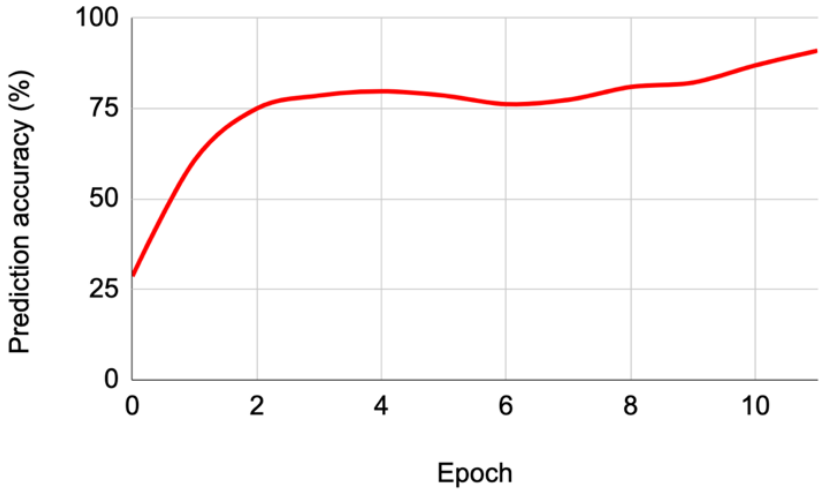


Figure 7-6: **Prediction accuracy approaches >90% for multi-class classification**

### 7.5.1. Prediction accuracy of binary classification

Figure 7-7 shows the prediction accuracy of binary and multi-class (mean-size) classification. Obviously, binary classification is easier because it is much easier to predict the presence or absence of dust particles compared to the relative difference between two particle size distributions. Therefor it can be seen that the prediction accuracy presence or absence of dust is >99%. In the dust particle size distribution, there is a lot of overlap between two different classes. For example, a 10-20 microns dust distribution means that 90% of the particles fall withing that range (by weight). However, there will be lot of particles >20 microns and <10 microns in this size distribution. This combined with multi-particle effects makes the images of 10-20 and 20-40 microns dust particle distribution appear pretty much the same for human eye from the microscope images. The CNN is able to identify differences, and results in a prediction accuracy >90%, albeit lower than the case of binary classification.

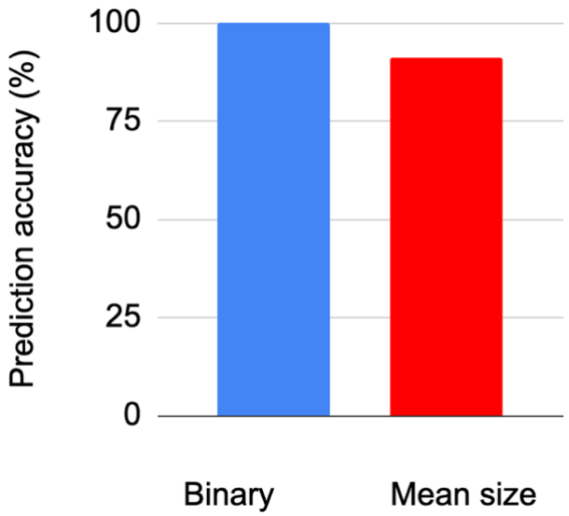


Figure 7-7: **Prediction accuracy for binary and multi-class classification**

### 7.5.2. Dust fouling library

In order to increasing the accuracy of multi-class classification, there are two tasks to be performed. (1) Fine tuning the neural network training by incorporating more hidden layers, dropout layer and other specific algorithms meant for particle detection and (2) Gathering more training data by expanding the fouling library. Currently we have ~100-200 images per class. If we expand that by an order of magnitude, the prediction accuracy of CNN will tremendously improve. Also expanding the fouling image library by capturing various fouling configuration of dust particles will also cover different physical conditions such as sandstorms (heavy particle fouling) and airborne particle fouling (light particle fouling as shown in Figure 7-8.

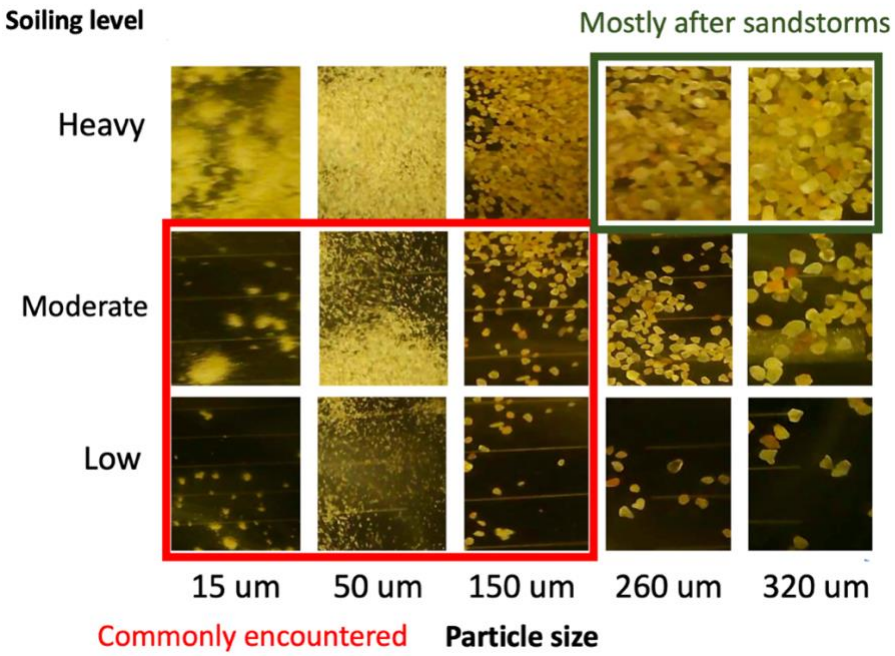


Figure 7-8: **A snapshot of sample images from our dust fouling library**. We create a library of dust particle fouling conditions by varying the dust particle size and the level of fouling. In this figure we show a sample of images from our dust fouling library.

The final aspect of expanding the dust fouling library is incorporating microscope images of wetted on dried particles. Wetting of the surface of solar panel and subsequent drying can result in formation of patterns of particles depending on the surface chemistry and texture. Thus, there are far more varieties of fouling patterns possible with dust particles of different sizes than what is possible with random distribution.

### 7.5.3. System level design

Figure 7-9 shows the system level design of electrostatic dust removal system we design. In step 1, USB microscope camera captures the pictures of solar panel at a constant frequency (once if few minutes). In step 2 the captured images are constantly fed to resnet34 neural network that we trained already with high prediction accuracy. In step 3, the neural network performs 2 predictions. One is the presence or absence of particles. Two is the mean size. If absence of dust is detected, there is no further action. But in presence of dust particles of certain mean size, in step 4 arduino is controlled signaled. In step 5 the Arduino triggers dust removal mechanism to repel dust.

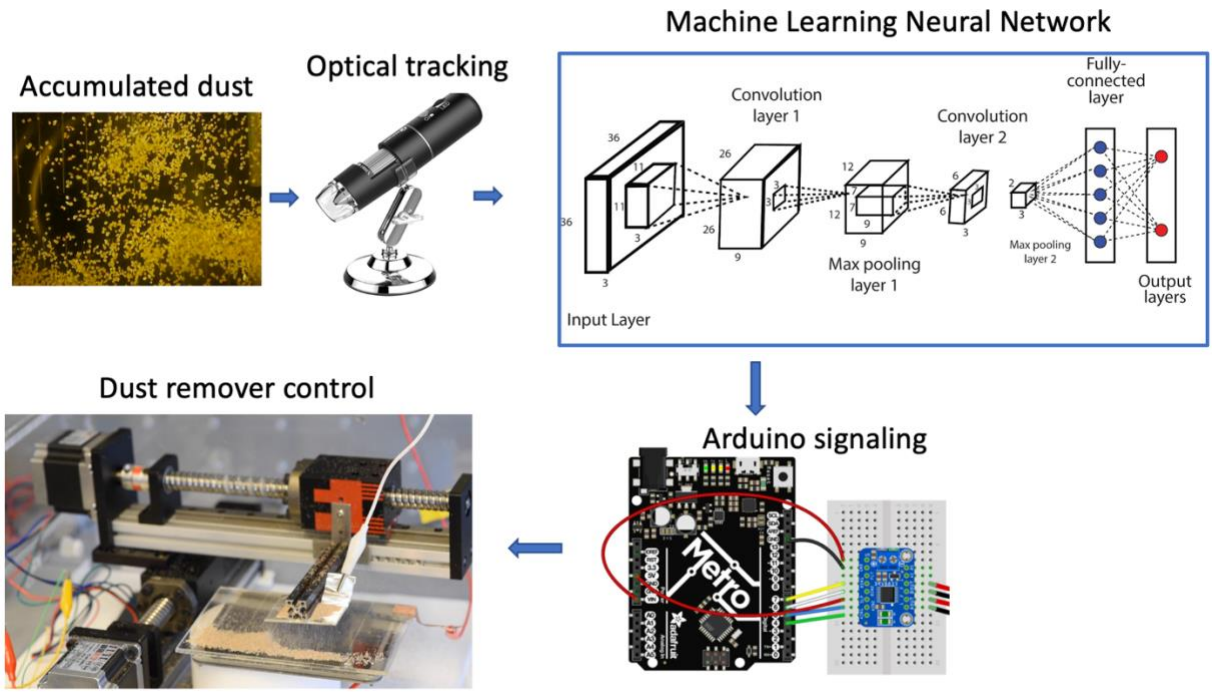


Figure 7-9: **System level design**

# 8. Bibliography


1. Electric power consumption (kWh per capita) | Data. Available at: https://data.worldbank.org/indicator/EG.USE.ELEC.KH.PC. (Accessed: 8th September 2022)
2. Ritchie, H., Roser, M. & Rosado, P. Energy. *Our World Data* (2020).
3. Electricity Mix - Our World in Data. Available at: https://ourworldindata.org/electricity-mix. (Accessed: 8th September 2022)
4. Davies, J.T., Rideal, E. K. *Interfacial Phenomena*. (1961).
5. Energy Agency, I. *The IEA examines the full spectrum of energy issues including oil*. (2018).
6. Ilse, K. *et al.* Techno-Economic Assessment of Soiling Losses and Mitigation Strategies for Solar Power Generation. *Joule* **3**, 2303–2321 (2019).
7. Yilbas, B. S. *et al.* Influence of dust and mud on the optical, chemical, and mechanical properties of a pv protective glass. *Sci. Rep.* **5**, 1–12 (2015).
8. Cordero, R. R. *et al.* Effects of soiling on photovoltaic (PV) modules in the Atacama Desert. *Sci. Rep.* **8**, 1–14 (2018).
9. Maghami, M. R. *et al.* Power loss due to soiling on solar panel: A review. *Renewable and Sustainable Energy Reviews* **59**, 1307–1316 (2016).
10. Mani, M. & Pillai, R. Impact of dust on solar photovoltaic (PV) performance: Research status, challenges and recommendations. *Renew. Sustain. Energy Rev.* **14**, 3124–3131 (2010).
11. Sarver, T., Al-Qaraghuli, A. & Kazmerski, L. L. A comprehensive review of the impact of dust on the use of solar energy: History, investigations, results, literature, and mitigation approaches. *Renew. Sustain. Energy Rev.* **22**, 698–733 (2013).
12. Ilse, K. K., Figgis, B. W., Naumann, V., Hagendorf, C. & Bagdahn, J. Fundamentals of soiling processes on photovoltaic modules. *Renew. Sustain. Energy Rev.* **98**, 239–254 (2018).
13. Sayyah, A., Horenstein, M. N. & Mazumder, M. K. Mitigation of soiling losses in

concentrating solar collectors. *Conf. Rec. IEEE Photovolt. Spec. Conf.* 480–485 (2013). doi:10.1109/PVSC.2013.6744194

14. Sayyah, A., Horenstein, M. N. & Mazumder, M. K. Energy yield loss caused by dust deposition on photovoltaic panels. *Sol. Energy* **107**, 576–604 (2014).
15. Jones, R. K. *et al.* Optimized Cleaning Cost and Schedule Based on Observed Soiling Conditions for Photovoltaic Plants in Central Saudi Arabia. *IEEE J. Photovoltaics* **6**, 730–738 (2016).
16. Cohen Gilbert E., Kearney, D. W. & Kolb, G. J. *Final Report on the Operation and Maintenance Improvement Program for Concentrating Solar Power Plants*. (1999). doi:10.2172/8378
17. Panat, S. & Varanasi, K. K. Electrostatic dust removal using adsorbed moisture–assisted charge induction for sustainable operation of solar panels. *Sci. Adv.* **8**, 78 (2022).
18. Barron, M. G. Ecological Impacts of the Deepwater Horizon Oil Spill: Implications for Immunotoxicity. *Toxicol. Pathol.* **40**, 315–320 (2012).
19. Shannon, M. A. *et al.* Science and technology for water purification in the coming decades. *Nat. 2008 4527185* **452**, 301–310 (2008).
20. Guha, I. F. & Varanasi, K. K. Separating nanoscale emulsions: Progress and challenges to date. *Current Opinion in Colloid and Interface Science* **36**, 110–117 (2018).
21. Fakhru'l-Razi, A. *et al.* Review of technologies for oil and gas produced water treatment. *J. Hazard. Mater.* **170**, 530–551 (2009).
22. Cherukupally, P. *et al.* Surface-engineered sponges for recovery of crude oil microdroplets from wastewater. *Nat. Sustain. 2019 32* **3**, 136–143 (2019).
23. Veil, J. A., Puder, M. G., Elcock, D. & Redweik, R. J., Jr. A white paper describing produced water from production of crude oil, natural gas, and coal bed methane. (2004). doi:10.2172/821666
24. Dudek, M., Kancir, E. & Øye, G. Influence of the Crude Oil and Water Compositions on the Quality of Synthetic Produced Water. *Energy and Fuels* **31**, 3708–3716 (2017).
25. Fakhru'l-Razi, A. *et al.* Review of technologies for oil and gas produced water treatment. *Journal of Hazardous Materials* **170**, 530–551 (2009).
26. Kokal, S. & Aramco, S. *Crude-Oil Emulsions: A State-Of-The-Art Review*. (2005).

27. Wong, S. F., Lim, J. S. & Dol, S. S. Crude oil emulsion: A review on formation, classification and stability of water-in-oil emulsions. *J. Pet. Sci. Eng.* **135**, 498–504 (2015).
28. Saad, M. A., Kamil, M., Abdurahman, N. H., Yunus, R. M. & Awad, O. I. An Overview of Recent Advances in State-of-the-Art Techniques in the Demulsification of Crude Oil Emulsions. *Processes* **7**, 470 (2019).
29. Kilpatrick, P. K. Water-in-Crude Oil Emulsion Stabilization: Review and Unanswered Questions. *Energy and Fuels* **26**, 4017–4026 (2012).
30. Mhatre, S. *et al.* Electrostatic phase separation: A review. *Chemical Engineering Research and Design* **96**, 177–195 (2015).
31. Kang, W. *et al.* Demulsification performance, behavior and mechanism of different demulsifiers on the light crude oil emulsions. *Colloids Surfaces A Physicochem. Eng. Asp.* **545**, 197–204 (2018).
32. Salam, K. K., Alade, A. O., Arinkoola, A. O. & Opawale, A. Improving the Demulsification Process of Heavy Crude Oil Emulsion through Blending with Diluent. *J. Pet. Eng.* **2013**, (2013).
33. Henderson, S. B., Grigson, S. J. W., Johnson, P. & Roddie, B. D. Potential Impact of Production Chemicals on the Toxicity of Produced Water Discharges from North Sea Oil Platforms. *Mar. Pollut. Bull.* **38**, 1141–1151 (1999).
34. Dalmazzone, C. & Noïk, C. Development of New green Demulsifiers for Oil Production. *SPE Int. Oilf. Chem. Symp. Proc.* 1–9 (2001). doi:10.2118/65041-MS
35. Energy Agency, I. Global Energy Review: CO2 Emissions in 2021 Global emissions rebound sharply to highest ever level. (2021).
36. CO2 emissions - Our World in Data. Available at: https://ourworldindata.org/co2-emissions. (Accessed: 14th October 2021)
37. AR5 Climate Change 2014: Mitigation of Climate Change — IPCC. Available at: https://www.ipcc.ch/report/ar5/wg3/. (Accessed: 14th October 2021)
38. AVoided Emissions and geneRation Tool (AVERT) | US EPA. Available at: https://www.epa.gov/avert. (Accessed: 14th October 2021)
39. Epa, U. & Change Division, C. Inventory of U.S. Greenhouse Gas Emissions and Sinks: 1990-2019 – Main Text - Corrected Per Corrigenda, Updated 05/2021. (1990).

40. Notz, R. J., Tönnies, I., McCann, N., Scheffknecht, G. & Hasse, H. CO2 Capture for Fossil Fuel-Fired Power Plants. *Chem. Eng. Technol.* **34**, 163–172 (2011).
41. Chao, C., Deng, Y., Dewil, R., Baeyens, J. & Fan, X. Post-combustion carbon capture. *Renew. Sustain. Energy Rev.* **138**, 110490 (2021).
42. Yang, J., Yu, X., Yan, J. & Tu, S. T. CO2 capture using amine solution mixed with ionic liquid. *Ind. Eng. Chem. Res.* **53**, 2790–2799 (2014).
43. Guo, H., Li, C., Shi, X., Li, H. & Shen, S. Nonaqueous amine-based absorbents for energy efficient CO2 capture. *Appl. Energy* **239**, 725–734 (2019).
44. Dutcher, B., Fan, M. & Russell, A. G. Amine-based CO2 capture technology development from the beginning of 2013-A review. *ACS Appl. Mater. Interfaces* **7**, 2137–2148 (2015).
45. Mohd Shariff, A. *et al.* Factors affecting CO2 absorption efficiency in packed column: A review Author's personal copy Review Factors affecting CO 2 absorption efficiency in packed column: A review. doi:10.1016/j.jiec.2012.05.013
46. Iso, Y., Huang, J., Kato, M., Matsuno, S. & Takano, K. Numerical and Experimental Study on Liquid Film Flows on Packing Elements in Absorbers for Post-combustion CO2 Capture. *Energy Procedia* **37**, 860–868 (2013).
47. Singh, R. K., Galvin, J. E. & Sun, X. Multiphase flow studies for microscale hydrodynamics in the structured packed column. *Chem. Eng. J.* **353**, 949–963 (2018).
48. Sebastia-Saez, D., Gu, S., Ranganathan, P. & Papadikis, K. Micro-scale CFD modeling of reactive mass transfer in falling liquid films within structured packing materials. *Int. J. Greenh. Gas Control* **33**, 40–50 (2015).
49. Agbonghae, E. O., Hughes, K. J., Ingham, D. B., Ma, L. & Pourkashanian, M. Optimal Process Design of Commercial-Scale Amine-Based CO2 Capture Plants. *Ind. Eng. Chem. Res.* **53**, 14815–14829 (2014).
50. Husebye, J., Brunsvold, A. L., Roussanaly, S. & Zhang, X. Techno Economic Evaluation of Amine based CO2 Capture: Impact of CO2 Concentration and Steam Supply. *Energy Procedia* **23**, 381–390 (2012).
51. Liu, H., Consoli, C. & Zapantis, A. Overview of Carbon Capture and Storage (CCS) Facilities Globally. *SSRN Electron. J.* (2018). doi:10.2139/SSRN.3366353
52. GLOBAL STATUS OF CCS 2020.

53. World Energy Outlook 2020 – Analysis - IEA. Available at: https://www.iea.org/reports/world-energy-outlook-2020. (Accessed: 5th August 2022)
54. Jäger-Waldau, A. Snapshot of Photovoltaics—February 2019. *Energies* **12**, 769 (2019).
55. Energy Information Administration, U. *International Energy Outlook 2019*. (2019).
56. International Energy Agency. *Trends in photovoltaic applications*. *Survey report of selected IEA countries between 1992 and 2011* (2019). doi:10.1021/ac50054a041
57. Comello, S., Reichelstein, S. & Sahoo, A. The road ahead for solar PV power. *Renewable and Sustainable Energy Reviews* **92**, 744–756 (2018).
58. Nayak, P. K., Mahesh, S., Snaith, H. J. & Cahen, D. Photovoltaic solar cell technologies: analysing the state of the art. *Nat. Rev. Mater.* **4**, 269–285 (2019).
59. Raut, H. K., Ganesh, V. A., Nair, A. S. & Ramakrishna, S. Anti-reflective coatings: A critical, in-depth review. *Energy and Environmental Science* **4**, 3779–3804 (2011).
60. Sargunanathan, S., Elango, A. & Mohideen, S. T. Performance enhancement of solar photovoltaic cells using effective cooling methods: A review. *Renewable and Sustainable Energy Reviews* **64**, 382–393 (2016).
61. Rodríguez-Gallegos, C. D. *et al.* Global Techno-Economic Performance of Bifacial and Tracking Photovoltaic Systems. *Joule* **4**, 1514–1541 (2020).
62. Battaglia, C. *et al.* Nanoimprint lithography for high-efficiency thin-film silicon solar cells. *Nano Lett.* **11**, 661–665 (2011).
63. Rahman, A. *et al.* Sub-50-nm self-assembled nanotextures for enhanced broadband antireflection in silicon solar cells. *Nat. Commun.* **6**, (2015).
64. Sarver, T., Al-Qaraghuli, A. & Kazmerski, L. L. A comprehensive review of the impact of dust on the use of solar energy: History, investigations, results, literature, and mitigation approaches. *Renewable and Sustainable Energy Reviews* **22**, 698–733 (2013).
65. Parrott, B., Carrasco Zanini, P., Shehri, A., Kotsovos, K. & Gereige, I. Automated, robotic dry-cleaning of solar panels in Thuwal, Saudi Arabia using a silicone rubber brush. *Sol. Energy* **171**, 526–533 (2018).
66. Sansom, C. *et al.* Soiling and cleaning of polymer film solar reflectors. *Energies* **9**, (2016).
67. Mazumder, M. K. *et al.* Self-cleaning transparent dust shields for protecting solar panels and other devices. *Part. Sci. Technol.* **25**, 5–20 (2007).

68. Calle, C. I., Buhler, C. R., McFall, J. L. & Snyder, S. J. Particle removal by electrostatic and dielectrophoretic forces for dust control during lunar exploration missions. *J. Electrostat.* **67**, 89–92 (2009).
69. Kawamoto, H. & Shibata, T. Electrostatic cleaning system for removal of sand from solar panels. *J. Electrostat.* **73**, 65–70 (2015).
70. Kawamoto, H. Electrostatic cleaning equipment for dust removal from soiled solar panels. *J. Electrostat.* **98**, 11–16 (2019).
71. Calle, C. I., Mcfall, J. L., Buhler, C. R., Snyder, S. J. & Arens, E. E. Dust Particle Removal by Electrostatic and Dielectrophoretic Forces with Applications to NASA Exploration Missions. *ESA Annu. Meet. Electrost.* 1 (2008).
72. Calle, C. I., Buhler, C. R., Johansen, M. R., Hogue, M. D. & Snyder, S. J. Active dust control and mitigation technology for lunar and Martian exploration. *Acta Astronaut.* **69**, 1082–1088 (2011).
73. Mazumder, M. *et al.* Characterization of electrodynamic screen performance for dust removal from solar panels and solar hydrogen generators. *IEEE Trans. Ind. Appl.* **49**, 1793–1800 (2013).
74. Mazumder, M. K. US Patent No: US 9,433,336 B2, Self-cleaning solar panels and concentrators with transparent electrodynamic screens. (2016).
75. Yilbas, B. S. *et al.* Characterization of Environmental Dust in the Dammam Area and Mud After-Effects on Bisphenol-A Polycarbonate Sheets. *Sci. Rep.* **6**, 1–14 (2016).
76. Husar, R. B. Intercontinental Transport of Dust: Historical and Recent Observational Evidence. *Handb. Environ. Chem.* **4**, 277–294 (2004).
77. Orange, D., Gac, J. Y. & Diallo, M. I. Geochemical assessment of atmospheric deposition including Harmattan dust in continental West Africa. *Tracers Hydrol. Proc. Int. Symp. Yokohama, 1993* 303–312 (1993).
78. Sun, J. & Besant, R. W. Heat and mass transfer during silica gel-moisture interactions. *Int. J. Heat Mass Transf.* **48**, 4953–4962 (2005).
79. Anderson, J. H., Parks, G. A. & Anderson1, J. H. The Electrical Conductivity of Silica Gel in the Presence of Adsorbed Water. *J. Phys. Chem.* (1968).
80. Zhang, Y. *et al.* Electric field and humidity trigger contact electrification. *Phys. Rev. X* **5**,

1–9 (2015).

81. Jones, R., Pollock, H. M., Cleaver, J. A. S. & Hodges, C. S. Adhesion forces between glass and silicon surfaces in air studied by AFM: Effects of relative humidity, particle size, roughness, and surface treatment. *Langmuir* **18**, 8045–8055 (2002).
82. Heim, L.-O., Blum, J., Preuss, M. & Butt, H.-J. Adhesion and Friction Forces between Spherical Micrometer-Sized Particles. *Phys. Rev. Lett.* **83**, (1999).
83. Farshchi-Tabrizi, M., Kappl, M., Cheng, Y., Gutmann, J. & Butt, H.-J. On the adhesion between fine particles and nanocontacts: an atomic force microscope study. *Langmuir* **22**, 2171–2184 (2006).
84. Hamaker, H. C. The London—van der Waals attraction between spherical particles. *Physica* **4**, 1058–1072 (1937).
85. Rabinovich, Y. I., Adler, J. J., Ata, A., Singh, R. K. & Moudgil, B. M. Adhesion between Nanoscale Rough Surfaces. *J. Colloid Interface Sci.* **232**, 17–24 (2000).
86. Haus Melcher James R, H. A. *Electromagnetic Fields and Energy*.
87. Bishop, K. J. M., Drews, A. M., Cartier, C. A., Pandey, S. & Dou, Y. Contact Charge Electrophoresis: Fundamentals and Microfluidic Applications. *Langmuir* **34**, 6315–6327 (2018).
88. Israelachvili, J. N. Van der Waals Forces between Particles and Surfaces. *Intermol. Surf. Forces* 253–289 (2011). doi:10.1016/B978-0-12-375182-9.10013-2
89. Rodriguez, R. D., Lacaze, E. & Jupille, J. Probing the probe: AFM tip-profiling via nanotemplates to determine Hamaker constants from phase–distance curves. *Ultramicroscopy* **121**, 25–30 (2012).
90. Jones, R., Pollock, H. M., Cleaver, J. A. S. & Hodges, C. S. Adhesion forces between glass and silicon surfaces in air studied by AFM: Effects of relative humidity, particle size, roughness, and surface treatment. *Langmuir* **18**, 8045–8055 (2002).
91. Rumpf, H. & Bull, F. A. *Particle technology*. (Chapman and Hall, 1990).
92. Ramakrishna, S. N., Clasohm, L. Y., Rao, A. & Spencer, N. D. Controlling adhesion force by means of nanoscale surface roughness. *Langmuir* **27**, 9972–9978 (2011).
93. Beach, E. R., Tormoen, G. W., Drelich, J. & Han, R. Pull-off force measurements between rough surfaces by atomic force microscopy. *J. Colloid Interface Sci.* **247**, 84–99 (2002).

94. van Zwol, P. J., Palasantzas, G. & Th De Hosson, J. M. Influence of random roughness on the adhesion between metal surfaces due to capillary condensation. (1019). doi:10.1063/1.2768919
95. J, G.-C. *et al.* Dew condensation on desert beetle skin. *Eur. Phys. J. E. Soft Matter* **37**, (2014).
96. Nayshevsky, I., Xu, Q. & Lyons, A. Literature Survey of Dust Particle Dimensions on Soiled Solar Panel Modules. **3**, (2020).
97. Bohren, C. F. & Huffman, D. R. Absorption and Scattering of Light by Small Particles. *Absorpt. Scatt. Light by Small Part.* (1998). doi:10.1002/9783527618156
98. Guo, H. *et al.* Effect of ITO film deposition conditions on ITO and CdS films of semiconductor solar cells. *Optik (Stuttg).* **140**, 322–330 (2017).
99. Khachatryan, H., Kim, D. J., Kim, M. & Kim, H. K. Roll-to-Roll fabrication of ITO thin film for flexible optoelectronics applications: The role of post-annealing. *Mater. Sci. Semicond. Process.* **88**, 51–56 (2018).
100. PTI. *Arizona Test Dust (ATD) Safety Data Sheet*. (2016).
101. Ilse, K. *et al.* Techno-Economic Assessment of Soiling Losses and Mitigation Strategies for Solar Power Generation. *Joule* (2019). doi:10.1016/j.joule.2019.08.019
102. Yilbas, B. S. *et al.* Influence of dust and mud on the optical, chemical, and mechanical properties of a pv protective glass. *Sci. Rep.* **5**, (2015).
103. Li, X., Mauzerall, D. L. & Bergin, M. H. Global reduction of solar power generation efficiency due to aerosols and panel soiling. *Nat. Sustain.* **3**, 720–727 (2020).
104. Calle, C. I. *et al. Dust Particle Removal by Electrostatic and Dielectrophoretic Forces with Applications to NASA Exploration Missions*. (2008).
105. Fan, S. K. & Wang, F. M. Multiphase optofluidics on an electro-microfluidic platform powered by electrowetting and dielectrophoresis. *Lab Chip* **14**, 2728–2738 (2014).
106. Trigwell, S., Grable, N., Yurteri, C. U., Sharma, R. & Mazumder, M. K. Effects of surface properties on the tribocharging characteristics of polymer powder as applied to industrial processes. *IEEE Trans. Ind. Appl.* **39**, 79–86 (2003).
107. Johnson, K. L., Kendall, K. & Roberts, A. D. Surface Energy and the Contact of Elastic Solids. *Proc. R. Soc. A Math. Phys. Eng. Sci.* **324**, 301–313 (1971).

108. Israelachvili, J. *Intermolecular and Surface Forces*. *Intermolecular and Surface Forces* (2011). doi:10.1016/C2009-0-21560-1
109. Derjaguin, B. V., Muller, V. M. & Toporov, Y. P. Effect of contact deformations on the adhesion of particles. *J. Colloid Interface Sci.* **53**, 314–326 (1975).
110. Adrian Parsegian, V. Van der Waals forces: A handbook for biologists, chemists, engineers, and physicists. *Van Der Waals Forces A Handb. Biol. Chem. Eng. Phys.* 1–380 (2005). doi:10.1017/CBO9780511614606
111. Heckenthaler, T. *et al.* Self-Cleaning Mechanism: Why Nanotexture and Hydrophobicity Matter. *Langmuir* **35**, 15526–15534 (2019).
112. Jones, R., Pollock, H. M., Cleaver, J. A. S. & Hodges, C. S. Adhesion Forces between Glass and Silicon Surfaces in Air Studied by AFM : Effects of Relative Humidity , Particle Size , Roughness , and Surface Treatment. 8045–8055 (2002).
113. Pan, C. *et al.* Fabrication of micro-texture channel on glass by laser-induced plasma-assisted ablation and chemical corrosion for microfluidic devices. *J. Mater. Process. Technol.* **240**, 314–323 (2017).
114. Beach, E. R., Tormoen, G. W., Drelich, J. & Han, R. Pull-off Force Measurements between Rough Surfaces by Atomic Force Microscopy. **99**, 84–99 (2002).
115. Zhang, X., Wang, L. & Levänen, E. Superhydrophobic surfaces for the reduction of bacterial adhesion. *RSC Adv.* **3**, 12003–12020 (2013).
116. Said, S. A. M., Al-Aqeeli, N. & Walwil, H. M. The potential of using textured and anti-reflective coated glasses in minimizing dust fouling. *Sol. Energy* **113**, 295–302 (2015).
117. Ijaola, A. O. *et al.* Wettability Transition for Laser Textured Surfaces: A Comprehensive Review. *Surfaces and Interfaces* **21**, 100802 (2020).
118. Wu, Z., Bao, H., Xing, Y. & Liu, L. Tribological characteristics and advanced processing methods of textured surfaces: a review. *Int. J. Adv. Manuf. Technol. 2021 1145* **114**, 1241–1277 (2021).
119. Tan, C. L. C., Gao, S., Wee, B. S., Asa-Awuku, A. & Thio, B. J. R. Adhesion of dust particles to common indoor surfaces in an air-conditioned environment. *Aerosol Sci. Technol.* **48**, 541–551 (2014).
120. Levinson, H. J. Principles of lithography.

121. Allen, T., Bullock, J., Cuevas, A., Baker-Finch, S. & Karouta, F. Reactive ion etched black silicon texturing: A comparative study. *2014 IEEE 40th Photovolt. Spec. Conf. PVSC 2014* 562–566 (2014). doi:10.1109/PVSC.2014.6924983
122. Butt, H. J., Cappella, B. & Kappl, M. Force measurements with the atomic force microscope: Technique, interpretation and applications. *Surf. Sci. Rep.* **59**, 1–152 (2005).
123. Spierings, G. A. C. M. Wet chemical etching of silicate glasses in hydrofluoric acid based solutions. *J. Mater. Sci. 1993 2823* **28**, 6261–6273 (1993).
124. Znaidi, L. *et al.* AZO Thin Films by Sol-Gel Process for Integrated Optics. *Coatings 2013, Vol. 3, Pages 126-139* **3**, 126–139 (2013).
125. Fernandes, G. E., Kim, J. H. & Xu, J. Sol-gel synthesis and thermoelectric properties of AZO films with pyrolytic carbon inclusions. *Superlattices Microstruct.* **109**, 161–169 (2017).
126. Huang, Z. Q., Hong, M. H., Do, T. B. M. & Lin, Q. Y. Laser etching of glass substrates by 1064 nm laser irradiation. *Appl. Phys. A 2008 931* **93**, 159–163 (2008).
127. Infante, D. *et al.* Durable, superhydrophobic, antireflection, and low haze glass surfaces using scalable metal dewetting nanostructuring. *Nano Res. 2013 66* **6**, 429–440 (2013).
128. Fingas, M. & Fieldhouse, B. Formation of water-in-oil emulsions and application to oil spill modelling. *J. Hazard. Mater.* **107**, 37–50 (2004).
129. Nordvik, A. B., Simmons, J. L., Bitting, K. R., Lewis, A. & Strøm-Kristiansen, T. Oil and water separation in marine oil spill clean-up operations. *Spill Sci. Technol. Bull.* **3**, 107–122 (1996).
130. Schrope, M. Oil spill: Deep wounds. *Nature* **472**, 152–154 (2011).
131. Solomon, B. R., Hyder, M. N. & Varanasi, K. K. Separating Oil-Water Nanoemulsions using Flux-Enhanced Hierarchical Membranes. *Sci. Reports 2014 41* **4**, 1–6 (2014).
132. Mannu, A., Garroni, S., Porras, J. I. & Mele, A. Available Technologies and Materials for Waste Cooking Oil Recycling. *Process. 2020, Vol. 8, Page 366* **8**, 366 (2020).
133. Zhang, H., Aytun Ozturk, U., Wang, Q. & Zhao, Z. Biodiesel produced by waste cooking oil: Review of recycling modes in China, the US and Japan. *Renew. Sustain. Energy Rev.* **38**, 677–685 (2014).
134. Jacobs, R. P. W. M., Grant, R. O. H., Kwant, J., Marquenie, J. M. & Mentzer, E. The

Composition of Produced Water from Shell Operated Oil and Gas Production in the North Sea. *Prod. Water* 13–21 (1992). doi:10.1007/978-1-4615-2902-6_2

135. Pereira, J. *et al.* Crude Oil Desalting Process. *Adv. Petrochemicals* (2015). doi:10.5772/61274
136. Patel, V. Advances in Petrochemicals. *Adv. Petrochemicals* (2015). doi:10.5772/59296
137. Feng, J. *et al.* Nanoemulsions obtained via bubble-bursting at a compound interface. *Nat. Phys. 2014 108* **10**, 606–612 (2014).
138. Post, E., Kwon, G. & Tuteja, A. Oil–Water Separation with Selective Wettability Membranes. *RSC Soft Matter* **2017-Janua**, 347–367 (2016).
139. Kang, W., Jing, G., Zhang, H., Li, M. & Wu, Z. Influence of demulsifier on interfacial film between oil and water. *Colloids Surfaces A Physicochem. Eng. Asp.* **272**, 27–31 (2006).
140. Sams, G. W. & Zaouk, M. Emulsion Resolution in Electrostatic Processes. *Energy and Fuels* **14**, 31–37 (1999).
141. Lai, A., Bremond, N. & Stone, H. A. Separation-driven coalescence of droplets: an analytical criterion for the approach to contact. *J. Fluid Mech.* **632**, 97–107 (2009).
142. Ristenpart, W. D., Bird, J. C., Belmonte, A., Dollar, F. & Stone, H. A. Non-coalescence of oppositely charged drops. *Nat. 2009 4617262* **461**, 377–380 (2009).
143. Chun, C.-L., Park, J.-W. & Member, A. Oil Spill Remediation Using Magnetic Separation. *J. Environ. Eng.* **127**, 443–449 (2001).
144. Leary, T., Yeganeh, M. & Maldarelli, C. Microfluidic Study of the Electrocoalescence of Aqueous Droplets in Crude Oil. *ACS Omega* **5**, 7348–7360 (2020).
145. Liu, Z., Chan, S. T., Faizi, H. A., Roberts, R. C. & Shum, H. C. From chip-in-a-lab to lab-on-a-chip: towards a single handheld electronic system for multiple application-specific lab-on-a-chip (ASLOC). **15**, (2014).
146. Luo, S., Schiffbauer, J. & Luo, T. Effect of electric field non-uniformity on droplets coalescence. *Phys. Chem. Chem. Phys.* **18**, 29786–29796 (2016).
147. Prieve, D. C., Yezer, B. A., Khair, A. S., Sides, P. J. & Schneider, J. W. Formation of Charge Carriers in Liquids. *Adv. Colloid Interface Sci.* **244**, 21–35 (2017).
148. Smith, G. N. & Eastoe, J. Controlling colloid charge in nonpolar liquids with surfactants. *Physical Chemistry Chemical Physics* **15**, 424–439 (2013).

149. Mengotti Charin, R. *et al.* Crude Oil Electrical Conductivity Measurements at High Temperatures: Introduction of Apparatus and Methodology. (2017). doi:10.1021/acs.energyfuels.6b03237
150. J. Patrick BerryStewart J. MulveyAdrian G. BaileyMartin T. ThewTrevor J. WilliamsNicholas J. WaythOlav Urdahl. Compact electrostatic coalescer. (1998).
151. Reza Mahmoudi, Seyed; Varanasi, K. K. Systems and methods for unipolar separation of emulsions and other mixtures. (2016).
152. Shahbaznezhad, M., Dehghanghadikolaei, A. & Sojoudi, H. Contactless Method for Electrocoalescence of Water in Oil. *ACS Omega* **6**, 14298–14308 (2021).
153. R., K. P. Applied Electrostatic Precipitation. *Appl. Electrost. Precip.* (1996). doi:10.1007/978-94-009-1553-4
154. Less, S. & Vilagines, R. The electrocoalescers' technology: Advances, strengths and limitations for crude oil separation. *J. Pet. Sci. Eng.* **81**, 57–63 (2012).
155. Warner, E. H. *Corona Discharge (Classic Reprint)*. (Fb&c Limited, 2016, 2016).
156. Dukhin, A. S. & Goetz, P. J. How non-ionic 'electrically neutral' surfactants enhance electrical conductivity and ion stability in non-polar liquids. *J. Electroanal. Chem.* **588**, 44–50 (2006).
157. Park, J. K., Ryu, J. C., Kim, W. K. & Kang, K. H. Effect of Electric Field on Electrical Conductivity of Dielectric Liquids Mixed with Polar Additives: DC Conductivity. doi:10.1021/jp9015189
158. Bombard, A. J. F. & Dukhin, A. Ionization of a nonpolar liquid with an alcohol. *Langmuir* **30**, 4517–4521 (2014).
159. Higuera, F. J. Electrohydrodynamic flow of a dielectric liquid around a blade electrode. *Phys. Fluids* **12**, 2732–2742 (2000).
160. Higuera, F. J. Electrohydrodynamic flow of a dielectric liquid due to autonomous injection of charge by a needle electrode. *Phys. Fluids* **14**, 423–426 (2002).
161. Ryu, J. C., Park, H. J., Park, J. K. & Kang, K. H. New Electrohydrodynamic Flow Caused by the Onsager Effect. (2009). doi:10.1103/PhysRevLett.104.104502
162. Liu, Z., Chan, S. T., Faizi, H. A., Roberts, R. C. & Shum, H. C. Droplet-based electro-coalescence for probing threshold disjoining pressure. *Lab Chip* **15**, 2018–2024 (2015).

163. Mohammadi, M. and F. M. Parametric study on electrical conductivity of crude oils; basis experimental data. *Petroleum and Coal* (2016). Available at: https://www.researchgate.net/publication/311494030_Parametric_study_on_electrical_conductivity_of_crude_oils_basis_experimental_data. (Accessed: 3rd February 2022)
164. Dukhin, A. & Parlia, S. Ions, ion pairs and inverse micelles in non-polar media. *Current Opinion in Colloid and Interface Science* **18**, 93–115 (2013).
165. Post-Combustion CO2 Capture | netl.doe.gov. Available at: https://netl.doe.gov/coal/carbon-capture/post-combustion. (Accessed: 13th October 2021)
166. Samanta, A., Zhao, A., Shimizu, G. K. H., Sarkar, P. & Gupta, R. Post-Combustion CO2 Capture Using Solid Sorbents: A Review. *Ind. Eng. Chem. Res.* **51**, 1438–1463 (2011).
167. Wang, M., Lawal, A., Stephenson, P., Sidders, J. & Ramshaw, C. Post-combustion CO2 capture with chemical absorption: A state-of-the-art review. *Chem. Eng. Res. Des.* **89**, 1609–1624 (2011).
168. Luis, P. & Bruggen, B. Van der. The role of membranes in post-combustion CO2 capture. *Greenh. Gases Sci. Technol.* **3**, 318–337 (2013).
169. Zhao, S. *et al.* Status and progress of membrane contactors in post-combustion carbon capture: A state-of-the-art review of new developments. *J. Memb. Sci.* **511**, 180–206 (2016).
170. Mattisson, T., Lyngfelt, A. & Cho, P. The use of iron oxide as an oxygen carrier in chemical-looping combustion of methane with inherent separation of CO2. *Fuel* **80**, 1953–1962 (2001).
171. Ben-Mansour, R. *et al.* Carbon capture by physical adsorption: Materials, experimental investigations and numerical modeling and simulations – A review. *Appl. Energy* **161**, 225–255 (2016).
172. Song, C., Liu, Q., Deng, S., Li, H. & Kitamura, Y. Cryogenic-based CO2 capture technologies: State-of-the-art developments and current challenges. *Renew. Sustain. Energy Rev.* **101**, 265–278 (2019).
173. Giordano, L., Roizard, D. & Favre, E. Life cycle assessment of post-combustion CO2 capture: A comparison between membrane separation and chemical absorption processes. *Int. J. Greenh. Gas Control* **68**, 146–163 (2018).
174. Savile, C. K. & Lalonde, J. J. Biotechnology for the acceleration of carbon dioxide capture

and sequestration. *Curr. Opin. Biotechnol.* **22**, 818–823 (2011).

175. Ho, S. H., Chen, C. Y., Lee, D. J. & Chang, J. S. Perspectives on microalgal CO2-emission mitigation systems — A review. *Biotechnol. Adv.* **29**, 189–198 (2011).
176. Global Status Report - Global CCS Institute. Available at: https://www.globalccsinstitute.com/resources/global-status-report/. (Accessed: 23rd August 2021)
177. Cho, M., Lee, S., Choi, M. & Lee, J. W. Novel Spray Tower for CO2 Capture Using Uniform Spray of Monosized Absorbent Droplets. *Ind. Eng. Chem. Res.* **57**, 3065–3075 (2018).
178. and, J. K. & Aroonwilas*, A. Performance of Spray Column for CO2 Capture Application. *Ind. Eng. Chem. Res.* **47**, 145–153 (2007).
179. Xu, Y. *et al.* Numerical simulation of aqueous ammonia-based CO2 absorption in a sprayer tower: An integrated model combining gas-liquid hydrodynamics and chemistry. *Appl. Energy* **211**, 318–333 (2018).
180. Stolaroff, J. K., Keith, D. W. & Lowry, G. V. Carbon dioxide capture from atmospheric air using sodium hydroxide spray. *Environ. Sci. Technol.* **42**, 2728–2735 (2008).
181. Wan, Z. & Li, Y. Numerical study of the falling film wettability and heat transfer on the inclined plates with different corrugated structures. *Asia-Pacific J. Chem. Eng.* **16**, e2664 (2021).
182. Khakharia, P., Kvamsdal, H. M., Da Silva, E. F., Vlugt, T. J. H. & Goetheer, E. Field study of a Brownian Demister Unit to reduce aerosol based emission from a Post Combustion CO2 Capture plant. *Int. J. Greenh. Gas Control* **28**, 57–64 (2014).
183. Rahimi, R. & Abbaspour, D. Determination of pressure drop in wire mesh mist eliminator by CFD. *Chem. Eng. Process. Process Intensif.* **47**, 1504–1508 (2008).
184. Parker, K. R. Applied electrostatic precipitation. 521 (1997).
185. Damak, M. & Varanasi, K. K. Electrostatically driven fog collection using space charge injection. *Sci. Adv.* **4**, (2018).
186. Choi, M., Cho, M. & Lee, J. W. Empirical formula for the mass flux in chemical absorption of CO2 with ammonia droplets. *Appl. Energy* **164**, 1–9 (2016).
187. Epa. Wet Electrostatic Precipitator (ESP) - Wire Pipe Type.

188. Reynolds, J. P., Theodore, L. & Marino, J. Calculating Collection Efficiencies for Electrostatic Precipitators. *J. Air Pollut. Control Assoc.* **25**, 610–616 (1975).
189. Turner, J. H. *et al.* Electrostatic Precipitators. (1999).
190. IECM Technical Documentation: Amine-based Post-Combustion CO 2 Capture.
191. Keith, D. W., Holmes, G., St. Angelo, D. & Heidel, K. A Process for Capturing CO2 from the Atmosphere. *Joule* **2**, 1573–1594 (2018).
192. Analysis, Synthesis and Design of Chemical Processes - Richard Turton, Richard C. Bailie, Wallace B. Whiting, Joseph A. Shaeiwitz - Google Books. Available at: https://books.google.com/books?hl=en&lr=&id=kWXyhVXztZ8C&oi=fnd&pg=PT3&dq=%5B1%5D+Turton,+R.+et+al.+Analysis,+Synthesis,+and+Design+of+Chemical+Processes.+Prentice+Hall,+2009.&ots=p_lVsHvQvG&sig=ExBigZieQSrpwzJE26pzjO8KtaQ#v=onepage&q&f=false. (Accessed: 15th October 2021)
193. Woodard, M. K. Stationary Source Control Techniques Document for Fine Particulate Matter. (1998).